

Department of Mechanical and
Industrial Engineering
University of Illinois at
Urbana-Champaign
Urbana, IL 61801



UILU ENG-88-4001

4

AD-A190 772

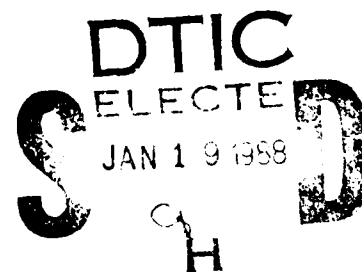
NUMERICAL AND EXPERIMENTAL INVESTIGATION OF MULTIPLE SHOCK WAVE/TURBULENT BOUNDARY LAYER INTERACTIONS IN A RECTANGULAR DUCT

J. C. Dutton and B. F. Carroll

Final Technical Report submitted to
Office of Naval Research
Mechanics Division
Arlington, VA 22217-5000

Contract No. N00014-85-K-0665
Work Unit No. 432e-009

January 1988



REPORT DOCUMENTATION PAGE

1a REPORT SECURITY CLASSIFICATION Unclassified			1b. RESTRICTIVE MARKINGS None		
2a SECURITY CLASSIFICATION AUTHORITY			3. DISTRIBUTION/AVAILABILITY OF REPORT Approved for Public Release; Distribution Unlimited		
2b DECLASSIFICATION/DOWNGRADING SCHEDULE					
4. PERFORMING ORGANIZATION REPORT NUMBER(S) UILU-ENG-88-4001			5. MONITORING ORGANIZATION REPORT NUMBER(S)		
6a NAME OF PERFORMING ORGANIZATION University of Illinois at Urbana-Champaign		6b. OFFICE SYMBOL (If applicable) UIUC	7a. NAME OF MONITORING ORGANIZATION Office of Naval Research		
6c. ADDRESS (City, State, and ZIP Code) Dept. of Mechanical & Industrial Engineering 1206 West Green Street Urbana, Illinois 61801			7b. ADDRESS (City, State, and ZIP Code) ATTN: Dr. S. G. Lekoudis, Code 432F 800 North Quincy Street Arlington, Virginia 22217-5000		
8a. NAME OF FUNDING/SPONSORING ORGANIZATION Office of Naval Research		8b. OFFICE SYMBOL (If applicable) ONR	9. PROCUREMENT INSTRUMENT IDENTIFICATION NUMBER Contract No. N00014-85-K-0665		
8c. ADDRESS (City, State, and ZIP Code) Attn: Dr. S. G. Lekoudis, Code 432F 800 North Quincy Street Arlington, Virginia 22217-5000			10. SOURCE OF FUNDING NUMBERS		
			PROGRAM ELEMENT NO.	PROJECT NO.	TASK NO.
			WORK UNIT ACCESSION NO 432e-009		
11. TITLE (Include Security Classification) Numerical and Experimental Investigation of Multiple Shock Wave/Turbulent Boundary Layer Interactions in a Rectangular Duct					
12. PERSONAL AUTHOR(S) J. C. Dutton and B. F. Carroll					
13a. TYPE OF REPORT Final Technical		13b. TIME COVERED FROM 1 Jul 85 TO 31 Dec 87		14. DATE OF REPORT (Year, Month, Day) 1988 January 6	
				15. PAGE COUNT 107	
16. SUPPLEMENTARY NOTATION					
17. COSATI CODES			18. SUBJECT TERMS (Continue on reverse if necessary and identify by block number)		
FIELD	GROUP	SUB-GROUP			
			Shock wave; Turbulent boundary layer; Flow separation; Laser Doppler velocimetry; Navier-Stokes computations		
19. ABSTRACT (Continue on reverse if necessary and identify by block number)					
<p>Multiple shock wave/turbulent boundary layer interactions in constant or nearly constant area supersonic duct flows occur in a variety of devices including scramjet inlets, gas ejectors, and supersonic wind tunnels. For sufficiently high duct exit pressures, a multiple shock wave/turbulent boundary layer interaction or shock train may form in the duct and cause a highly nonuniform, and possibly unsteady, flow at the duct exit.</p> <p>In this report, the mean flow characteristics of two shock train interactions, one with an initial Mach number of 2.5 the other at Mach 1.6, are investigated using spark Schlieren photography, surface oil flow visualization, and mean wall pressure measurements. An LDV investigation of the Mach 1.6 interaction is currently underway. The experiments were performed in 3 inch wide rectangular ducts with nominal heights of 1.5 and 1.4 inches for the Mach 2.5 and 1.6 interactions, respectively. The Mach 2.5 interaction was oblique and asymmetric in nature. A large separation occurs after the first oblique shock. The top and bottom wall boundary layer</p>					
20. DISTRIBUTION/AVAILABILITY OF ABSTRACT <input checked="" type="checkbox"/> UNCLASSIFIED/UNLIMITED <input checked="" type="checkbox"/> SAME AS RPT <input type="checkbox"/> DTIC USERS			21. ABSTRACT SECURITY CLASSIFICATION Unclassified		
22a. NAME OF RESPONSIBLE INDIVIDUAL Dr. Spiro G. Lekoudis			22b. TELEPHONE (Include Area Code) (202) 696-4306		22c. OFFICE SYMBOL ONR

separation has been investigated, revealing that the shape of the reattachment lines and surface flow patterns for the two separation regions are quite different. This oblique shock flow pattern occurs in a neutrally stable fashion with each type of opposing separation region alternately existing on either the top or bottom wall during the course of a run. A small scale unsteadiness in the shock train location, with movement on the order of a boundary layer thickness, is also observed. In contrast, the Mach 1.6 interaction consists of repeated, symmetric normal shocks. The initial, bifurcated normal shock has a small separation region at its foot while the following weaker shocks do not separate the boundary layer. The number of shocks in the shock train and the overall length of the interaction increase as the boundary layer thickens in the duct. Only very slight unsteadiness in the shock train location is observed at this lower Mach number. A comparison of the Mach 2.5 and 1.6 shock train interactions is made and features of these types of interactions are discussed. In conjunction with a review of the existing literature, these results help establish the type of shock system to be expected under various operating conditions and the amount of flow nonuniformity and unsteadiness which can be caused.

The experimental investigation has been coordinated with a numerical study of the shock train phenomenon. The computations use the explicit, time-dependent, second-order accurate MacCormack scheme to solve the mass averaged Navier-Stokes equations. Turbulence is modeled via the Baldwin-Lomax algebraic model and the Wilcox-Rubesin two-equation model. Test calculations have been performed for two flat plate equilibrium turbulent boundary layer flows and one separated oblique shock/turbulent boundary layer interaction. A numerical simulation of the Mach 1.6 multiple normal shock/turbulent boundary layer interaction is currently being performed.

FINAL TECHNICAL REPORT

NUMERICAL AND EXPERIMENTAL INVESTIGATION OF MULTIPLE SHOCK WAVE/TURBULENT BOUNDARY LAYER INTERACTIONS IN A RECTANGULAR DUCT

by

J. C. Dutton, Associate Professor
B. F. Carroll, ONR Graduate Fellow

Department of Mechanical and Industrial Engineering
University of Illinois at Urbana-Champaign
Urbana, Illinois 61801

Supported by

Office of Naval Research
Contract Number N00014-85-K-0665
Work Unit Number 432e-009
Technical Monitor, Dr. S. G. Lekoudis

Report Number UILU-ENG-88-4001
January 1988

Approved for Public Release; Distribution Unlimited



Accession For	
NTIS SERIAL	<input checked="checked" type="checkbox"/>
DTIC TAB	<input type="checkbox"/>
Unannounced	<input type="checkbox"/>
Justification	
By	
Distribution	
Availability	
Notes	
A-1	

ABSTRACT

Multiple shock wave/turbulent boundary layer interactions in constant or nearly constant area supersonic duct flows occur in a variety of devices including scramjet inlets, gas ejectors, and supersonic wind tunnels. For sufficiently high duct exit pressures, a multiple shock wave/turbulent boundary layer interaction or shock train may form in the duct and cause a highly nonuniform, and possibly unsteady, flow at the duct exit.

In this report, the mean flow characteristics of two shock train interactions, one with an initial Mach number of 2.5 the other at Mach 1.6, are investigated using spark Schlieren photography, surface oil flow visualization, and mean wall pressure measurements. An LDV investigation of the Mach 1.6 interaction is currently underway. The experiments were performed in 3 inch wide rectangular ducts with nominal heights of 1.5 and 1.4 inches for the Mach 2.5 and 1.6 interactions, respectively. The Mach 2.5 interaction was oblique and asymmetric in nature. A large separation occurs after the first oblique shock. The top and bottom wall boundary layer separation has been investigated, revealing that the shape of the reattachment lines and surface flow patterns for the two separation regions are quite different. This oblique shock flow pattern occurs in a neutrally stable fashion with each type of opposing separation region alternately existing on either the top or bottom wall during the course of a run. A small scale unsteadiness in the shock train location, with movement on the order of a boundary layer thickness, is also observed. In contrast, the Mach 1.6 interaction consists of repeated, symmetric normal shocks. The initial, bifurcated normal shock has a small separation region at its foot while the following weaker shocks do not separate the boundary layer. The number of shocks in the shock train and the overall length of the interaction increase as the boundary layer thickens in the duct. Only very slight unsteadiness in the shock train location is observed at this lower Mach number. A comparison of the Mach 2.5 and 1.6 shock train interactions is made and features of these types of interactions are discussed. In conjunction with a review of the

existing literature, these results help establish the type of shock system to be expected under various operating conditions and the amount of flow nonuniformity and unsteadiness which can be caused.

The experimental investigation has been coordinated with a numerical study of the shock train phenomenon. The computations use the explicit, time-dependent, second-order accurate MacCormack scheme to solve the mass averaged Navier-Stokes equations. Turbulence is modelled via the Baldwin-Lomax algebraic model and the Wilcox-Rubesin two-equation model. Test calculations have been performed for two flat plate equilibrium turbulent boundary layer flows and one separated oblique shock/turbulent boundary layer interaction. A numerical simulation of the Mach 1.6 multiple normal shock/turbulent boundary layer interaction is currently being performed.

TABLE OF CONTENTS

	Page
ABSTRACT	ii
I. INTRODUCTION	1
II. LITERATURE REVIEW	6
A. EXPERIMENTAL WORK, UNCONFINED INTERACTION	6
B. EXPERIMENTAL WORK, CONFINED INTERACTION	9
C. NUMERICAL WORK	16
III. NUMERICAL TECHNIQUES	18
A. GOVERNING EQUATIONS	18
1. BALDWIN-LOMAX TURBULENCE MODEL	22
2. WILCOX-RUBESIN TURBULENCE MODEL	24
B. NUMERICAL TECHNIQUES	18
C. BOUNDARY AND INITIAL CONDITIONS	28
1. INFLOW AND SYMMETRY BOUNDARY CONDITIONS	29
2. OUTFLOW BOUNDARY CONDITIONS	29
3. SOLID WALL BOUNDARY CONDITIONS	31
D. TEST CALCULATIONS	36
1. TEST CASE 1	36
2. TEST CASE 2	38
3. TEST CASE 3	41
IV. EXPERIMENTAL SETUP	43
A. EXPERIMENTAL AIR FLOW FACILITY AND TEST SECTION..	43
B. SCHLIEREN, SURFACE FLOW, AND PRESSURE	
MEASURING PROCEDURES	48
C. LDV PROCEDURES	49

V. EXPERIMENTAL RESULTS	52
A. MACH 2.45 RESULTS	52
1. MACH 2.45 FLOW VISUALIZATIONS	53
2. MACH 2.45 PRESSURE MEASUREMENTS	56
B. MACH 1.6 RESULTS	58
1. MACH 1.6 FLOW VISUALIZATIONS	58
2. MACH 1.6 PRESSURE MEASUREMENTS	61
VI. CONCLUSIONS AND RECOMMENDATIONS	63
VIII. REFERENCES	65
APPENDIX A.	103
APPENDIX B. RESEARCH CONTRACT-RELATED PUBLICATIONS ..	106
APPENDIX C. PARTICIPATING PERSONNEL	107

I. INTRODUCTION

This report describes the results of an integrated numerical and experimental investigation of multiple shock wave/turbulent boundary layer interactions in confined rectangular ducts. Multiple shock wave/turbulent boundary layer interactions, also called pseudo-shock or shock train interactions, are typically found in confined, internal, supersonic flows experiencing large adverse pressure gradients. Rather than recompressing through a single shock, as would be expected in an inviscid flow, the flow recompresses through an extended shock system consisting of a series of repeated normal or oblique shocks. Reacceleration of the flow following each shock is caused by adjustments in the wall boundary layers. The objective of this study is to investigate the shock train phenomenon, both experimentally and numerically, with the goal of understanding the detailed turbulent and mean flow mechanisms occurring in the shock train. Additionally, the ability of existing numerical techniques to compute such flows is evaluated.

Multiple shock wave/turbulent boundary layer interactions occur in a variety of devices of technological importance. Examples include supersonic gas ejectors, supersonic wind tunnel diffusers, and scramjet (supersonic combustion ramjet) inlets. Ejectors are used to both pump and mix fluids and are especially suited to applications requiring low maintenance or involving corrosive fluids. A supersonic ejector uses a high stagnation pressure supersonic stream to entrain a lower stagnation pressure secondary stream. The two streams mix and recompress in a mixing duct. Under proper conditions, both streams attain supersonic velocities in the duct, then decelerate through a shock train system to subsonic exit velocities. Both the mixing effect of the shock train as well as its pressure recovery are important in this application. In supersonic wind tunnel diffusers, shock train systems are often found and are usually the dominant source of losses in the diffuser. Consequently, the power required to operate the wind tunnel is directly related to the losses occurring in the shock train.

The main impetus for the current research is the development of scramjet propulsion systems. Recently, a heightened interest in scramjet propulsion has been shown. The U.S. Navy is developing defensive missiles capable of maintaining high supersonic speeds for ranges exceeding several hundred miles. Ramjet or scramjet air-breathing propulsion systems will probably be required to achieve the necessary range under the size and weight constraints imposed by current launch platforms and launchers. Much attention has also been focused on the development of a new hypersonic aircraft, called the National Aero-Space Plane or X-30, which will employ scramjet propulsion¹. The development of such an aircraft is expected to depend heavily on computational fluid dynamic (CFD) methods to supplement conventional wind tunnel testing, assuming the reliability of the computational approach can be demonstrated². This increased dependence on numerical predictions is due to the scarcity of hypersonic test facilities, difficulties in performing hypersonic measurements, and the lower relative cost of numerical predictions. The research reported herein will help develop a better understanding of the inlet flow, including the detailed turbulent transport and flow reacceleration phenomena which can occur and will help qualify computational techniques for predicting such flows.

Traditionally, less than optimal scramjet and ramjet inlet designs have been used due to the limited knowledge of the inlet flowfield. Ramjet inlet flowfields are characterized by complicated shock structures, rapidly growing boundary layers, large separated regions, and undesirable, self-excited, low frequency oscillations. Ramjet inlet flows have also shown strong coupling with unsteady combustor pressures resulting in large amplitude oscillations. These problems have led to a series of investigations, both numerical and experimental, into the behavior of ramjet flowfields. Some of the more recent results are those of Hsieh, et al.³, Hsieh, et al.⁴, Bogar⁵, Bogar, et al.⁶, Sajben, et al.⁷, and Talcott and Kumar⁸. Scramjet inlet flows have received considerably less attention relative to those of ramjet inlets. While the two types of inlets perform similar functions, the ramjet inlet's geometry and internal flow are significantly different than the scramjet's. Scramjet inlet flowfields are also characterized by

complicated shock patterns, large separation regions, and thick boundary layers compared to the duct dimensions. For sufficiently high combustor pressures, a shock train may form in the diffuser portion of the inlet, thereby adversely affecting the pressure recovery and causing a highly nonuniform flow at the diffuser exit. The unsteady nature of the scramjet inlet flow, the inlet normal and oblique shock train phenomena, the susceptibility of the scramjet inlet to self-excited and combustor-induced oscillations, and the unsteady inlet buzz phenomenon are aspects of the scramjet inlet flow which require further study. In particular, Waltrup⁹ identified the shock wave/boundary layer interactions occurring in scramjet inlets as an area requiring further research. He states that detailed measurements of the turbulent transport and dissipation mechanisms in the near wall region for a variety of initial conditions are needed. According to Waltrup, "it is these that are of interest in hypersonic inlets, especially in internally ducted supersonic flows with compression and expansion waves so that the viscous total pressure losses as well as regions of separation can be modeled and predicted with confidence."

As stated above, the objective of this research is to contribute to a better understanding of the complicated flow mechanisms involved in the shock train phenomenon and to evaluate numerical predictive techniques for such flows. A combined numerical and experimental investigation has been performed. The numerical portion of the work was undertaken both to evaluate the ability of existing numerical techniques for calculating such flows and to assist in the planning, execution, and evaluation of the experimental work. These calculations employ the widely used explicit MacCormack scheme to integrate the time-dependent, mass-averaged Navier-Stokes equations along with a two-equation model of turbulence and an algebraic turbulence model. This approach is typical of those currently being used for scramjet engine analysis as discussed by White, et al.¹⁰, although most previous work has used only the simpler algebraic turbulence models and has focused on the gross flowfield characteristics. The current experimental investigation has been performed to improve the understanding of the flow mechanisms occurring in the shock train interaction and to add to the relatively sparse data base on such interactions. Such a data base is needed both to assist in the understanding and

analysis of shock train interactions and to evaluate and improve numerical techniques for calculating such flows. The experimental measurements were taken in a small scale planar two-dimensional wind tunnel with incoming Mach numbers of 2.45 and 1.6. Experimental measurement techniques included spark Schlieren photography, oil streak surface flow visualization, mean wall static pressure measurements, and two-component, coincident laser Doppler velocimeter (LDV) measurements of the mean and turbulent velocity fields. The experimental techniques employed are similar to those being used by Yanta¹¹ to investigate a planar two-dimensional scramjet inlet flow. This inlet consists of a 10 degree precompression ramp, followed by an inward turning scoop feeding a nearly constant area supersonic diffuser of rectangular cross section. Waltrup⁹ listed Yanta's work as the only other relevant investigation of a diffuser flow of this type in which experimental measurements, of sufficient detail to study the turbulent transport as well as mean flow phenomena occurring, are being taken. In the current work, the flow non-uniformities caused by the inward turning scoop portion of a scramjet type inlet have been avoided and the flow mechanisms in the shock train system are investigated for a uniform incoming supersonic ducted flow, with an equilibrium turbulent boundary layer.

Several studies^{12,13,14} have shown that three-dimensional effects are present in nominally two-dimensional planar oblique shock/boundary layer interactions due to the interaction of the oblique shock with the side wall boundary layers. Chriss, et al.¹⁵ have also shown that some three-dimensionality is present in a multiple normal shock interaction in a square duct. While axisymmetric geometries provide a more nearly two-dimensional flow, measurements in these geometries are difficult. Optical techniques such as Schlieren or LDV are complicated by the curvature of the duct walls. Physical probes, such as pressure or hot wire probes, can be used, but their presence causes undesirable flow disturbances. In this study, a planar two-dimensional geometry was selected to facilitate LDV and Schlieren studies of the interaction. Furthermore, applications such as the National Aerospace Plane will involve planar geometries.

In the remainder of this report, the shock train phenomenon will be described in more detail. The literature review describes both confined and unconfined shock wave/boundary layer interactions illustrating the major differences between these two types of flows. The major features of the confined, shock train interaction are introduced and previous experimental and numerical investigations of this phenomenon are discussed. Details of the experimental and numerical approaches are then given. Finally, a discussion of the experimental and numerical results is presented and some concluding remarks and recommendations are made.

II. LITERATURE REVIEW

In this section the relevant literature pertaining to multiple shock wave/turbulent boundary layer or shock train interactions in constant area or nearly constant area rectangular ducts is reviewed. An introduction to the nomenclature and basic physical concepts relating to this type of interaction is incorporated into the literature review. Before proceeding further, a distinction between confined and unconfined shock wave/turbulent boundary layer interactions is made. The confined nature of an internal ducted supersonic flow is necessary for the shock train phenomenon to occur. With external shock wave/boundary layer interactions, the flow downstream of the interaction is unconfined, and the multiple shock phenomenon, characterized by flow reacceleration following each shock, is not normally observed. Thus, the shock wave/boundary layer interaction for confined flows is fundamentally different than for external, unconfined flows. In this work a confined interaction is defined as an internal interaction in which the confinement effect of the duct walls noticeably affects the interaction. Unconfined interactions are defined as any interaction, external or internal, in which confinement effects are negligible.

A large number of previous studies have focused on the shock wave/turbulent boundary layer interaction. Fortunately, several review articles are available which have summarized the results of these papers. Two review articles are of particular interest: Green¹⁶ and Adamson and Messiter¹⁷. While no effort will be made to duplicate the contents of these two reviews, several papers deserve individual discussion due to their relevance to the work reported herein. Additionally, important contributions to this area of research have been made since Adamson and Messiter's¹⁷ article.

A. EXPERIMENTAL WORK, UNCONFINED INTERACTION

In this section, only papers treating the unconfined, nominally steady, normal shock/turbulent boundary layer interaction will be reviewed, as this unconfined interaction

bears some resemblance to the confined shock train interaction under consideration. A summary of the relevant unconfined studies is given in Table 1. Several researchers have considered this problem including Seddon¹⁸, Vidal, et al.¹⁹, Kooi²⁰, East²¹, and Delery²² with both East and Delery making laser Doppler velocimeter (LDV) measurements of the flow. These studies were all performed in wind tunnels for which confinement effects were small. The flows studied by East and Delery exhibited small flow confinement effects and one of Seddon's configurations also showed similar effects. However, these three studies^{18,21,22} appear to be best described as unconfined interaction studies.

East²¹ and Delery²² both observed unseparated normal shock/turbulent boundary layer interactions with a Mach number at the start of the interaction, M_u , of 1.3. At this low Mach number, the pressure rise across the shock is too small to cause the boundary layer to separate. As shown in Figure 1, the subsonic portion of the unseparated boundary layer thickens upstream of the shock causing compression waves to emanate from the sonic line which eventually coalesce forming a foot for the outer shock. The outer shock is slightly curved, being a strong oblique shock (not strictly normal) with the flow following the interaction being totally subsonic. The wall static pressure increases in a continuous fashion, while the static pressure in the core flow increases discontinuously, reflecting the mixed subsonic/supersonic nature of the interaction.

At higher Mach numbers, the inertial forces in the subsonic layer near the wall are not strong enough to negotiate the increased pressure rise and the boundary layer will separate at the foot of the shock, thereby increasing the streamwise extent of the pressure rise. Seddon¹⁸, Vidal et al.¹⁹, Kooi²⁰, East²¹, and Delery²² all found separated normal shock/turbulent boundary layer interactions at Mach numbers greater than $M_u = 1.4$ and various Reynolds numbers. The presence of a free interaction at the separation point has been observed experimentally, i.e. the flow upstream of and slightly downstream of the separation does not depend on the details of the downstream pressure rise.

A schematic of the separated, unconstrained interaction is shown in Figure 2. The increasing thickness of the subsonic layer in the region near the separation point causes weak oblique compression waves to propagate into the outer flow. These waves coalesce to form a weak oblique shock (leading shock) which eventually intersects the strong, nearly normal shock in the outer supersonic flow. At this intersection, termed the bifurcation point, a second weak oblique shock (trailing shock) is generated which propagates back toward the wall. A slip line is also generated at the bifurcation point and extends downstream, static pressure and flow direction being matched across the slip line. The second oblique shock is required to satisfy compatibility of flow direction, while the slip line is indicative of a mismatch in velocity magnitude caused by the differing losses through the outer and inner shocks. A region of supersonic flow which isentropically decelerates to subsonic speed may exist in the otherwise subsonic flow below the slip line. In experiments involving a Mach 1.47 separated normal shock interaction, Seddon¹⁸ observed such a region, which he called a "supersonic tongue." However, in a similar separated normal shock interaction at Mach 1.4, Kooi²⁰ did not observe this phenomenon, indicating a Mach number dependence. This dependence was confirmed in a series of three normal shock/boundary layer interaction experiments where East²¹ found all subsonic flow behind a Mach 1.3 interaction, a region of sonic flow behind a Mach 1.4 interaction, and a supersonic tongue at the boundary layer edge behind a Mach 1.54 interaction. A second Mach number dependence is related to the strength of the nearly normal shock. As the Mach number increases, the pressure rise increases, causing the separation region to grow in size, effectively pushing the bifurcation point further from the wall. The freestream Reynolds number also has an effect on the interaction as shown, for example, by Vidal, et al.¹⁹. For a fixed pressure rise, the length of the separation region and height of the bifurcation point above the wall increases as Reynolds number based on undisturbed boundary layer thickness, Re_{δ_u} , decreases.

Some general observations about these unconfined, normal shock wave/turbulent boundary layer studies follow. Throughout the interaction region, large variations in the static

and stagnation pressure are observed across the boundary layer, normal to the wall, and following the interaction the boundary layer takes an appreciable distance to fully recover to equilibrium conditions. For example, Seddon¹⁸ found the boundary layer following a separated normal shock interaction to be still recovering after up to 50 undisturbed boundary layer thicknesses downstream of the start of the interaction. Vidal, et al.¹⁹, using high speed Schlieren movies, detected an unsteady shock structure at the bifurcation point. Unsteady shock structures were also observed by East²¹ and by Delery²². Both investigators found that the use of an adjustable second throat to choke the subsonic flow following the interaction substantially improved the steadiness of the shock, presumably because such a device isolates the interaction from downstream pressure fluctuations. East²¹ also used conditional sampling in his LDV measurements to avoid measuring "false turbulence" caused by shock motion.

B. EXPERIMENTAL WORK, CONFINED INTERACTION

Despite many similarities, major differences exist between unconfined and confined shock wave/boundary layer interactions. Flow confinement, as characterized by the ratio of the undisturbed boundary layer thickness to the radius of the duct (for axisymmetric geometries), δ_u/r , can have significant effects on the interaction, leading to three types of shock systems²³: a single normal shock for small δ_u/r , a series of nearly normal shocks for moderate δ_u/r , and a series of strong oblique shocks for large δ_u/r . In a planar geometry, the confinement parameter is defined as δ_u/h , where h is the duct half height in the direction perpendicular to the surface at which the interaction of interest occurs (normally taken as the shorter dimension in a rectangular duct). The Mach number in the core flow at the start of the interaction, M_u , and the confinement parameter are the primary parameters affecting the confined interaction as shown by Merkli²⁴ and Mateer and Viegas²⁵. Reynolds number was shown to have a less pronounced influence on the confined interaction as compared to the unconfined interaction. Experimental studies of the confined shock wave/boundary layer interaction have been performed in both planar two-dimensional and axisymmetric geometries, with varying degrees

of detail. In reviewing the experimental work, the various types of measurements will be discussed separately, beginning with the Schlieren flow visualization, overall pressure recovery, and surface pressure rise studies, and followed by the mean flow and turbulence studies. A summary of the confined experimental studies is given in Table 2.

Lustwerk²³, McLafferty, et al.²⁶, and Fejer, et al.²⁷ have all shown still Schlieren photographs of the various shock structures. While these photographs clearly show the instantaneous structure of the three types of shock systems (single normal shock, multiple normal shocks, or multiple oblique shocks), high speed Schlieren movies of the interactions were not used to investigate the steadiness of the interaction. McLafferty, et al.²⁶ also presented high speed measurements of fluctuating wall pressures in a constant area axisymmetric duct. Pressure fluctuations with frequencies of 240 to 300 Hz were found in the neighborhood of the shock interaction. These fluctuations were present at Mach numbers of 2.51 and 2.20, indicating the presence of some shock unsteadiness in constant area, circular ducts. Resonance frequencies of about 300 Hz were also calculated for the subsonic duct flow following the shock. Lustwerk²³ noted that diverging the duct by 50 minutes (full angle) helped to stabilize the shock system in a rectangular duct.

A series of papers from by Ikui, et al.^{28,29,30} gives an enlightening overview of the shock train phenomenon. Schlieren photographs along with wall pressure measurements were used to investigate the shock train for Mach numbers ranging from 1.33 to 2.79.²⁸ At $M_u = 1.33$ a single normal shock was observed. Mach numbers from 1.37 to 1.60 yielded multiple normal shocks, while Mach numbers from 1.86 to 2.79 caused multiple oblique shocks. When the Mach number exceeded 1.60 considerable flow asymmetry was observed. Shock wave motion was observed at all these Mach numbers and was investigated using high speed Schlieren movies and high speed wall pressure measurements.²⁹ The amplitude of the shock oscillation increased with increasing Mach number. They theorized that the shock motion is triggered by high frequency pressure fluctuations in the incoming boundary layer while the frequencies of the shock motion are related to the resonance frequencies of the downstream

subsonic duct flow. Reference 30 by Ikui, et al. considered ducts with relatively large divergence and is not, therefore, directly applicable to the current study.

The early investigators were mainly concerned with the overall pressure recovery characteristics of constant area supersonic diffusers. Johnson and Wu³¹ compiled a summary of these early diffuser pressure recovery results. Typically, the static wall pressure was found to rise in a continuous fashion over a distance of 8 to 12 duct diameters with the pressure recovery slightly lower than that occurring for a single normal shock at the same undisturbed Mach number. In more recent results, Waltrup and Billig³², Merkli²⁴, Mateer et al.³³, Mateer and Viegas²⁵, Om, et al.³⁴, and Om and Childs³⁵ have studied various parametric trends in the pressure rise. Some difficulty arises when comparing these investigations since the data is presented in various formats and the parameters are not always non-dimensionalized in the same way. The start of the interaction is typically defined as the point at which the wall pressure begins to rise, and flow parameters at this location are referred to as undisturbed values. In the more recent papers, the wall pressure is normalized by the undisturbed pressure, P_u , or the upstream stagnation pressure, P_0 , and the axial distance is measured from the start of the interaction and normalized by the undisturbed boundary layer thickness, δ_u . Several trends are noticed in the wall pressure distribution when plotted in such a manner. An initial steep pressure rise is followed by a region of nearly constant slope in the pressure distribution. The shape of the wall pressure profile displays a strong dependence on Mach number, M_u , and confinement parameter, δ_u/r , and a weaker dependence on Reynolds number. The slope in the initial pressure rise increases slightly with increasing unit Reynolds number, Re/m . This result seems to be valid for both single and multiple shock systems (possibly because of a free interaction effect at the start of the interaction). Conflicting Mach number dependencies were found. For the single shock, Om, et al.³⁴ found the slope of the initial pressure rise tends to increase with increasing Mach number and constant unit Reynolds number, Re/m , while Mateer and Viegas²⁵ found the initial slope to decrease with increasing Mach number and constant Reynolds number based on downstream distance, Re_s . The Reynolds number based

on undisturbed boundary layer thickness, Re_{δ_u} , was not held constant in either experiment. Om, et al.³⁴ noted that Re_{δ_u} decreased at a faster rate, as Mach number decreased, in Mateer and Viegas' ²⁵ series of experiments than in their own, and suggest that this is the cause of the conflicting Mach number dependencies. This observation implies that the proper Reynolds number to use in characterizing the flow is one based on an undisturbed boundary layer thickness. One consistent Mach number effect is that the length of the interaction increases with increasing Mach number. Considering the effect of confinement, one observes that the pressure recovery decreases with increasing δ_u/r and fixed Mach number and unit Reynolds number³⁵. This effect may be due to increased losses as the shock system becomes a multi-shock structure and to a greater increase in the displacement thickness for the multiple shocks as opposed to the single shock system. The increase in displacement thickness effectively accelerates the subsonic flow after the shock system causing a reduction in static pressure.

A description of the local mean and fluctuating flow characteristics will now be given, with the single shock interaction and multiple shock interaction being considered separately. The confined, separated single normal shock interaction shown in Figure 3 is fairly similar to the unconfined, separated normal shock interaction (Figure 2). Mateer and Viegas²⁵ showed that the tendency toward separation increased as δ_u/r decreased, i.e. flow confinement delays separation. As was found for the unconfined case, the height of the bifurcation above the wall and the tendency toward separation increases as Mach number, M_u , increases and as unit Reynolds number, Re/m , decreases. Mateer et al.³³ showed that the length of the separation scales directly with the undisturbed boundary layer thickness. Their measurements, made with the use of a fast responding, embedded hot wire separation detector, indicated some unsteadiness in the separation region. In this study, surveys of the mean and fluctuating flow were also made using pitot pressure and hot wire probes. Upstream of the shock, a peak in the axial mass flux fluctuations was observed in the boundary layer, away from the wall. An order of magnitude increase in the mass flux fluctuations was observed going through the interaction followed by a relaxation and diffusion of the fluctuating quantities downstream of the

interaction leading to lower, nearly constant levels through the boundary layer out into the mean flow. At transonic speeds, the interpretation of hot wire data is difficult due to the presence of shock waves on the probe. As a result, Matecr et al.³³ commented that the accuracy of the hot wire data may be poor for the range of local Mach numbers, $1.0 < M < 1.25$. They also noted the presence of a supersonic tongue at an initial Mach number of 1.5 but did not mention the presence of a slip line in the flow. Om, et al.³⁴ made a detailed study of the single shock interaction in an axisymmetric duct using pitot and static pressure probes to map out the mean flow, and an alcohol injection technique to detect separation. They found no separation at a Mach number of 1.28, incipient separation at $M_u = 1.37$, and separated flow at $M_u = 1.48$. Their measurements also showed an embedded supersonic tongue for $M_u = 1.28$, 1.37, and 1.48 which increased with size as Mach number increased. The shape of their supersonic tongue was different than that found in external interactions^{18,20,21} in that the thickness of the tongue increased with downstream distance. Om, et al.³⁴ observed that the confinement effect tended to increase the size of the supersonic tongue. By increasing the unit Reynolds number, the confinement effect, and correspondingly the size of the supersonic tongue, were reduced. A slip line was detected at $M_u = 1.48$, but was too weak to be measured at Mach numbers of 1.37 and 1.28. In one of the few detailed studies performed at higher Mach numbers, Cuffel and Back³⁶ investigated a Mach 2.92 interaction using pressure and temperature probes. In spite of relatively high confinement levels, only a single, separated normal shock was reported. Wall cooling was present in this experiment and may have had sufficient effect to change the trends observed in other adiabatic wall experiments.

Using the same test section, Om, et al.³⁴ found single normal shocks with $M_u = 1.48$, $Re/m = 4.92 \times 10^6$, and $\delta_w/r = 0.081$ while Om and Childs³⁵ found a repeated nearly normal shock pattern at essentially the same Mach number and Reynolds number, $M_u = 1.49$, $Re/m = 4.90 \times 10^6$, and higher confinement levels, $\delta_w/r = 0.198$. Om and Childs³⁵ investigated this multiple shock interaction making detailed pitot and static pressure surveys. A qualitative sketch of a two shock system is shown in Figure 4. The repeated, nearly normal shock

interaction investigated by Om and Childs³⁵ consisted of several shocks whereas the sketch in Figure 4 shows only two shocks. In their study, the boundary layer displacement thickness was found to increase rapidly through the first shock, then decrease slightly before increasing again across the second shock. This pattern was repeated through the whole interaction. The momentum thickness distribution exhibited similar behavior. A slip line was generated at the bifurcation point of the first shock and persists through the following, weaker shocks which do not appear to generate slip lines. Following the interaction, the pitot pressure profiles remain nonuniform even after the static pressure profiles have become uniform. The flow just outside the boundary layer stayed supersonic through the whole interaction, while the flow in the core region went subsonic after each shock, then reaccelerated to supersonic speed before the next shock, the distance between successive shocks decreasing with downstream distance from the start of the interaction. At the end of the interaction, the flow is still mixed supersonic/subsonic in nature, with the supersonic portion of the flow following the last shock isentropically decelerating to subsonic velocities. Recently, an investigation of the three-dimensional nature of the shock wave/turbulent boundary layer interaction in a square duct was made by Chriss, et al.¹⁵ using a one-component LDV system to make non-coincident measurements of the three velocity components. At Mach 1.3 an unseparated single shock system was found that was largely two-dimensional with the notable exception of a supersonic tongue near the corner. A separated, multiple normal shock system was found at Mach 1.6 that included a higher level of three-dimensionality especially near the corners where the size of the supersonic tongue was greater than at mid-span. The extent of flow separation was also greatest in the corners. Considerable high frequency shock motion was observed and caused distinctly bimodal velocity histograms in the LDV measurements near the shock. Schlieren photographs revealed what appears to be a weak reflected shock generated where the trailing leg of the initial, bifurcated shock intersects the boundary layer. Measurements were not made in the near wall portion of the boundary layer, and boundary layer thickness parameters were not reported nor was any turbulence information apparently obtained. Data for the spanwise component of

velocity were not included in this paper either but are expected to be released at a later date. In the only other detailed study of the mean flow in a confined multiple shock interaction, Waltrup and Billig³² investigated the flow at Mach numbers in the range $1.53 < M_u < 2.72$, various unit Reynolds numbers ranging from $2.2 \times 10^7 < Re/m < 6.3 \times 10^7$, and confinement levels ranging from $0.005 < \theta_w/r < 0.020$. At $M_u = 1.53$ they observed a single normal shock. At all other Mach numbers tested, they reported finding an oblique shock system and postulated that the shock system was a series of weak reflected oblique shocks with totally supersonic flow following each shock.

The Reynolds number effect on the shock structure is clearly seen by comparing the results of Mateer, et al.³³ ($Re/m = 2.3 \times 10^7$, $M_u = 1.5$, $\delta_w/r = 0.202$), who found a single normal shock, to those of Om and Childs³⁵ ($Re/m = 4.9 \times 10^6$, $M_u = 1.49$, $\delta_w/r = 0.198$) who found a repeated normal shock system. Increasing the Reynolds number for almost identical Mach numbers and confinement parameters causes the shock structure to shift from a multiple to a single shock system. The effect of Mach number on the shock structure is not clear, but a tendency toward repeated shock systems as Mach number increases is evidenced by the increase in the length of the pressure rise with increasing Mach number. The results of Waltrup and Billig³² suggest that a single normal shock may not exist in high Mach number confined flows, even with small δ_w/r . However, the results of Cuffel and Back³⁶ indicate that a single normal shock can exist in a high Mach number flow with relatively large δ_w/r . A comparison of these two works also contradicts the expected Reynolds number effect (increasing Re/m leading to a single shock system). The cause of this apparent discrepancy is not clear, indicating the need for further work to establish what types of shock structures can be expected at higher Mach numbers, i. e. Mach numbers of approximately 1.8 and above.

In reviewing the body of experimental work related to the internal shock wave/turbulent boundary layer interaction, several areas requiring further study are evident. Further work is needed to determine when the transition from a single normal shock to multiple normal shocks to repeated oblique shocks occurs at various Mach numbers, Reynolds numbers, and

confinement parameters. The exact nature of the repeated oblique shock system is also unclear. From the existing data it is difficult to determine if the oblique shocks are strong (subsonic flow after each shock) or weak (supersonic flow after each shock). The steadiness of the interaction in a constant area duct is also questionable. Small scale, high frequency motion of the shock would lead to false turbulence measurements. This effect should be investigated further. The topic of unsteady shock structures has received more attention in the planar studies. This may indicate that the axisymmetric geometry is inherently steadier or it may simply indicate that shock motion is easier to detect in planar geometries. Conspicuously absent are any measurements of the turbulence structure in a repeated system of either normal or oblique shocks. The amount of turbulence data available for the confined single normal shock interaction is also severely limited.

C. NUMERICAL WORK

Numerous researchers have applied numerical techniques for solving the mass averaged Navier-Stokes equations to external or unconfined shock wave/boundary layer interactions, including MacCormack and Baldwin³⁷, Wilcox³⁸, Shang and Hankey³⁹, Deiwert⁴⁰, Hung and MacCormack⁴¹⁻⁴³, and Settles, et al.⁴⁴. These studies all demonstrate the ability of shock capturing finite difference techniques to predict the qualitative features of the interaction. With the turbulent calculations, close quantitative agreement, especially for separated flows is strongly dependent on the turbulence model employed. In a series of papers, researchers at NASA-Ames have studied a variety of shock wave/turbulent boundary layer interaction flows.^{25,33,34,45-49} Both confined and unconfined flows were considered. These calculations employed the second-order accurate, explicit, time-splitting, finite difference method of MacCormack⁵⁰ modified by MacCormack's explicit-implicit characteristics scheme.⁵¹ Several turbulence models were employed including a variety of algebraic eddy-viscosity models, the one-equation model of Rubesin⁵², and the two-equation models of Jones and Launder⁵³ and Wilcox and Rubesin.⁵⁴ All of the calculations showed good qualitative agreement with

experimental results. Quantitative agreement with experimental data was more difficult to obtain, especially when boundary layer separation was present. Experimental measurements of surface pressure distributions, skin friction, separation and reattachment locations, mean velocity profiles, and turbulence kinetic energy profiles were used to evaluate the various computations. While none of the models was clearly superior in all respects, the higher order models were found to be more universally applicable and typically offered better accuracy than the lower order models. The Wilcox-Rubesin two equation eddy viscosity model⁵⁴ emerged as being superior for general use in shock wave/boundary layer interaction flows. However, a deficiency of the higher order, eddy viscosity models is that they give poor predictions of velocity profiles downstream of the single shock wave/boundary layer interaction, and this may limit the ability of the higher order eddy viscosity models to predict multiple shock wave/boundary layer interactions.

In all of the numerical investigations mentioned above, only single shock interactions have been calculated. To the author's knowledge, no calculations of multiple normal or strong oblique shock wave/turbulent boundary layer interactions have been performed. Several reported calculations of supersonic inlet flows have shown the ability to calculate single terminal shocks and reflected weak oblique shocks in confined ducts of various geometries. Fairly coarse grids were used in these calculations, thus the details of the flow are poorly resolved. The calculations of Knight⁵⁵⁻⁵⁷, Kumar⁵⁸⁻⁶⁰, Drummond and Weidner⁶¹, Talcott and Kumar⁸, Coakley and Hsieh⁶², and Hunter, et al.⁶³ have all employed some form of MacCormack's finite-difference method. Other techniques have been employed as well. For example, Paynter and Chen⁶⁴ used a zonal analysis and Chaussee and Pulliam⁶⁵ used the implicit finite-difference method of Beam and Warming.⁶⁶

III. NUMERICAL TECHNIQUES

The techniques used for the numerical portion of this investigation are presented in this chapter. The computational strategy was to employ existing numerical techniques, typical of those being used in industrial and research applications, and to use existing software when possible. The NASCRIN computer code⁵⁹, obtained from Dr. Ajay Kumar at NASA-Langley Research Center, has been extensively modified for the current application. These modifications included work with the outflow and no-slip boundary conditions. A reference plane characteristics-type subsonic outflow boundary condition was incorporated and the no-slip wall boundary conditions were modified to use a normal momentum equation in calculating wall pressure. The original code contained the algebraic Baldwin-Lomax turbulence model⁶⁷ which is a widely used model in applied research and development activities. As was mentioned in the literature review, the two-equation Wilcox-Rubesin turbulence model⁵⁴ has been shown to be effective for use in calculating shock wave/boundary layer interaction flows^{34,48} giving slightly better performance than the more widely used Jones-Launder model⁵³. For these reasons, the Wilcox-Rubesin model was selected for use and was incorporated into the modified NASCRIN code. Wall function boundary conditions for use with the Wilcox-Rubesin model have also been incorporated. The wall function method helps avoid numerical problems due to the extremely stiff nature of the turbulence model equations near the wall and also offers a considerable savings in computer time. Finally, the NASCRIN code has been modified with respect to data input and output and computational grid generation. In the remainder of this chapter, the details of these numerical techniques are given.

A. GOVERNING EQUATIONS

The governing equations for the mean flow are the same as those used by Kumar,^{58,59} i. e. the conservation form of the mass averaged, time-dependent Navier-Stokes equations. A

generalized coordinate transformation is applied to take the equations from the physical (x,y) plane to the computational (ξ, η) plane with a unit grid spacing being used in the mutually orthogonal ξ and η directions. The coordinate transformation is applied such that the equations remain in strong conservation form. The resulting equations are:

$$\frac{\partial \mathbf{U}}{\partial t} + \frac{\partial \mathbf{M}}{\partial \xi} + \frac{\partial \mathbf{N}}{\partial \eta} = 0 \quad (1)$$

where the vectors \mathbf{U} , \mathbf{M} , and \mathbf{N} are

$$\mathbf{U} = J \begin{bmatrix} \rho \\ \rho u \\ \rho v \\ \rho H - p \end{bmatrix} \quad (2)$$

$$\mathbf{M} = \begin{bmatrix} \rho \bar{u} \\ \rho u \bar{u} + y_{\eta} \sigma_x - x_{\eta} \tau_{xy} \\ \rho v \bar{u} + y_{\eta} \tau_{xy} - x_{\eta} \sigma_y \\ \rho H \bar{u} - p \bar{u} + y_{\eta} (u \sigma_x + q_x) - x_{\eta} (v \sigma_y + q_y) + \tau_{xy} (v y_{\eta} - u x_{\eta}) \end{bmatrix} \quad (3)$$

$$\mathbf{N} = \begin{bmatrix} \rho \bar{v} \\ \rho u \bar{v} - y_{\xi} \sigma_x + x_{\xi} \tau_{xy} \\ \rho v \bar{v} - y_{\xi} \tau_{xy} + x_{\xi} \sigma_y \\ \rho H \bar{v} - p \bar{v} - y_{\xi} (u \sigma_x + q_x) + x_{\xi} (v \sigma_y + q_y) + \tau_{xy} (-v y_{\xi} + u x_{\xi}) \end{bmatrix} \quad (4)$$

The contravariant velocities are defined as

$$U = \bar{u}/J = \overline{\mathbf{V}} \cdot \nabla \xi = (y_{\eta} u - x_{\eta} v)/J \quad (5)$$

$$V = \bar{v}/J = \overline{\mathbf{V}} \cdot \nabla \eta = (-y_{\xi} u + x_{\xi} v)/J \quad (6)$$

where $\overline{\mathbf{V}}$ is the velocity vector in the (x,y) plane. The contravariant velocity components U and V represent the velocities perpendicular to lines of constant ξ and η , respectively. The Jacobian of the transformation is given as

$$J = x_{\xi}y_{\eta} - x_{\eta}y_{\xi} \quad (7)$$

and the metrics of the transformation are defined as

$$y_{\eta} = \xi_x J \quad x_{\eta} = -\xi_y J \quad y_{\xi} = -\eta_x J \quad x_{\xi} = \eta_y J . \quad (8)$$

The subscripts denote partial differentiation, for example $y_{\eta} \equiv \frac{\partial y}{\partial \eta}$. The total stresses, assumed

to be comprised of a laminar and a turbulent contribution, are defined by

$$\sigma_x = \sigma_x^l + \sigma_x^t \quad (9)$$

$$\sigma_y = \sigma_y^l + \sigma_y^t \quad (10)$$

$$\tau_{xy} = \tau_{xy}^l + \tau_{xy}^t \quad (11)$$

The laminar stresses are given by

$$\sigma_x^l = p + \frac{2}{3}\mu_l \frac{\partial v}{\partial y} - \frac{4}{3}\mu_l \frac{\partial u}{\partial x} \quad (12)$$

$$\sigma_y^l = p + \frac{2}{3}\mu_l \frac{\partial u}{\partial x} - \frac{4}{3}\mu_l \frac{\partial v}{\partial y} \quad (13)$$

$$\tau_{xy}^l = -\mu_l \left(\frac{\partial u}{\partial y} + \frac{\partial v}{\partial x} \right) \quad (14)$$

and the turbulent stresses are obtained using the Boussinesq eddy viscosity assumption described below. The total heat flux is also made up of a laminar and turbulent contribution,

$$q_x = - \left(\frac{\mu_l}{Pr_l} + \frac{\mu_t}{Pr_t} \right) \frac{\partial h}{\partial x} \quad (15)$$

$$q_y = - \left(\frac{\mu_l}{Pr_l} + \frac{\mu_t}{Pr_t} \right) \frac{\partial h}{\partial y} . \quad (16)$$

All of the derivatives with respect to x and y are actually calculated in the transformed coordinates ξ and η . As an example, the derivative of h with respect to y is calculated from

$$\frac{\partial h}{\partial y} = (-h_\xi x_\eta + h_\eta x_\xi)/J \quad (17)$$

In these equations ρ, u, v , and p are the density, mean velocity in the x -direction, mean velocity in the y -direction, and static pressure. H is the stagnation enthalpy and h is the static enthalpy. The laminar viscosity, μ_l , is obtained from the Sutherland viscosity law while the turbulent viscosity, μ_t , is calculated from the turbulence models described below. The laminar and turbulent Prandtl numbers are taken as $Pr_l = 0.72$ and $Pr_t = 0.90$, respectively. In the energy equation, the dependent variable is written as $\rho H - p$ and is physically interpreted as the total internal energy per unit volume. One additional relation, beyond the turbulence model for μ_t , is required to close this set of equations. This is taken as the ideal gas law

$$p = \rho R T \quad (18)$$

where R is the gas constant and T is the static temperature.

Implicit in this formulation is the Boussinesq eddy viscosity assumption. The basic assumption is that the apparent turbulent stresses, τ_{ij}^t , which arise from the mass averaging operation, are related to the mean rate of strain through a turbulent or eddy viscosity, μ_t . In this study, an isotropic eddy viscosity is employed which has the same numerical value for all elements of the stress tensor at a point, i.e. the eddy viscosity is independent of direction. A mathematical statement of the eddy viscosity assumption is written as

$$\tau_{ij}^t = \overline{\rho u_i' u_j'} = -\mu_t \left(\frac{\partial u_i}{\partial x_j} + \frac{\partial u_j}{\partial x_i} \right) + \frac{2}{3} \delta_{ij} \left(\mu_t \frac{\partial u_k}{\partial x_k} + \rho k \right) \quad (19)$$

where k is the turbulence kinetic energy defined as

$$k = \frac{1}{2} \overline{u_k' u_k'} \quad (20)$$

The primes denote fluctuating quantities and the overbars indicate a mass average is taken. Equation (19) is the constitutive relation between the turbulent stresses and the mean rates of strain that is used to calculate the turbulent stress required in Equations (9-11). When expanded, Equation (19) is identical in form to Equations (12-14) with p replaced by ρk and

the l subscript replaced by t . The ρk term represents an apparent pressure due to turbulent fluctuations. The eddy viscosity assumption does not by itself constitute a turbulence model. Rather, it defines the framework in which a turbulence model may be developed and applied. All that remains in the turbulence modeling procedure is to specify μ_t and k in terms of known quantities.

By analogy to the kinetic theory for molecular viscosity, the turbulent viscosity is modeled by

$$\mu_t = \rho V_t L_t \quad (21)$$

where V_t and L_t are characteristic velocity and length scales of the turbulent flow. In general, these characteristic scales vary from point to point in the flow and may depend on the history of the flow both upstream and downstream of the location of interest. Thus, a fundamental distinction exists between the laminar viscosity, which is a local property of the fluid, and the turbulent viscosity, which is a function of the particular flow field. The two turbulence models employed in this investigation, one due to Baldwin and Lomax⁶⁷ and the other to Wilcox and Rubesin⁵⁴, are based on this framework.

1. BALDWIN -LOMAX TURBULENCE MODEL

The Baldwin-Lomax model⁶⁷ is a widely used two-layer, algebraic, isotropic eddy viscosity turbulence model. The term algebraic refers to the type of relations used to calculate the turbulent length and velocity scales. This is a two-layer model in that the turbulent viscosity is calculated using two distinct formulations in two distinct layers, the inner layer close to a solid wall, and the outer layer away from the wall. A smooth transition between the two formulations is enforced as follows

$$\mu_t = \begin{cases} (\mu_t)_{\text{inner}} & y \leq y_{\text{crossover}} \\ (\mu_t)_{\text{outer}} & y_{\text{crossover}} < y \end{cases} \quad (22)$$

Here, y is the normal distance from the wall and the crossover point is the closest location to the wall at which the outer and inner turbulent viscosities are equal. In the inner region, the Prandtl-Van Driest formulation is used,

$$(\mu_t)_{\text{inner}} = \rho L_t^2 |\omega| \quad (23)$$

where the turbulent length scale is

$$L_t = \kappa y D, \quad (24)$$

the turbulent velocity scale is $L_t |\omega|$, κ is von Karman's constant, and $|\omega|$ is the magnitude of the vorticity

$$|\omega| = \sqrt{\left(\frac{\partial u}{\partial y} - \frac{\partial v}{\partial x}\right)^2} \quad (25)$$

D is the Van Driest damping factor

$$D = [1 - \exp(-y^+/A^+)] \quad (26)$$

and

$$y^+ = \frac{y \sqrt{\rho_w \tau_w}}{\mu_w} \quad (26)$$

The outer turbulent viscosity is calculated from

$$(\mu_t)_{\text{outer}} = C_{cl} C_{cp} \rho F_{\text{wake}} F_{\text{kleb}}(y). \quad (27)$$

In this expression, C_{cl} is the Clauser constant, C_{cp} is an additional constant, and $F_{\text{kleb}}(y)$ is the Klebanoff intermittency function given by

$$F_{\text{kleb}}(y) = \left[1 + 5.5 \left(\frac{C_{\text{kleb}} y}{y_{\text{max}}} \right)^6 \right]^{-1}. \quad (28)$$

The wake function is calculated from

$$F_{\text{wake}} = y_{\text{max}} F_{\text{max}} \quad (29)$$

where y_{max} is the y location of the peak in the function

$$F(y) = y |\omega| D \quad (29)$$

and $F_{\text{max}} = F(y_{\text{max}})$. The turbulent length scale in the outer region is proportional to y_{max} and the turbulent velocity scale is proportional to F_{max} . Thus, the distribution of vorticity in the

outer region is used to establish these outer scales. Baldwin and Lomax⁶⁷ noticed in their original paper that the function $F(y)$ can develop multiple peaks in the vicinity of a shock wave/boundary layer interaction. If the wrong peak is selected, the function F_{wake} will be incorrectly evaluated. Visbal and Knight⁶⁸ investigated this effect in more detail. Their results indicated that two main peaks develop in the separation region of a shock wave/boundary layer interaction. Selection of the inner peak causes artificially low values of F_{wake} , while selection of the outer peak gave physically more reasonable results leading them to recommend use of the outer peak. They also noted that near the separation point, where the wall shear stress goes to zero, the Van Driest damping function unrealistically vanishes causing low values of the computed turbulent viscosity. The use of the local shear stress, instead of the wall shear stress, avoided this problem. The constants C_{cp} and C_{kleb} exhibited a Mach number dependence. A value of $C_{cp}=2.08$ was recommended for a Mach 3.0, nearly adiabatic flat plate boundary layer. No specific recommendation concerning C_{kleb} in a compressible flow was made. The original values of the model constants are⁶⁷

$$\begin{aligned}
 A^+ &= 26 \\
 C_{cp} &= 1.6 \\
 C_{kleb} &= 0.3 \\
 \kappa &= 0.4 \\
 C_{cl} &= 0.0168
 \end{aligned}
 \tag{30}$$

The kinetic energy term, pk , in the constitutive relation, Equation (19), is set to zero.

2. WILCOX-RUBESIN TURBULENCE MODEL

The Wilcox-Rubesin turbulence model⁵⁴ is a two-equation, eddy viscosity model. Two partial differential equations are solved for the turbulence kinetic energy and the specific turbulence dissipation. These two quantities are then used in a set of algebraic relations to obtain the turbulent length and velocity scales which are combined to obtain a turbulent viscosity. Wilcox and Rubesin⁵⁴ preferred to interpret the quantity k which will appear in the

turbulence model equations as a turbulence mixing energy rather than the total turbulence kinetic energy. The turbulence mixing energy is related to the fluctuating velocity component which is perpendicular to the mean flow direction, but was not precisely defined by Wilcox and Rubesin⁵⁴. In this work, the quantity k is taken as the total turbulence kinetic energy. This choice is in agreement with that of Viegas and Horstman⁴⁸ in their implementation of the Wilcox-Rubesin model. The specific turbulence dissipation, ω , defined as the rate of dissipation of turbulence kinetic energy per unit of turbulence kinetic energy, is related to the dissipation of turbulence kinetic energy by

$$\omega = \frac{\varepsilon}{\beta^* k} \quad (31)$$

where β^* is a constant and ε is the dissipation of turbulence kinetic energy used in the Jones-Launder model⁵³. The turbulent viscosity is calculated from

$$\mu_t = \rho \gamma^* \frac{k}{\omega} \quad (32)$$

where k and ω are obtained from the turbulence model equations for ρk and $\rho \omega^2$:

$$\frac{\partial(\rho k)}{\partial t} + \frac{\partial(\rho u_j k)}{\partial x_j} + \tau_{ij} \frac{\partial(u_i)}{\partial x_j} + \beta^* \rho \omega k - \frac{\partial}{\partial x_j} \left[(\mu_t + \sigma^* \mu_t) \frac{\partial(k)}{\partial x_j} \right] = 0 \quad (33)$$

$$\begin{aligned} \frac{\partial(\rho \omega^2)}{\partial t} + \frac{\partial(\rho u_j \omega^2)}{\partial x_j} + \gamma \frac{\omega^2}{k} \tau_{ij} \frac{\partial(u_i)}{\partial x_j} + \left[\beta + 2\sigma \left(\frac{\partial L_t}{\partial x_k} \right)^2 \right] \rho \omega^3 \\ - \frac{\partial}{\partial x_j} \left[(\mu_t + \sigma \mu_t) \frac{\partial(\omega^2)}{\partial x_j} \right] = 0 \end{aligned} \quad (34)$$

The turbulent length scale is

$$L_t = \frac{\sqrt{k}}{\omega} \quad (35)$$

Five terms appear in each of the turbulence model equations for k and ω^2 , Equations (33) and (34). From left to right, these terms are the time rate of change followed by the convection, production, viscous dissipation, and viscous diffusion terms. A viscous damping term, γ^* , is included in the expression for the turbulent viscosity and is given by

$$\gamma^* = [1 - (1 - \lambda^2) \exp(-Re_t/R_k)] \quad (36)$$

To allow a different level of damping in the ω^2 equation, a second damping term, γ , is defined by

$$\gamma\gamma^* = \gamma_\infty [1 - (1 - \lambda^2) \exp(-Re_t/R_\omega)] \quad (36)$$

These viscous damping terms were required in the model to correctly simulate the near wall region where molecular viscosity dominates. The Reynolds number of turbulence is expressed as

$$Re_t = \frac{\rho \sqrt{k} L_t}{\mu} \quad (37)$$

The model closure coefficients are

$$\begin{aligned} \beta &= \frac{3}{20} & \beta^* &= \frac{9}{100} & \sigma &= \sigma^* = \frac{1}{2} \\ \gamma_\infty &= \frac{10}{9} & \lambda &= \frac{1}{11} & R_k &= 1 \end{aligned} \quad (38)$$

$$R_\omega = 2.0$$

Viegas and Horstman⁴⁹ found that calculations with the original value of $\gamma_\infty = 10/9$ underpredicted the wall shear stress in a flat plate equilibrium boundary layer by 27% and recommended that a value of $\gamma_\infty = 0.90$ be used instead. This set of model equations, when solved in conjunction with the mean flow equations, gives the turbulent viscosity, μ_t , and the turbulent kinetic energy, k , required in Equation (19). In Wilcox and Rubesin's⁵⁴ original work, terms were added to the constitutive relation, Equation (19), to allow for non-aligned stress and strain. These terms, intended as a correction to the isotropic model for non-isotropic effects, were found to cause numerical difficulties at times,⁴⁹ especially in calculations of

shock wave/boundary layer interaction flows, and have therefore not been included in the current formulation.

B. NUMERICAL SOLUTION METHOD

The set of governing equations given above are solved using the original explicit, time-dependent, second-order accurate, predictor-corrector, finite-difference method of MacCormack⁶⁹. A shock capturing approach on a fixed grid is taken. This method has the advantages of being easily understood and implemented and is highly vectorizable. In this computational approach, the solution is advanced in time from some initial value plane to a final converged, steady state solution. The advantage of using a time-dependent method to obtain the steady state solution is seen by considering the nature of the governing partial differential equations. The governing equations are hyperbolic in time, but display a mixed elliptic-hyperbolic nature in the spatial coordinates due to the mixed subsonic-supersonic velocities of the strongly shocked boundary layer flow under consideration. A steady state, spatial marching technique would require different computational procedures in the subsonic and supersonic portions of the flow. This is avoided by using the time-dependent approach to march the solution in time until the desired steady solution is obtained, allowing the spatial differences to be performed in the same manner regardless of the local flow velocity.

In MacCormack's method⁶⁹ the solution is progressed from one time plane to the next in two steps, the predictor and corrector. The same finite-difference method is used to solve both the mean flow and turbulence partial differential equations. However, to illustrate the method consider only the mean flow equations, Equation (1), for which the predictor-corrector sequence is

$$U_p^{n+1} = U^n - \Delta t / \Delta \xi (D_+ M^n) - \Delta t / \Delta \eta (D_+ N^n) \quad (39)$$

$$U_c^{n+1} = U^n - \Delta t / \Delta \xi (D_- M_p^{n+1}) - \Delta t / \Delta \eta (D_- N_p^{n+1}) \quad (40)$$

$$U^{n+1} = 1/2(U_p^{n+1} + U_c^{n+1})$$

The predictor step is given by Equation (39) and the corrector step is given by Equations (40). In these expressions, the superscript n denotes the previous time plane, and the superscript $n+1$ denotes the new time plane. The subscripts p and c indicate that predicted and corrected values of the flow variables are used to evaluate the vector. The time step is Δt and the grid spacings are $\Delta \xi$ and $\Delta \eta$. The finite difference operators D_+ and D_- need further explanation. The operator D_+ indicates that first order accurate forward differences are used to evaluate the outer spatial derivatives in the governing mean and turbulence equations while first order backward differences are used for all derivatives in the shear stress and heat flux terms, Equations (12-16,19), and for the inner derivatives of the diffusion terms in the turbulent kinetic energy and turbulent dissipation rate equations, Equations (33) and (34). The operator D_- indicates the opposite differencing scheme, first order backward differences on all outer derivatives and first order forward differences on all inner derivatives. In the original MacCormack scheme, central differences were used on all inner cross-derivatives in the shear stress and heat flux terms. Central differences were not used on these terms in the present code. This allows a simpler algorithm which saves both computer memory space and execution time. The use of one-sided differences on these cross derivatives still retains second-order accuracy for the predictor-corrector sequence and is expected to have only slight, if any, effect on the computed results.⁷⁰ The sequence of operators, D_+ , D_- for the predictor-corrector steps is reversed at every time step so that the repeated sequence of operators is D_+ , D_- , D_+ , D_- .

A fourth-order numerical damping option⁵⁹ is included in the code. It is available for use when strong shocks are present in the flow and is required to avoid excessively large numerical oscillations in the computed results near such shocks.

C. BOUNDARY AND INITIAL CONDITIONS

The numerical procedure described above is used to solve the governing differential equations at all grid locations except the boundaries. At each new time plane in the solution procedure, appropriate boundary conditions must be applied. The philosophy taken in this

work is that while the boundary points represent only a fraction of the computational grid points, the boundary conditions applied at these points exert a large influence on the computed results. Consequently, when formulating and applying the boundary conditions, care was taken to realistically model the actual physical constraints. In the following sections, the inflow, outflow, solid wall, and symmetry plane boundary conditions are treated separately. An initial value plane must also be specified to start the calculation. The initial value plane should be selected such that large numerical transients which might cause the solution to become unstable are avoided. The choice of initial value plane could also affect the overall time required for convergence to a steady solution and could conceivably determine which steady state solution is reached, since the uniqueness of the solution is not assured. The actual initial value plane used for each calculation is stated where that calculation is discussed.

1. INFLOW AND SYMMETRY BOUNDARY CONDITIONS

The inflow and symmetry boundary conditions are treated together since they are both relatively simple. At the inflow boundary the flow is assumed to be supersonic except in the near wall regions where the flow may be subsonic. For these conditions the governing equations are either hyperbolic or parabolic and one would not expect information to propagate upstream. Accordingly, the primitive variables u , v , T , p , k , and ω are held fixed at specified incoming values. At a symmetry boundary, the symmetric quantities u , T , and p are obtained from a one point (zeroth order) extrapolation (equivalent to zero normal gradient) while the antisymmetric quantity v is set to zero. The turbulence quantities k and ω are also obtained from one point extrapolations.

2. OUTFLOW BOUNDARY CONDITIONS

Several options are allowed at the outflow boundary. The turbulence variables k and ω are extrapolated at both subsonic and supersonic outflow points using a zeroth order extrapolation. With supersonic outflow, information is physically expected to be swept out of

the grid so that either zeroth or first order extrapolation may be used for u , v , p , and T . This type of extrapolation is also applied at the near wall subsonic points in a parabolic boundary layer type flow. The reference plane characteristic scheme, described below, may also be used for supersonic outflow conditions. When the flow is subsonic at the outflow boundary, information can propagate upstream and extrapolation of the mean flow variables is not physically consistent. As will be shown, one of the mean flow variables u , v , p , or T must be specified at the exit. Rudy and Strikwerda⁷¹ show that a proper treatment of a subsonic boundary is needed to prevent the numerical reflection of information at the boundary. A simple treatment such as extrapolating u , v , and T and holding p fixed can cause the reflection of pressure waves back into the computational grid. Low frequency pressure waves can actually be trapped in the computational grid. To avoid such problems, a non-reflective, reference plane characteristics scheme, similar to that of Cline^{72,73} has been implemented.

A method of characteristics analysis of the non-conservative form of the governing equations is performed to find the characteristic and compatibility equations. The ξ direction is perpendicular to the boundary and the η direction is parallel to the boundary. All η derivatives and viscous terms are evaluated using finite differences and are treated as source terms. The resulting set of compatibility and associated characteristic relations are

$$dp - \Omega_1 dp = \Psi_4 dt \quad \text{along} \quad \frac{d\xi}{dt} = U \quad (41)$$

$$\Omega_2 du + \Omega_3 dv = (\Omega_2 \Psi_2 + \Omega_3 \Psi_3) dt \quad \text{along} \quad \frac{d\xi}{dt} = U \quad (42)$$

$$\begin{aligned} \Omega_4 du - \Omega_5 dv + dp &= (\Omega_1 \Psi_1 + \Omega_4 \Psi_2 - \Omega_5 \Psi_3 + \Psi_4) dt \\ \text{along} \quad \frac{d\xi}{dt} &= U + a \int \sqrt{x_\eta^2 + y_\eta^2} \end{aligned} \quad (43)$$

and

$$\begin{aligned} -\Omega_6 du - \Omega_7 dv + dp &= (\Omega_1 \Psi_1 - \Omega_6 \Psi_2 + \Omega_7 \Psi_3 + \Psi_4) dt \\ \text{along} \quad \frac{d\xi}{dt} &= U - a \int \sqrt{x_\eta^2 + y_\eta^2} \end{aligned} \quad (44)$$

The Ω_i and Ψ_i are defined in Appendix A. The contravariant velocity U was previously defined in Equation (5) and a is the speed of sound defined as

$$a = \sqrt{\gamma RT} \quad (45)$$

The total derivatives in Equations (41-44) are applied along the characteristics. The three characteristic directions are obtained from the equations for $d\xi/dt$. When the flow is supersonic in the ξ direction, all three characteristics extend backwards into the computational domain from the boundary, indicating that the values of u , v , p , and T at the exit are determined from the upstream flow. When the flow is subsonic in the ξ direction, the first two characteristics extend into the domain while one extends out of the computational domain, such that one of the flow variables must be specified. At an inflow boundary, this same analysis shows that four flow variables must be specified for supersonic inflow, while only three flow variables should be specified for subsonic inflow.

3. SOLID WALL BOUNDARY CONDITIONS

Adiabatic, no slip, solid wall boundary conditions are enforced. The method of applying these boundary conditions depends on the turbulence model employed. With the Baldwin-Lomax model the mean flow equations are integrated to the wall with the first grid point off the wall placed in the viscous sublayer to provide sufficient resolution of the extremely steep velocity gradients in the near wall region. The u and v velocity components are set to zero at the wall. The wall temperature is obtained from a zeroth order extrapolation which is equivalent to enforcing a zero normal temperature gradient. The wall pressure is obtained from a normal momentum equation.

Two options are available for applying the wall boundary conditions when the Wilcox-Rubesin model is used. The first is to integrate the governing equations to the wall as is done with the Baldwin-Lomax model. However, a much finer grid spacing is required to resolve the gradients in the turbulence quantities. With the Baldwin-Lomax model a value of y^+ between 1 and 5 at the first grid point off the wall is sufficient. To accurately solve the Wilcox-Rubesin turbulence model equations, this value of y^+ must be reduced by a factor of ten with a value below 0.1 recommended. The mean flow variables u , v , p , and T are obtained as for the

Baldwin-Lomax model. The turbulent kinetic energy is set to zero at the wall. Physically, the specific turbulence dissipation goes to infinity at the wall. However, the following asymptotic value of ω is recommended by Wilcox and Rubesin⁵⁴ for a smooth impervious wall

$$\omega \rightarrow \frac{20\mu_w}{\beta\rho_w y^2} \quad (45)$$

and was found by Viegas and Horstman⁴⁹ to be valid up to $y^+=10$.

Initial computations using Equation (45) and integration to the wall showed that the turbulence model equations were extremely stiff in the near wall region causing numerical problems for even a simple flat plate boundary layer case. Accurate solutions could be obtained but required inordinate amounts of computer time due to the extremely fine grid spacing.

In an effort to avoid these problems, Viegas and Rubesin⁷⁴ developed a wall function boundary condition for use with the Jones-Launder and Wilcox-Rubesin turbulence models that is applicable to adiabatic, no-slip wall conditions. Their results were most promising with the general conclusion that the wall functions improved the agreement of computed results with experiments, especially in the regions of shock wave/boundary layer interactions and also helped avoid the stiffness problems associated with the near wall region. This formulation required that the first grid point off the wall be located in the fully turbulent log region with a y^+ of at least 40. The upper limit on y^+ at the second grid point off the wall was constrained to be less than $\delta^+/7$. Thus, a vast reduction in computer time could be achieved. In a later paper, Viegas, et al.⁷⁵ presented an extended version of the wall function method with improved performance in the calculation of separated flows. The new method was also applicable to non-adiabatic walls and included a formulation for use in the viscous sublayer. The original wall function method was incorporated into the NASCRIN code and was used for a preliminary set of calculations with adiabatic wall conditions. For a flat plate boundary layer case, the wall temperature was found to increase with downstream distance, eventually exceeding the incoming stagnation temperature. The reason for this was not apparent.

Although the wall function method applied in the log layer appeared to be most promising, the problem with the wall temperature was disturbing. For the current applications where detailed experimental measurements through the boundary layer are going to be evaluated and compared to numerical predictions, a finer grid spacing than the log layer wall function method provides is desired. For this reason, the wall function formulation for use in the viscous sublayer⁷⁵ is used in this study. With this formulation, the grid spacing requirements near the wall are the same as with the Baldwin-Lomax model. Hence, the two techniques may be compared on the same grid. The sublayer formulation is also much easier to vectorize than the log layer method while it still offers the advantage of reducing the numerical stiffness problems. The sublayer type wall function approach is outlined below.

At the wall $u = v = q_y = 0$ and the vector \mathbf{N} at the wall becomes

$$\mathbf{N}_w = \begin{bmatrix} 0 \\ -y_\xi p_w + x_\xi (\tau_{xy})_w \\ -y_\xi (\tau_{xy})_w + x_\xi p_w \\ -y_\xi (q_x)_w \end{bmatrix} \quad (46)$$

It is this vector that is needed in Equation (1) to impose the wall boundary conditions. The wall shear stress, $(\tau_{xy})_w$, the wall pressure, p_w , and the wall temperature T_w are required to evaluate this expression. The wall pressure is obtained from the same normal momentum equation used with the Baldwin-Lomax model. In the following development of the wall function relationships, the coordinate system is slightly different than in the mean flow equations. The y direction is perpendicular to the wall and positive away from the wall. The u velocity is the velocity along the wall and the heat flux and shear stress terms are defined by gradients perpendicular to the wall. The first grid point off the surface is denoted by a subscript 2 and the edge of the viscous sublayer is denoted by a subscript v .

The wall temperature is obtained from the reduced energy equation in the viscous sublayer

$$q = q_w + u\tau \quad (47)$$

where q is the heat flux normal to the wall, u is the velocity parallel to the wall and τ is the shear stress aligned with wall. For an adiabatic wall, equation (47) may be written as

$$-\frac{C_p}{Pr_l} \frac{\partial T}{\partial u} = u \quad (48)$$

which is integrated to yield

$$T = T_w - \frac{Pr_l}{C_p} \frac{u^2}{2} \quad (49)$$

This expression is applied at point 2, where $u = u_2$, $T = T_2$ to give the wall temperature, T_w .

The wall shear stress is obtained from the reduced momentum equation in the sublayer,

$$\mu \frac{\partial u}{\partial y} = \tau_w + \frac{dp}{dx} y \quad (50)$$

The viscosity is assumed to vary linearly with temperature, $\mu = \mu_w (T/T_w)$. Using this assumption and the temperature distribution given by Equation (49), Equation (50) is integrated to give an expression for the wall shear stress

$$\tau_w = \frac{u_2 - \frac{Pr_l}{2C_p T_w} \frac{u_2^3}{3} - \frac{y_2^2}{2\mu_w} \frac{dp}{dx}}{y_2/\mu_w} \quad (51)$$

Equations (49) and (51) are used to evaluate the wall shear stress and temperature given values of u , T , and y at point 2 and dp/dx at the wall, the only restriction being that this grid point be located in the viscous sublayer, $y_2 < y_v$. The edge of the viscous sublayer is taken as the location where

$$Re_v = 20 = \frac{y_v \sqrt{\rho_v k_v / \rho_w}}{\mu_w / \rho_w} \quad (52)$$

A parabolic kinetic energy distribution

$$k = k_v \left(\frac{y}{y_v} \right)^2 \quad (53)$$

is assumed in the viscous sublayer. Equations (52) and (53) are combined to give an expression for the location of the viscous edge

$$y_v = (Re_v y_2 \mu_w)^{1/2} \left(\frac{\rho_w}{\rho_2 k_2} \right)^{1/4} \quad (54)$$

Special conditions must also be applied to the turbulence model equations when employing the wall function method. From the kinetic energy distribution, equation (53), one sees that a zero normal gradient in k exists at the wall, i. e.

$$\left. \frac{dk}{dy} \right|_w = 0 \quad (55)$$

This condition is imposed on the normal derivatives of k at the wall which appear in the turbulence model equation for k . The turbulence kinetic energy production and dissipation terms also receive special treatment. The production of turbulence kinetic energy at point 2 is set to zero. The turbulence dissipation is set using Equation (45),

$$\omega_2 = \frac{20\mu_w}{\beta\rho_w y_2^2} \quad (56)$$

and the dissipation term in the kinetic energy equation is then calculated using this value of ω_2 . By specifying ω_2 , the need to solve Equation (34) at point 2 is eliminated.

A brief summary of the wall wall function boundary condition is now given. Equations (49) and (51) are solved for the wall temperature and wall shear stress needed in the vector \mathbf{N}_w . The wall pressure is obtained from a normal momentum equation. The turbulence dissipation is set using Equation (56) and the turbulence kinetic energy is set to zero. Additionally, the condition of zero gradient in the turbulence kinetic energy as stated in Equation (55) is imposed when evaluating the turbulence model equations at point 2. These relations are used at solid wall boundary points and have been found to allow a coarser grid spacing near the wall which helps avoid numerical problems encountered when the turbulence equations are integrated to the wall and allows a larger time step.

D. TEST CALCULATIONS

Several test calculations were performed to validate the computational procedure outlined in the preceding sections. All of the computations reported here were performed on the NCSA CRAY-XMP/48 vector processing supercomputer. This computer is configured such that each of the four available processors act independently, i.e. no parallel processing, and the core memory of this computer was sufficiently large to execute all of the runs in the core memory without having to resort to the use of the Solid State Disk (SSD) device which is available. The SSD is essentially a very large and fast RAM disk device. Three test cases were executed. The first was a Mach 1.48 equilibrium flat plate turbulent boundary layer, the second was a Mach 2.94 equilibrium flat plate turbulent boundary layer, and the third was a Mach 2.94 oblique shock/turbulent boundary layer interaction at a 20 deg. compression corner. The results of these three cases are now considered separately.

1. TEST CASE 1

This test case was performed mainly as a check for the wall function boundary conditions but is also a useful check on the proper performance of the main computational scheme and the Wilcox-Rubesin turbulence model. Computations were made of an adiabatic equilibrium flat plate boundary layer at $M = 1.48$, $T_0 = 283$ K, and $Re_\delta = 5.83 \times 10^5$, $\delta = 25$ mm. These flow conditions correspond to the experimental conditions of Mateer, et al.³³. These experiments were performed in a constant area duct of radius 0.1239 m (4.875 in.). This case was also computed by Viegas and Rubesin⁷⁴ using both integration to the wall and log-layer type wall function boundary conditions. The integration to the wall employed the Wilcox-Rubesin model while the reported results for the wall function calculations employed the Jones-Launder model.

To compute this case the computational grid was set up with a symmetry plane located 0.12m from the flat plate. In the direction normal to the wall, 52 grid points were used. A geometric progression, with a grading ratio of 1.05, was used to stretch the grid near the wall.

The geometric progression was applied to the first 41 points off the wall and a constant grid spacing was used for the remaining points. The spacing between the first point and the wall was $y_2 = 6.0 \times 10^{-4}$ m ($y_2^+ = 170$), resulting in 21 grid points being located in the boundary layer. In the flow direction a constant grid spacing of $\Delta x/\delta = 1.0$ was used. The incoming boundary layer for the calculation was obtained using the Baldwin-Lomax turbulence model to calculate a boundary layer growing from a uniform initial profile. The results from the Baldwin-Lomax calculation were used to start the Wilcox-Rubesin calculation by assuming a uniform turbulence intensity through the boundary layer to give the turbulence kinetic energy, k . The specific dissipation, ω , was obtained using this value of k , the turbulent viscosity and density from the Baldwin-Lomax calculation, and Equation (31) with $\gamma^* = 1.0$. The calculation was then continued using the log-layer wall functions and the Wilcox-Rubesin model. Inaccuracies in the profiles of the turbulence quantities caused by this crude patching together of the two models were found to quickly damp out a few grid locations downstream. The initial value plane was obtained by applying the incoming flow variable profiles to all downstream locations. Extrapolation was used at the outflow boundary and symmetry conditions were imposed at the freestream boundary. The original constants (Equation 38) for the Wilcox-Rubesin model were used with the exception of $\gamma_\infty = 0.90$ being used, as this value of γ_∞ was the one used by Viegas and Rubesin⁷⁴. Numerical damping was not used. The calculation was made in segments by dividing the flow direction into three pieces. The final calculation was made on a 52×51 grid and was run for 12000 iterations requiring 323 cpu seconds giving a computational rate of 1.02×10^{-5} seconds / grid point / time step. This was sufficient physical time to allow a particle in the freestream to traverse the computational domain 5 times.

To evaluate the computed results a comparison to Viegas and Rubesin's⁷⁴ integration to the wall is made in Figures 5 and 6. In Figure 5 the computed u velocity profiles are shown with good agreement between the two computations. A more severe test is shown in Figure 6 where the computed turbulent kinetic energy profiles are compared. Again, good agreement is

seen. These results were most encouraging as they indicate that the current implementation of the Wilcox-Rubesin model with the log-layer wall function boundary conditions could accurately reproduce calculations made with an entirely independent code. However, upon further study of the computed results, the wall temperature was not found to be constant. The wall temperature was seen to increase with downstream distance eventually exceeding the incoming stagnation temperature. This condition is physically unrealistic for this adiabatic wall calculation. Similar calculations employing the Wilcox-Rubesin model and the sublayer wall functions did not display this undesirable trend. The reason for this discrepancy is unknown and because of this only the sublayer type wall functions are employed in the remainder of this work.

2. TEST CASE 2

For the second test case the Mach 2.94 adiabatic flat plate equilibrium boundary layer investigated experimentally by Kuntz⁸⁴ was computed using both the Baldwin-Lomax and Wilcox-Rubesin turbulence models. The velocity measurements of Kuntz⁸⁴ were made using the same two-component, coincident LDV system to be used in this study. These measurements were made on the floor of a 10.2 x 10.2 cm² wind tunnel with the upstream stagnation conditions being $p_0 = 483$ kPa (70 psia) and $T_0 = 303^\circ$ K. The boundary layer thickness was $\delta = 8.2$ mm.

The same computational grid in the y-direction was used for both the Baldwin-Lomax and the Wilcox-Rubesin calculations. Fifty-five grid points were used in the y-direction, normal to the wall. These grid points were distributed into 4 regions. A geometric progression was applied in the first three regions away from the wall. In the first region, closest to the wall, 20 points were used and the grading ratio was 1.15. The location of the first grid point away from the wall was at $y_2 = 1.0 \times 10^{-5}$ ($y_2^+ \approx 2.5$). In the next region, 20 more points were used with a grading ratio of 1.05. In the third region, 10 points were used with a grading ratio of 1.30. Equal grid spacing was used for the remaining points in the fourth region. The

freestream boundary was located 0.1 m from the wall. The initial boundary layer profiles and initial time planes were obtained using the same procedure described above for the Mach 1.48 boundary layer calculation and, as before, the calculation was performed in segments.

For the final Baldwin-Lomax calculation, 41 grid points were used in the flow direction with a constant spacing of 0.015 m with $\Delta x/\delta = 1.8$ at the location of interest. Visbal and Knight's⁶⁸ recommended value of $C_{cp} = 2.08$ was used; otherwise the original model constants in Equation (30) were used. No slip boundary conditions were applied at the wall, symmetry boundary conditions were applied at the freestream boundary, one point extrapolation was used at the exit, and all incoming flow variables were held fixed. The explicit-implicit option available in the NASCRIN code was used with a Courant number of 3. No damping was used. Special care was taken to ensure that the absolute maximum outer peak in the function $F(y)$ was selected. Several local peaks in this function were observed. The solution was run for 30,000 iterations requiring 499 cpu seconds giving a computational rate of 7.4×10^{-6} seconds / grid point / time step. A particle in the freestream would have had sufficient time pass through the computational domain 1.4 times. Thus, this solution may not be totally converged.

The final Wilcox-Rubesin computation was performed on a grid with 21 points in the flow direction and an equal spacing of 0.015 m giving $\Delta x/\delta = 1.8$ at the location of interest. The patching between the Baldwin-Lomax and the Wilcox-Rubesin calculations was performed at a location 0.75 m upstream of the initial column on the final grid. Sublayer type wall functions were used at the solid wall, otherwise the boundary conditions were the same as in the Baldwin-Lomax calculation. A Courant number of 0.95 was used with the totally explicit MacCormack scheme and the model constants used were those given in Equation (38) with the exception of γ_∞ . The solution was run for 45,000 iterations using $\gamma_\infty = 9/10$, giving the first solution. The solution was then advanced for 20,000 more iterations with $\gamma_\infty = 10/9$, giving the second solution. After the total of 65,000 iterations a particle in the freestream would have

had sufficient time to pass 4.25 times through the computational domain. The computational rate was 1.39×10^{-5} sec / grid point / time step.

A comparison with the experimental data will now be made for these three computations. The computed values of the wall shear stress for the Baldwin-Lomax, $\gamma_{\infty} = 9/10$ Wilcox-Rubesin, and $\gamma_{\infty} = 10/9$ Wilcox-Rubesin calculations are 120, 113 and 99 N/m², respectively. These correspond to friction velocities of $u_{\tau} = 25, 24.2$, and 22.7 m/s. The experimental value of the friction velocity was obtained from the velocity measurements using a wall-wake profile curve fit to the data yielding a value of $u_{\tau} = 24.6$ m/s. Thus, all three computations give reasonable values for the wall shear stress with the $\gamma_{\infty} = 10/9$ Wilcox-Rubesin calculation underpredicting the wall shear stress somewhat. This trend is in agreement with the results of Viegas and Horstman⁴⁹. Streamwise velocity profiles for the three computations are compared to the experimental results in Figure 7. All three computations do a fair job of predicting the velocity profile. The Baldwin-Lomax calculation tends to overpredict the velocity over the entire boundary layer. Both Wilcox-Rubesin calculations give better predictions near the boundary layer edge but also overpredict the velocity closer to the wall. The turbulence kinetic energy profiles for the two Wilcox-Rubesin calculations are compared to the data in Figure 8. Both calculations overpredict the turbulence kinetic energy within the boundary layer with the $\gamma_{\infty} = 10/9$ solution giving closer agreement to the data. In the freestream, both calculations give zero turbulence kinetic energy while the experimental results indicate a freestream turbulence intensity is present. Part of this freestream turbulence may be attributed to the limited resolution of the counter clocks used for the LDV measurements. In a high speed flow, this clock resolution problem leads to an overprediction of the freestream turbulence intensity. The shape of the two computed profiles are very similar displaying a peak in the turbulence kinetic energy very close to the wall and a second peak in the middle of the boundary layer. This second peak is also seen to occur in the experimental results. Measurements were not made close enough to the wall to reveal the inner peak in the turbulence kinetic energy. The turbulence kinetic energy is a very sensitive variable and the differences

between the computed and experimental results are not considered to be excessive. However, the overprediction of the turbulence kinetic energy could help explain the slightly fuller computed mean velocity profiles.

3. TEST CASE 3

For the third test case a separated oblique shock/turbulent boundary layer interaction was selected. The experimental measurements of Kuntz⁸⁴ for a Mach 2.94 oblique shock/turbulent boundary layer interaction at a 20° compression corner are compared to computed results. Calculations employing the Baldwin-Lomax model have been completed and calculations with the Wilcox-Rubesin model are currently being performed. A description of the Baldwin-Lomax calculation follows. The grid in the y-direction is the same as that used above for the Mach 2.94 equilibrium boundary layer computation. Results from the calculation above were also used to specify the incoming flow variables. The boundary conditions and turbulence model constants are the same as above but now the totally explicit MacCormack scheme is used with a Courant number of 0.95. The computational domain extended from $x = 0$ to $x = 0.0825$ m with the 20° ramp beginning at $x = 0.040$ mm. Two grids were employed, varying only in the streamwise grid spacing. For the first grid, 34 points were used with a constant spacing of $\Delta x = 2.5$ mm, $\Delta x/\delta_0 = 0.3$. For the second grid 45 points were used with the grid spacing varying from $\Delta x/\delta_0 = 0.49$ upstream of the separation point, to $\Delta x/\delta_0 = 0.12$ in the separation region, to $\Delta x/\delta_0 = 0.31$ downstream of reattachment. The first calculation, (a), employed the 34 point grid and was run for 30,000 iterations using a damping coefficient of 0.05. This calculation was extended for 30,000 more iterations using a damping coefficient of 0.20 to give the second calculation, (b). The third calculation, (c), was performed on the refined grid using a damping coefficient of 0.20 and was run for 16,000 iterations. For computations (a) and (b) sufficient physical time was allowed for a particle in the freestream to pass through the domain 5 times while in (c) a particle had time to pass approximately 2.5 times through the domain. However, in (c) the separation location was not

found to change significantly for 1000 iterations. In all three cases the computational rate was approximately 7.8×10^{-6} sec / grid point / time step.

Results for these three calculations are shown in Figure 8 where the wall static pressure non-dimensionalized by the freestream static pressure has been plotted with the downstream distance shifted such that the corner occurs at an abscissa value of zero. All three calculations predicted a small separation region at the corner but greatly underpredicted the upstream extent of the separation. This result is typical of the Baldwin-Lomax model.⁶⁸ Oscillations in the pressure are seen in case (a) indicating the need for increased numerical damping. Cases (b) and (c) are nearly identical indicating that grid independence has been achieved, at least in the flow direction. The effects of the grid spacing normal to the wall need to be investigated further. LDV measurements of the velocity field are also available for this configuration but have not yet been compared to the computations. As was mentioned above, calculations with the Wilcox-Rubesin model are currently being made for this test case and are expected to give much improved results.

IV. EXPERIMENTAL SETUP

The experimental facilities and procedures used during this investigation are described in this chapter. In part A attention is focused on the air flow facility and small scale wind tunnel/test section used. The preliminary experiments performed to check the operating characteristics of the wind tunnel are also described. In part B details of the procedures and equipment used to perform the Schlieren, surface flow visualization, and the wall static pressure measurements are given. Finally, in part C the laser Doppler velocimeter (LDV) system is discussed. This system will be used in the remainder of this study to investigate the Mach 1.6 shock wave/turbulent boundary layer interaction. LDV operating procedures and data reduction and analysis considerations are given.

A. EXPERIMENTAL AIR FLOW FACILITY AND TEST SECTION

The experimental portion of this study was performed in the Gas Dynamics Laboratory of the Department of Mechanical and Industrial Engineering. This high pressure air flow facility consists of two compressors which supply air to a storage tank farm with an approximate volume of 140 m^3 . The first compressor, built by Ingersoll-Rand, delivers 41 kg/min at 960 kPa (1200 SCFM at 125 psig), and the second, a Gardner-Denver compressor, supplies 20 kg/min at 760 kPa (600 SCFM at 95 psig). Thus, at pressures below 760 kPa , a continuous flowrate of 61 kg/min is possible. A six inch supply line connects the tank farm to a large axisymmetric plenum chamber with a flat circular faceplate designed to allow the connection of either axisymmetric or planar measurement sections. Flow leaving the attached measurement section is vented outside through a large silencing duct. A Fisher model EK-667, 4 inch control valve equipped with a 40% capacity cage is located in the supply line. The control valve, in conjunction with a Fisher type TL101 electronic controller, was used to regulate the plenum pressure which could be automatically held constant to within $\pm 0.69 \text{ kPa}$

(± 0.1 psi) as the tank farm pressure varied. A Wallace & Tiernan model 61A-1A-0200 precision absolute pressure gage was used to monitor the plenum chamber pressure.

A small scale, planar two-dimensional supersonic wind tunnel was fabricated out of aluminum for use in this investigation. The wind tunnel consists of a constant area stagnation chamber followed by a symmetric supersonic nozzle feeding directly into the test section. A symmetric nozzle is used such that the upper and lower wall boundary layers entering the test section have identical properties. A variable area diffuser is located at the exit of the test section which can be adjusted to yield either a diverging or converging-diverging geometry. The wind tunnel has a constant width of 7.62 cm (3.0 in.) over the entire length. The entrance to the stagnation chamber is mounted directly to the faceplate of the large plenum chamber and the diffuser exit is connected to the silencing duct venting outside. Two interchangeable nozzle blocks were designed and built, one for Mach 2.45 and the other for Mach 1.60. The supersonic nozzles were designed using the nozzle design program of Carroll, et al.⁷⁶ which employs an inviscid method of characteristics analysis to design supersonic nozzles with uniform exit flow. Optical access to the test section is provided by removable windows in the wind tunnel side walls. The 40.64 cm (16 in.) long by 5.08 cm (2 in.) high, 1.27 cm (0.5 in.) thick soda lime glass is mounted in a symmetric frame which can be rotated to view either the forward or rear portion of the test section with a 7.62 cm (3 in.) overlap in the viewing areas. The surfaces of the glass were not polished nor was any flatness specification imposed. Samples of optical glass with a high degree of flatness and parallelity displayed only slightly better optical quality than the unpolished soda lime glass when viewed through the Schlieren system. For this reason, the considerably cheaper unpolished soda lime glass was selected. As a side note, heat treated Pyrex glass was found to have a high level of internal stress which appeared as striations when viewed with the Schlieren, even when the surface was highly polished to a strict flatness tolerance. A photograph of the wind tunnel is shown in Figure 10. The faceplate of the large axisymmetric stagnation chamber is visible to the left and the

silencing duct is on the right. The near window has been removed to reveal the Mach 1.6 test section. The far window frame is mounted with the glass in the forward position.

A description of the wind tunnel configuration with the Mach 2.45 nozzle is given first. A photograph of the Mach 2.45 nozzle blocks is shown in Figure 11. The upper and lower stagnation chamber, nozzle, and test section walls were each fabricated from a single piece of aluminum to avoid seams between sections. The stagnation chamber had a constant height of 10.16 cm (4.0 in.). The nozzle throat, located 33.528 cm (13.2 in.) from the entrance, had a height of 1.448 cm (0.57 in.). The nozzle exit height was 3.81 cm (1.5 in.) with the distance from the throat to the nozzle exit being 8.179 cm (3.22 in.). This nozzle was designed for a Mach number of 2.50 but due to boundary layer growth on the nozzle walls yielded a Mach number of 2.45 based on wall static pressure measurements. Following the recommendations of Bradshaw⁷⁷ and Baines and Peterson⁷⁸, two removable screens each with 57.4% open area (44x44 mesh stainless steel wire cloth, 0.0055 in. wire diameter), were located in the rectangular stagnation chamber, 16.36 cm (6.44 in.) and 20.19 cm (7.95 in.) from the entrance, to help provide uniform mean and fluctuating velocity profiles. The screens are mounted in aluminum frames which are slid into the slots visible in the stagnation chamber portion of the nozzle blocks of Figure 11. Originally, the Mach 2.45 test section was made with a constant height of 3.81 cm (1.5 in.). However, initial Schlieren visualizations with this nozzle block revealed undesirable oscillatory movement of the shock train location on the order of a boundary layer thickness in amplitude. The frequency of this shock motion was not determined. In an effort to eliminate this shock motion, the test section walls were modified such that the upper and lower walls could be diverged by a variable angle of up to 1.25 degrees each with the divergence beginning at the nozzle exit. The variable area exit diffuser was also used to isolate the test section from downstream fluctuations by forming a nearly sonic second throat. A series of Schlieren visualizations with various test section divergence angles and diffuser geometries showed that the shock train unsteadiness was not visibly affected by the divergence angle. However, the second throat diffuser did tend to make the mean shock

location insensitive to relatively large variations in the plenum pressure of the order of 34.5 to 69.1 kPa (5 to 10 psia). For the results presented in this report, the test section divergence angle was held fixed at 0.25 degrees for both the top and bottom walls to give a zero pressure gradient in the fully started test section. Static pressure taps were located along the centerline of the upper and lower test section walls. On the upper wall, 40 taps were installed, the first tap being at a location 0.0762 cm (0.03 in.) from the nozzle exit. A spacing between taps of 1.27 cm (0.5 in.) was used from 0.0762 cm (0.03 in.) to 38.18 cm (15.03 in.) downstream of the nozzle exit, a spacing of 2.54 cm (1.0 in.) was used from 38.18 cm (15.03 in.) to 53.42 cm (21.03 in.) downstream, and a spacing of 5.08 cm (2.0 in.) was used from 53.42 cm (21.03 in.) to 68.66 cm (27.03 in.) downstream. On the lower test section wall, 14 taps, spaced 5.08 cm (2.0 in.) apart, were installed with the first tap located 2.62 cm (1.03 in.) downstream of the nozzle exit. The pressure tap diameter on the inside surface of the test section was 0.0635 cm (0.025 in.) I. D. On the outside of the test section a 0.16 cm (0.063 in.) O. D. stainless steel tubulation was mounted to each tap opening. Vinyl tubing was then used to connect the tubulation to the pressure measuring device. Vacuum grease was used to seal all mating components of the wind tunnel. Initially, soapy water applied to the joints of the tunnel revealed that leaks were present around the wind tunnel window frames. Surface flow results also showed the presence of these leaks. Additional mounting studs were added to rigidly hold the window in place and linear o-ring material was mounted in the side of the nozzle blocks. These steps corrected the leakage problem.

The Mach 1.6 nozzle was designed for a Mach number of 1.615 to allow for boundary layer growth on the nozzle walls. Based on pressure measurements, the nozzle exit Mach number is very close to 1.60. This nozzle has a throat height of 2.54 cm (1.0 in.) and an exit height of 3.206 cm (1.262 in.) with a length of 4.628 cm (1.822 in.) from the throat to the nozzle exit. The throat is located 37.34 cm (14.7 in) from the entrance. The stagnation chamber has the same height as for the Mach 2.45 nozzle and the two flow screens are again located at the same distance from the entrance. With the Mach 1.6 nozzle, additional flow

straightening in the stagnation chamber was provided through honeycomb installed 3.81 cm (1.5 in) from the entrance. The honeycomb had a cell size of 0.635 cm (0.25 in.) and a cell length of 6.35 cm (2.5 in.) with the web material being 0.127 mm (0.005 in.) thick stainless steel. The test section extends from the nozzle exit to 75.38 cm (29.67 in) downstream. The boundary layer growth in the Mach 1.6 test section was predicted using the boundary layer code of Dutton and Addy.⁷⁹ Based on these results, a fixed divergence angle of 0.13 degrees was used for both the upper and lower test section walls in an effort to provide a zero pressure gradient in the fully started test section. Similar boundary layer calculations with the Mach 2.45 test section showed that this method accurately predicted the boundary layer growth for that case. As will be shown in the results section, a small pressure gradient resulted in the Mach 1.6 test section in spite of these efforts. Pressure taps were located only along the centerline of the upper test section wall for the Mach 1.6 nozzle. The first tap was located at the nozzle exit. The second tap was located 2.350 cm (0.925 in.) downstream of the nozzle exit. From 2.350 cm (0.925 in.) to 9.970 cm (3.925 in.) the tap spacing was 2.54 cm (1.0 in.). From 9.970 cm (3.925 in.) to 56.960 cm (22.425 in.) downstream the tap spacing was 1.27 cm (0.5 in.). From 56.960 cm (22.425 in.) to 72.20 cm (28.425 in.) downstream, the tap spacing was 2.54 cm (1.0 in.). As for the Mach 2.45 nozzle, the inside test section pressure tap diameter is 0.0635 cm (0.025 in.) I. D. Connection to each tap is provided on the outside of the test section by 0.16 cm (0.063 in.) O. D. stainless steel tubulations. Vacuum grease was used to seal all mating parts of the wind tunnel. Soapy water applied to the joints while the tunnel was running did not reveal any leaks, with surface flow results confirming this finding.

With both nozzle blocks the particles for the LDV measurements may be injected into the large axisymmetric plenum chamber or along the vertical centerline of the rectangular stagnation chamber. The vertical particle seeder consists of a 0.476 cm (3/16 in.) O.D. tube (#7 hypodermic tubing) which spans the 10.16 cm height of the stagnation chamber and is located before the two screens, and after the honeycomb for the Mach 1.6 nozzle. Nine

aligned, evenly spaced 0.132 cm (0.052 in.) diameter holes are drilled in the wall of the seeder tube. The seeder tube may be rotated to point the nine holes at any desired angle to the mean flow. Seeding only the vertical centerline of the stagnation chamber should help prevent accumulation of seed particles on the windows. Complete information on the type of seed particles used and the particle generator is given in the section on LDV procedures.

B. SCHLIEREN, SURFACE FLOW, AND PRESSURE MEASURING PROCEDURES

Schlieren photography was used to investigate qualitative features of the shock train phenomenon. A standard Toepler Schlieren arrangement was used. The light source was a Xenon model 457 1.4 μ s duration light source which could be operated in either a single spark mode or in a stroboscopic mode for continuous viewing. Either 12 inch or 8 inch diameter parabolic mirrors were used to collimate the light. A box camera using Polaroid Type 55 Positive/Negative 4x5 sheet film (ASA 50) was used with the 12 inch mirror set. Both the box camera and a 35 mm camera mount were available for the 8 inch mirror set. A Nikon F2 camera body with Kodak Pan-X film (ASA 32) was used with the 35 mm mount. The 12 inch mirrors were used for the Mach 2.45 case to give the maximum viewing area. For the Mach 1.6 case, the interaction was shorter and the 8 inch mirrors with the more convenient 35 mm mount were used.

Surface flow visualization was used to give information concerning the separation and reattachment locations and the two-dimensionality of the flow. A mixture of 600 weight gear oil and lampblack was used. This mixture was either spread evenly over the test section surface or placed in discrete dots on the surface. The tunnel was then run for a sufficient amount of time to allow the surface streak pattern to set up. After shutting down the tunnel, a sheet of tissue paper was carefully laid on the surface to absorb the resulting pattern. A photocopy of the tissue paper was then made to obtain a permanent record. While the tunnel was running, notes concerning the direction of the oil flow on the surface were taken. Appropriate arrows were latter superimposed on the pattern to show these directions. The oil

pattern was also observed during the tunnel shutdown process to ensure that this transient did not significantly disturb the pattern.

Measurements of the wall static pressure were made with two Pressure Systems Incorporated (PSI) model DP 6400T digital pressure transmitters. One of these transmitters is visible below the tunnel in Figure 10. With this system a separate transducer is connected to each pressure port. The ports are scanned electronically and an onboard microprocessor reduces the data, giving gage pressure, and transfers it to a host computer. The first DP 6400T has sixteen ± 15 psig and sixteen ± 30 psig transducers, the second DP 6400T has sixteen ± 45 psig and sixteen ± 100 psig transducers. These transducers were calibrated with a primary standard and the slope of each calibration curve was stored in the transmitter memory. A zero point calibration was performed before each scan to account for varying atmospheric pressure. The estimated accuracy of the two lower range transducers was ± 0.0069 kPa (± 0.01 psi) and the accuracy of the two higher range transducers was ± 0.0172 kPa (± 0.025 psi). The two pressure transmitters were connected to a HP 9000 host computer through a manual switching box such that a scan with the first transmitter could be immediately followed by a scan with the second transmitter. A scan of 32 ports took approximately 5 seconds. A complete scan using both transmitters took a total time of between 10 to 15 seconds. All data analysis and plotting was done on the HP 9000.

C. LDV PROCEDURES

The laser Doppler Velocimeter (LDV) technique was selected as the method to be used in making the mean and fluctuating velocity measurements. Johnson and Rose⁸⁰ and Ardonneau⁸¹ have shown that both LDV and hot wire measurements have limitations in transonic flows. Hot wire measurements exhibit large variations in the mass flux sensitivity in the range of Mach numbers $0.8 < M < 1.4$. This effect is caused by detached shock waves from the hot wire supports interacting with the hot wire. Thus, large uncertainties in hot wire measurements occur at the Mach numbers present in the shock train. Additionally, the physical

presence of the hot wire probe in sensitive transonic and separated flows may noticeably disrupt the flow. The LDV is seen as an effective tool in the study of separated shock wave/boundary layer interactions provided the effects of particle lag, velocity bias, and fringe bias can be accounted for. The nonintrusive nature of the LDV and the unambiguous detection of reversed flow are two strong motivations for using the LDV technique in sensitive shock separated flows.

Since LDV is a relatively new and complicated technique, it will be described in some detail. The LDV system to be used in this study is essentially the same system used by Petrie⁸², Samimy⁸³, and Kuntz⁸⁴. The system consists of a Spectra Physics model 165 argon-ion 5 watt laser, TSI optics and electronics, a three-dimensional traversing mechanism, and a PDP 11/73 minicomputer. The experience of these previous researchers has contributed to a valuable body of knowledge in applying the LDV to high speed flows. A description of the current LDV operating procedures follows.

Dual-beam, two-component, coincident velocity measurements are made using two laser beams of 488 nm (blue) and 514.4 nm (green). Appropriate optics are used to generate a measurements volume consisting of two sets of orthogonal fringes rotated at approximately ± 45 deg. to the mean flow direction. The available optical arrangements are listed in Tables 3, 4, and 5. Beam expansion is available for beam spacings of 22 and 13 mm prior to the expander. The configuration selected for this study is a 13 mm beam spacing with beam expansion and a 350 mm transmitting lens. This configuration gives the advantages of a small measurement volume diameter and a relatively large beam spacing. Frequency shifting at 40 MHz will be used to detect reverse flow. Particles travelling at shallow angles to the fringes may not cross the required number of fringes for a valid measurement causing a bias toward measuring the velocities of particles travelling more nearly perpendicular to the fringes. This bias is commonly called fringe bias. The fringe bias effects were investigated using the analysis of Samimy⁸³. This type of bias can be especially severe when making two-component, coincident measurements since the probability of a valid coincident measurement is

equal to the product of the probabilities of valid measurements in each channel. The combination of frequency shifting, large fringe spacing (and correspondingly higher fringe velocity), ± 45 deg. fringe orientation, and the requirement of 4 fringe crossings for a valid measurement has the desirable effect of virtually eliminating fringe bias. The receiving optics are used in the forward scatter mode at 10 degrees off axis. Off axis collection reduces the effective length of the measurement volume and helps avoid problems with flare and stray laser light. A pinhole aperture and optical color filter in front of each photodetector also helps eliminate stray light, thereby increasing the signal-to-noise ratio of the system. Beam expansion also improves this ratio.

Two TSI model 1990B frequency counters, operating in the single measurement per burst mode, are used to process the signal from the photodetectors. The signal is high- and low-pass filtered to eliminate the pedestal and noise, respectively, from the signal. A comparison between the time for 2 and 4 cycles of the PMT signal is used to validate the signal, and a master interface is used to check for coincidence between the two counter outputs. This coincidence window is imposed to ensure that the measurement is made from the same particle in each channel. Digital output from the counters is transferred directly to the PDP 11/73 and saved on hard disk. Data reduction can be performed on the PDP 11/73 or the raw data can be transferred to a Hewlett-Packard 9000 series minicomputer for data reduction and graphical output. The frequency counters are capable of sampling at a speed much higher than the data rate. Hence, the data is not sampled at equal time intervals. Rather, each data sample which meets the coincidence requirement is collected, regardless of the time between samples. As a consequence, the resulting data is completely velocity biased and a two-dimensional velocity magnitude bias correction⁸⁵, similar to that of McLaughlin and Tiederman⁸⁶, is employed to correct the data. A TSI six jet atomizer is used to generate seed particles. Using this atomizer, Petrie⁸² produced approximately 1 micron diameter particles when 50 cp viscosity silicon oil is used.

V. EXPERIMENTAL RESULTS

The results of the integrated numerical and experimental investigation of multiple shock wave/turbulent boundary layer interactions in confined rectangular ducts are presented in this section. Two incoming, undisturbed Mach numbers were considered, Mach 1.6 and 2.45. For both the Mach 1.6 and 2.45 interactions, spark Schlieren flow visualization, surface oil flow visualization, and wall static pressure measurements were made. LDV measurements of a Mach 1.6 interaction are currently being made. The Mach 2.45 interaction was unsuitable for LDV measurements with the available equipment due to shock train unsteadiness. Numerical computations of the Mach 1.6 interaction are also being performed. The experimental results are discussed in the following sections and, when appropriate, the corresponding numerical results are also presented.

A. MACH 2.45 RESULTS

The experimental results for the Mach 2.45 shock train interaction are discussed in this section. The preliminary experiments with the Mach 2.45 test section have been previously described in Chapter 4. For the results given here a constant test section divergence angle of 0.25° was set on the upper and lower walls giving a total divergence angle of 0.50° . This was done to provide a neutral pressure gradient in the undisturbed boundary layer. Three cases are considered, corresponding to three shock locations in the test section. The experimental operating conditions are summarized in Table 6. For all three cases the wind tunnel was operated at a nominal stagnation pressure of 311 kPa (45 psia) measured in the large plenum chamber. The adjustable diffuser was configured as a converging-diverging diffuser. By adjusting the size of the second throat, the shock train was positioned at the three desired locations. This series of experiments is useful in investigating the effects of flow confinement, as described by the ratio δ_u/h , with the Mach number and unit Reynolds number held constant. The Reynolds number based on δ_u will change slightly as δ_u changes. For these preliminary

results, the undisturbed boundary layer thickness, δ_u , defined as the boundary layer thickness at the start of the pressure rise, was estimated from the Schlieren photographs.

1. MACH 2.45 FLOW VISUALIZATIONS

The Schlieren and surface flow results for the Mach 2.45 interaction are given in Figures 12, 13, and 14. In Figures 12 and 13 the top and bottom portions of the figures are the oil surface flow patterns of the top and bottom test section walls, respectively. Between these is shown the Schlieren, to scale with the surface flow, viewed through the window in the tunnel side wall. As discussed below, the surface flow for the third case could not be performed due to flow unsteadiness. Therefore, only the side view Schlieren is given in Figure 14. In Figures 13 and 14, the Schlieren picture shown consists of two photographs joined together. The entire shock train could not be photographed at once due to the limited field of view of the Schlieren apparatus. In all three figures the Schlieren was set up with a vertical knife edge such that accelerations show as light regions and decelerations as dark regions. The flow is from left to right in all cases.

A few cautionary words should be made concerning the interpretation of these flow visualizations. The Schlieren and surface flow results are useful in studying the qualitative features of the flow. However, care must be taken to not draw excessively quantitative conclusions from these results. In particular, caution must be taken in judging the velocity magnitudes through the interaction based solely on the Schlieren photographs. Also, the surface flow results give a good indication of the flow directions at the surface, but should not be used to evaluate the flow too far away from the surface.

Consider first the case with a confinement level of $\delta_u/h = 0.15$, Figure 12. In the Schlieren photograph, weak Mach waves can be seen in the incoming flow. These were generated by the growing boundary layer in the nozzle and by any slight imperfections in the nozzle contour. The first shock in the shock train is an asymmetric oblique shock pattern. The top leading oblique shock originates in the upper wall boundary layer upstream of the location

where the bottom leading oblique shock intersects the lower wall boundary layer. The two leading shocks cross below the centerline. After crossing, the two shocks terminate a fair distance from the nozzle wall indicating a substantial subsonic region near the wall. Following the first oblique shock pattern, the light region indicates that the flow reaccelerates. It is not possible to determine if the flow in this core region is totally supersonic or if the reacceleration occurs from subsonic initial velocities. The second and later shocks are not as well defined but appear to be nearly normal in character near the lower wall and tend to 'lie' along the lower wall without extending all the way to the upper wall. In the shock pattern shown, the shock train is described as being 'attached' to the lower wall even though boundary layer separation is present, as discussed below. This pattern was neutrally stable, with the shock system sometimes being attached to the lower wall and sometimes attached to the upper wall. Occasionally, the shock system would flip from one wall to the other during the course of a run. A large amplification of the size of the turbulence structure is observed going through the interaction and the boundary layer is seen to thicken substantially through the interaction.

Turning attention to the surface flow pattern for this case, one observes two highly different patterns on the top and bottom walls. This is not surprising in light of the asymmetric shock pattern described above. On the top wall a fairly straight separation line occurs slightly upstream of the separation on the bottom wall. Following the separation on the top wall is a large three-dimensional reverse flow region. The flow reattaches near the center of the tunnel at two 'star' patterns on either side of the centerline. After these star patterns the flow is seen to head downstream, with some of the flow closer to the side walls turning and heading back upstream. The flow reattaches near the side walls further downstream. This type of reattachment could be described as a U-shaped reattachment with the open part of the U facing downstream. Substantial corner effects are seen on the upper wall with the flow near the corners heading away from the side walls. Following complete reattachment, the flow is again fairly two-dimensional. On the bottom wall the separation line is again nearly straight. The separation region is much smaller and the reattachment line is only slightly curved. Again

corner effects are seen but are not large until after reattachment on the bottom wall where the corner vortex appears to grow at a faster rate on the bottom wall with only the middle third of the flow being two-dimensional at the downstream edge of the picture. In a study of supersonic flow through a square duct without shocks, Davis, et al.⁸⁷ observed a pair of counter rotating secondary flow cells centered about the corner bisector. Such a phenomenon could explain the corner effect observed here.

Moving to the second case with $\delta_u/h = 0.26$ (Figure 13), the results are similar to those with $\delta_u/h = 0.15$. However, the shock system now tends to flip-flop, from top wall attachment to bottom wall attachment, or vice versa, more often. The case of bottom wall shock train attachment is shown. In the Schlieren picture a small amount of oil can be seen on the window, appearing as small streaks on the glass. The Schlieren picture is very similar to the $\delta_u/h = 0.15$ case of Figure 12 with the asymmetric oblique initial shock, followed by a series of shocks that are more normal in character. The overall length of the interaction has not noticeably increased. The top wall surface flow again shows a nearly straight separation line with a U shaped reattachment. However, the flow now reattaches closer to the separation line. The reattachment near the side wall is clearer in this picture, showing a fan shaped pattern at the wall. The region near the side wall appears to be strongly influenced by the side wall and corner effects. Thus, this fan shaped reattachment near the side wall may be caused by secondary flow cells in the corners. The flow following reattachment is again fairly two-dimensional on the top wall with the corner effects being small. On the bottom wall the separation line is nearly straight with reattachment occurring earlier than on the top wall and being more two-dimensional. The second shock is seen to cause a necking in of the corner flow and an accumulation of oil under the shock. The third shock causes a similar but weaker effect. The washed out region between the first and second shocks on the bottom wall is presumed to be caused by the reacceleration of the flow following the first shock. Efforts to improve the recorded pattern by placing additional oil in this washed out area and rerunning the test were unsuccessful. The oil quickly left this region before the other features of the surface

flow could set up. Again a large increase in the corner effect is seen on the bottom wall following the interaction.

At $\delta_0/h = 0.35$ the shock train would not stay attached to a single wall long enough for the surface flow pattern to stabilize. Therefore, only the Schlieren visualization was obtained and is shown in Figure 14. The flow pattern is more symmetric now, with both the first and second shocks being oblique shocks. The later shocks still tend to attach to either the upper or lower wall in a neutrally stable manner. The length of the interaction is about the same as in the two previous cases.

In all three cases, substantial flow unsteadiness was present. This phenomenon was only studied visually with the stroboscopic Schlieren. Two main types of unsteadiness were observed. First is the neutrally stable shock pattern's tendency to flip from one wall to the other at random times. This phenomenon was more pronounced with the shock near the end of the duct. This could be due to the increased level of flow confinement or to a change in the characteristics of the subsonic flow between the shock train and the converging-diverging diffuser. The second type of unsteadiness was in the form of higher frequency shock motion in the flow direction. The magnitude of this motion was on the order of an undisturbed boundary layer thickness. Ikui²⁹ postulated that this type of motion was caused by the resonance of the subsonic flow following the shock. The diffuser is believed to have isolated the shock from the downstream silencing duct, such that any resonance would be due to either a transverse or longitudinal type of resonance in the test section.

2. MACH 2.45 PRESSURE MEASUREMENTS

Wall static pressure measurements were made for the three Mach 2.45 cases summarized in Table 6, with the results presented in Figures 15, 16, 17, and 18. Figures 15-17 present results for pressure measurements made on the top wall only with the shock attached to the bottom wall. In all these figures, the wall static pressure, p , has been normalized by the stagnation pressure before the interaction, p_0 . The ideal value of p/p_0

following a normal shock at Mach 2.45 is 0.4324. The maximum measured value of p/p_0 after the shock train interaction is 0.3742, 0.3496, and 0.3175 for $\delta_u/h = 0.15$, 0.26, and 0.35, respectively. Thus, the pressure recovery through the shock train ranges from 86.5% to 73.4% of the ideal normal shock value. This last value of 73.4% may be slightly low as the pressure recovery may not have been completed before the exit of the duct in this case. This is seen in Figure 15 where the abscissa is the actual downstream distance from the nozzle exit; in the $\delta_u/h = 0.35$ case the pressure is still rising at the duct exit. The zero pressure gradient in the incoming boundary layer is evident. A comparison of the traces shows that the initial pressure rise is very similar for all three cases, with the steep initial pressure rise followed by a pressure plateau. This similarity is seen more clearly in Figure 16, where the pressure traces have been shifted such that the downstream distance is measured from the start of the interaction. This agrees with the findings of Waltrup and Billig³² in their investigation of shock trains in circular ducts. This result is also consistent with the flow visualizations. As was noted in the Schlieren results, the structure of the shock system, which causes the pressure rise, does not change appreciably as δ_u/h increases. The top wall surface flow is seen to change to some extent but would not be expected to have a great effect on the wall pressure. As will be shown later, the Mach 1.6 wall pressure data collapsed well when the downstream distance is measured from the start of the interaction and is normalized by the undisturbed boundary layer thickness at the start of the interaction, δ_u . The Mach 2.45 results have been plotted in such a manner in Figure 17 but fail to collapse to a single curve. In Figure 18 the top and bottom wall pressure distributions for the $\delta_u/h = 0.26$ case are shown. In this case the shock system is attached to the bottom wall. (The bottom wall measurement was actually obtained using the pressure taps on the top wall but with the shock attached to the top wall. This was done to take advantage of the finer pressure tap spacing on the top wall.) The smooth pressure distribution occurs on the top wall where the larger separation region is present. The jagged pressure trace on the bottom wall was caused by the normal shocks lying very close to the surface. The initial pressure rise starts on the top wall first since the upper oblique shock

slightly leads the bottom oblique shock. The top and bottom wall pressure traces eventually coincide near the end of the interaction. Differences between the two profiles occur only in the middle of the shock train where normal shocks lie along one wall.

B. MACH 1.6 RESULTS

Six cases are considered for the Mach 1.6 interaction. A summary of these cases is given in Table 7. The stagnation pressure was held at a nominal value of 20.7 kPa (30 psia) for this set of experiments and the shock location was varied by adjusting the throat gap on the adjustable diffuser, configured as a symmetric converging-diverging second throat diffuser. The test section was built with a constant divergence angle of 0.13° on each side, yielding a 0.26° total divergence angle. This divergence angle was expected to provide a neutral pressure gradient in the undisturbed boundary layer but a small adverse pressure gradient is present. Therefore, the Mach number is approximately constant in this series of experiments, the unit Reynolds number is held constant, and the flow confinement parameter, δ_u/h , is varied. The undisturbed boundary layer thickness, δ_u , was estimated from Schlieren photographs with a horizontal knife edge. An exact value of δ_u will be determined from the LDV measurements once these results are available. In the following section, the Schlieren results are discussed first. Surface flow visualization for each case was so similar that only the surface flow results for $\delta_u/h = 0.34$ are presented. The wall static pressure measurements are then described.

1. MACH 1.6 FLOW VISUALIZATIONS

The Schlieren results are presented in Figures 19 and 20 with the flow from left to right and the knife edge vertical with decelerations showing as dark areas and accelerations as light regions. In Figure 19 the Schlieren was adjusted to a lower sensitivity to view the shape of the shock waves in the center of the duct without interference from the side wall shock wave/boundary layer interaction. The top picture shows the shock positioned near the nozzle exit where the boundary layer is thinnest. Proceeding from top to bottom, the shock is

progressively further from the nozzle exit and the boundary layer is correspondingly thicker, yielding increased values of the confinement parameter. In Figure 20 the same sequence of cases is given, now with increased Schlieren sensitivity. The turbulence structure is more visible in Figure 20, but the shock structure is somewhat obscured by the side wall interaction which appears as a dark region in front of the first shock and behind the central part of the later shocks. The shock train is very symmetric in all cases except $\delta_0/h = 0.06$ where a slight asymmetry occurs. In all cases an increase in the boundary layer thickness and an amplification of the turbulence scales is observed going through the interaction. The first shock is always bifurcated, while the following 'secondary' shocks are not. The bifurcated shock consists of a leading oblique shock, a nearly normal outer shock, and a trailing oblique shock with the three intersecting at the bifurcation point. The outer normal shock is concave facing upstream. A slip line is also generated at the bifurcation point and extends downstream. This slip line is visible in Figure 16(a) for $\delta_0/h = 0.34$ where the knife edge is horizontal. A weak reflected wave is caused by the trailing shock's intersection with the boundary layer. The outer, nearly normal shock, trailing shock, and reflected wave form a diamond shaped region where the flow is accelerating, as indicated by the lighter shading. Downstream of the diamond region, the darker shading indicates the flow is only weakly accelerating or even decelerating. The size and shape of the first shock and the diamond region remains approximately the same as δ_0/h increases, with the height of the bifurcation point above the wall increasing only slightly. The distance from the end of the diamond (i. e. where the reflected waves cross) to the second shock increases as confinement levels increase.

The shocks following the first shock, termed secondary shocks, are similar to each other but are different in character than the first shock. The secondary shocks are unbifurcated. The outer region is nearly normal, being concave facing downstream as opposed to the first shock in which the normal portion was concave facing upstream. An inflection point in the shock shape is seen to occur where the slip line from the bifurcation point of the first shock crosses the secondary shocks. This is especially visible in Figure 21(a) with horizontal knife

edge. Both high and low sensitivity Schlieren photographs with a vertical knife edge are shown in Figures 21(b) and 21(c), respectively, such that an easy comparison between the three types of Schlieren photographs can be made. A diamond shaped reacceleration region follows each secondary shock, but is not as well defined as the first diamond. Within a single shock train, the spacing between successive downstream shocks decreases. As confinement increases, the number of secondary shocks, the spacing between respective shocks in each shock train, and the overall length of the interaction increase.

The steadiness of the interaction was observed with the Schlieren light source in the continuous viewing mode. The mean shock train location was fixed with only very small amplitude oscillations in the leading shock's location. Each successive secondary shock showed motion of increasing amplitude. The last few secondary shocks in each shock train were very weak and displayed movement on the order of an undisturbed boundary layer thickness, δ_u . This shock motion was in the streamwise direction. No noticeable motion was observed in the direction normal to the wall. These observations of the shock unsteadiness agree with those of Ikui, et al.²⁹.

The surface flow visualization for $\delta_u/h = 0.34$ and Mach 1.6 is shown in Figure 22. As was done with the Mach 2.45 case, the top and bottom test section wall surface oil flow streak patterns are shown above and below the side view Schlieren photograph. This figure is representative of all the surface flow results at Mach 1.6. On the top wall, discrete drops of oil were placed on the duct wall. On the bottom wall, the entire surface was coated with oil. A small separation region is seen below the first shock. A distinct separation and reattachment line were not formed due to the small size of the separation. A slightly larger separation is seen near the corner and along the centerline. The secondary shocks do not appear to separate the flow. A corner effect is set up after the side wall separation under the first shock and continues to grow with downstream distance. The flow after the first shock appears to flow out of the corner, possibly due to some type of rotating secondary flow in the corner. At the downstream edge of the picture, the middle 50% of the flow is still two-dimensional.

2. MACH 1.6 PRESSURE MEASUREMENTS

The wall static pressure measurements for the six cases in Table 7 are presented in Figures 23, 24, and 25. The wall static pressure, P , has been normalized by the upstream stagnation pressure, p_0 . In Figure 23 the wall pressure is plotted versus the distance from the nozzle exit. The small pressure gradient in the undisturbed boundary layer is apparent. As the shock train is moved away from the nozzle exit to a location with higher confinement, the length of the pressure rise increases and the overall pressure recovery decreases. The ideal pressure recovery through a normal shock at Mach 1.6 is $p/p_0 = 0.6634$. The pressure recovery through the shock train interaction was $p/p_0 = 0.6094, 0.5962, 0.5735, 0.5582, 0.5358, \text{ and } 0.4998$ or 91.9%, 89.9%, 86.6%, 84.1%, 80.8%, and 73.35% of the ideal value for $\delta_u/h = 0.06, 0.14, 0.20, 0.26, 0.34, \text{ and } 0.44$, respectively. The pressure recovery has been completed by the duct exit for the first four cases, possibly the fifth case, but not for the sixth case where the shock train is closest to the exit. Two causes are responsible for the drop in pressure recovery at higher confinement levels. First, the shock system is longer with higher losses for the increased confinement and second, the interaction occurs at a slightly lower Mach number as the boundary layer thickens due to the slight adverse pressure gradient in the undisturbed boundary layer. In Figure 24 the pressure traces have been shifted with the downstream distance now being measured from the start of the interaction. The pressure traces fail to collapse to a single curve as they did in the Mach 2.45 case, the reason being that the spacing between shocks and the number of shocks in the shock train is now strongly linked to the level of confinement. The differences in the shock structure, i. e. an oblique leading shock for $M_u = 2.45$ and a normal shock for $M_u = 1.6$, could also be a contributing factor for this difference in the pressure traces. Recall that a pressure plateau was observed with the oblique leading shock but is no longer present with a bifurcated normal shock. Replotting the data with the downstream distance again measured from the start of the interaction and now non-dimensionalized by the undisturbed boundary layer thickness, δ_u , (Figure 25) causes the

pressure traces to collapse reasonably well to a single curve with the exception of the $\delta_w/h = 0.06$ case. The reason for this exception is unclear but could be due to the asymmetric nature of the shock train for this case.

VI. CONCLUSIONS AND RECOMMENDATIONS

In this final section conclusions are drawn from the experimental and numerical results and some recommendations for further research are made. It is to be emphasized that the results reported herein are partial results, as the LDV investigation of the Mach 1.6 interaction and numerical investigation of the multiple shock interaction have not yet been completed. Thus, only partial conclusions may be made pending the completion of the investigation.

Multiple shock wave/turbulent boundary layer interactions at incoming Mach numbers of 2.45 and 1.6 were studied experimentally. The Mach 2.45 interaction was found to be asymmetric with the leading shock being oblique in nature and the following shocks being more normal in character but tending to exist near either the upper or lower duct wall but not extending completely to the opposing wall. The interaction was neutrally stable with the repeated shock pattern tending to alternate between lying along the upper and lower duct walls at random times. A small scale, high frequency oscillation in the shock location was also observed. The shape and extent of the separation regions on the upper and lower walls were vastly different. The Mach 2.45 interaction was deemed unsuitable for the planned LDV investigation due to the flow unsteadiness and asymmetry. Therefore, an investigation of a Mach 1.6 interaction was also initiated.

The Mach 1.6 interaction consisted of a series of symmetric, nearly normal shocks. The initial, bifurcated shock caused a small separation region at its foot while the weaker, unbifurcated, secondary shocks did not separate the boundary layer. At Mach 1.6 the interaction was much steadier than for the Mach 2.45 case. A detailed LDV investigation of the Mach 1.6 interaction for one shock train location is currently being performed. These results will reveal the exact nature of the flow reacceleration following each shock and will also give information on the turbulence structure through the interaction.

Numerical results have been presented for three test cases. The first two test cases were for equilibrium flat plate boundary layers and were used to ensure that the computer code

was operating correctly and that the computational method was capable of predicting these relatively simple flows. The third test case was a separated oblique shock/turbulent boundary layer interaction at a compression corner. This case is being used to further validate the computational code and to gain experience in calculating a more complicated flowfield before computing the shock train case. The calculation for the third test case, using the Baldwin-Lomax turbulence model, did not accurately predict the size of the separation region caused by the shock. This result was not unexpected and has been previously observed and reported in the literature. A calculation for this case with the Wilcox-Rubesin two-equation turbulence model is currently being performed and is expected to yield much improved results. The final calculation to be performed is for the Mach 1.6 multiple normal shock/turbulent boundary layer interaction being investigated experimentally with the LDV system.

Several areas requiring further research have been identified. The steadiness of both the multiple normal and oblique shock/turbulent boundary layer interactions in nearly constant area ducts is questionable. The exact mechanisms which trigger and amplify the shock motion are poorly understood. The relative steadiness of planar versus axisymmetric geometries is also unknown. Three-dimensional effects present in planar geometries need to be investigated further. Finally, more work needs to be done at higher Mach numbers, i.e. Mach numbers above 1.8. The bulk of the previous research has focused on low Mach number interactions, perhaps because the multiple shock interaction is inherently steadier at lower Mach numbers and, consequently, easier to handle experimentally. However, many applications will require an understanding of the shock train phenomenon at higher Mach numbers. The transition of the shock train from a normal shock train to an oblique shock train at higher Mach numbers is poorly understood. Additionally, the exact nature of the oblique shock system (strong or weak oblique shocks) at higher Mach numbers is unclear.

VII. REFERENCES

- 1 Williams, R. M., "National Aero-Space Plane: Technology for America's Future," Aerospace America, November 1986, p. 18.
- 2 Dwoyer, D. L., Kutler, P., and Povinelli, L. A., "Retooling CFD for Hypersonic Aircraft," Aerospace America, October 1987, p. 32.
- 3 Hsieh, T., Bogar, T. J., and Coakley, T. J., "Numerical Simulation and Comparison with Experiment for Self-Excited Oscillations in a Diffuser Flow", AIAA Journal, Vol. 25, No. 7, July 1987, pp. 936-943.
- 4 Hsieh, T., Wardlaw, A. B. Jr., Collins, P., and Coakley, T. J., "Numerical Simulation of a Ramjet Inlet Flow in Response to Large Amplitude Combustor Pressure Oscillation," AIAA Paper 84-1363, June 1984.
- 5 Bogar, T. J., "Structure of Self-Excited Oscillations in Transonic Diffuser Flows," AIAA Journal, Vol. 24, No. 1, January 1986, pp. 54-61.
- 6 Bogar, T. J., Sajben, M., Kroutil, J. C., "Response of a Supersonic Inlet to Downstream Perturbations," AIAA Journal of Propulsion and Power, Vol. 1, No. 2, March-April, 1985, pp. 118-125.
- 7 Sajben, M., Bogar, T. J., and Kroutil, J. C., "Experimental Study of Flows in a Two-Dimensional Inlet Model," AIAA Journal of Propulsion and Power, Vol. 1, No. 2, March-April 1985, pp. 109-117.
- 8 Talcott, N. A., Jr. and Kumar, A., "Two-Dimensional Viscous Simulation of Inlet/Diffuser Flows with Terminal Shocks", AIAA Journal of Propulsion and Power, Vol. 1, No. 2, March-April 1985, pp. 103-108.
- 9 Waltrup, P. J., "Liquid Fueled Supersonic Combustion Ramjets: A Research Perspective of the Past, Present and Future," AIAA Paper 86-0158, January 1986.
- 10 White, M. E., Drummond, J. P., and Kumar, A., "Evolution and Application of CFD Techniques for Scramjet Engine Analysis," AIAA Journal of Propulsion and Power, Vol. 3, No. 5, September-October, 1987, pp 423-439.
- 11 Yanta, W., Naval Surface Weapons Center, Silver Spring, MD, private communication.
- 12 Reda, D. C. and Murphy, J. D., "Shock Wave/Turbulent Boundar-Layer Interactions in Rectangular Channels," AIAA Journal, Vol. 11, No. 2, February 1973, pp. 139-140.
- 13 Law, C. H., "Supersonic Shock Wave Turbulent Boundary-Layer Interactions," AIAA Journal, Vol. 14, No. 6, June 1976, pp. 730-734.
- 14 Fisher, S. A., "Three-Dimensional Flow Effects in a Two-Dimensional Supersonic Air Intake," AIAA Journal of Propulsion and Power, Vol. 2, No. 6, Nov.-Dec. 1986, pp. 546-551.

- 15 Chriss, R. M., Keith, T. G., Jr., Hingst, W. R., Strazisar, A. J., and Porro, A. R., "An LDA Investigation of Three-Dimensional Normal Shock-Boundary Layer Interactions in a Corner," AIAA Paper 87-1369, June 1987.
- 16 Green, J. E., "Interactions Between Shock Waves and Turbulent Boundary Layers," Progress in Aerospace Sciences, Vol. 11, 1970, Pergamon Press, pp. 235-341.
- 17 Adamson, T. C. and Messiter, A. F., "Analysis of Two-Dimensional Interactions Between Shock Waves and Boundary Layers," Annual Review of Fluid Mechanics, Vol. 12, 1980, Annual Reviews Inc., Palo Alto, Calif., pp. 103-138.
- 18 Seddon, J., "The Flow Produced by Interaction of a Turbulent Boundary Layer with a Normal Shock of Strength Sufficient to Cause Separation," Aeronautical Research Council Reports and Memoranda No. 3502, March 1960.
- 19 Vidal, R. J., Wittliff, C. E., Catlin, P. A., and Sheen, B. H., "Reynolds Number Effects in the Shock Wave - Turbulent Boundary Layer Interaction at Transonic Speeds," AIAA Paper No. 73-661, July 1973.
- 20 Kooi, J. W., "Experiment on Transonic Shock-Wave Boundary Layer Interaction," (NATO) AGARD Conference Proceedings No. 168, May 1975.
- 21 East, L. F., "The Application of a Laser Anemometer to the Investigation of Shock-Wave Boundary Layer Interactions," (NATO) AGARD Conference Proceedings No. 193, May 1976.
- 22 Delery, J. M., "Experimental Investigation of Turbulence Properties in Transonic Shock/Boundary Layer Interactions," AIAA Journal, Vol. 21, No. 2, February 1983, pp. 180-185.
- 23 Lustwerk, F., "The Influence of Boundary Layer on the 'Normal' Shock Configuration," Meteor. Report No. 61, Massachusetts Institute of Technology Guided Missiles Program, Cambridge Massachusetts, September, 1950.
- 24 Merkli, P. E., "Pressure Recovery in Rectangular Constant Area Supersonic Diffusers," AIAA Journal, Vol. 14, No. 2, February 1986, pp. 168-172.
- 25 Mateer, G. G. and Viegas, J. R., "Effect of Mach and Reynolds Numbers on a Normal Shock-Wave/Turbulent Boundary-Layer Interaction," AIAA Paper No. 79-1502, July 1979.
- 26 McLafferty, G. H., Krasnoff, E. L., Ranard, E. D., Rose, W. G., and Vergara, R. D., "Investigation of Turbojet Inlet Design Parameters," Report No. R-0790-13, United Aircraft Corp., Research Dept., East Hartford, Connecticut, December 1955, pp. 17-58.
- 27 Fejer, A. A., Heath, G. L., and Driftmeyer, R. T., "An Investigation of Constant Area Supersonic Flow Diffusion," ARL Report No. 64-81, Aerospace Research Laboratories, Office of Aerospace Research, Wright-Patterson Air Force Base, Ohio, May 1964.
- 28 Ikui, T., Matsuo, K., and Nagai, M., "The Mechanisms of Psuedo-Shock Waves," Bulletin of the JSME, Vol. 17, No. 108, June 1974, pp. 731 - 739.
- 29 Ikui, T., Matsuo, K., Nagai, M., and Honjo, M., "Oscillation Phenomena of Psuedo-Shock Waves," Bulletin of the JSME, Vol. 17, No. 112, October 1974, pp. 1278-1285.

- 30 Ikui, T., Matsuo, K., Mochizuki, H., and Somekawa, K., "Psuedo-Shock Waves in a Divergent Channel," Bulletin of the JSME, Vol. 23, No. 175, January 1980, pp. 20-25.
- 31 Johnson, J. A. and Wu, B. J. C., "Pressure Recovery in Supersonic Diffusers," ASME Journal of Fluids Engineering, Transactions of the ASME, September 1975, pp. 374-376.
- 32 Waltrup, P. J. and Billig, F. S., "Structure of Shock Waves in Cylindrical Ducts," AIAA Journal, Vol. 11, No. 10, October 1973, pp. 1404-1408.
- 33 Mateer, G. G., Brosh, A., and Viegas, J. R., "A Normal Shock-Wave Turbulent Boundary-Layer Interaction at Transonic Speeds," AIAA Paper No. 76-161, Jan. 1976.
- 34 Om, D., Childs, M. E., and Viegas, J. R., "An Experimental Investigation and Numerical Prediction of a Transonic Normal Shock/Turbulent Boundary Layer Interaction," AIAA Paper No. 82-0990, June 1982.
- 35 Om, D. and Childs, M. E., "An Experimental Investigation of Multiple Shock Wave/Turbulent Boundary Layer Interactions in a Circular Duct," AIAA Paper No. 83-1744, July 1983.
- 36 Cuffel, R. F. and Back, L. H., "Flow and Heat Transfer Measurements in a Pseudo-Shock Region with Surface Cooling," AIAA Journal, Vol. 14, No. 12, December 1976, pp. 1716-1722.
- 37 MacCormack, R. W. and Baldwin, B. S., "A Numerical Method for Solving the Navier-Stokes Equations with Application to Shock-Boundary Layer Interactions," AIAA Paper No. 75-1, January 1975.
- 38 Wilcox, D. C., "Numerical Study of Separated Turbulent Flows," AIAA Journal, Vol. 13, No. 5, May 1975, pp. 555-556.
- 39 Shang, J. S. and Hankey, W. L., "Numerical Solution for Supersonic Turbulent Flow over a Compression Ramp," AIAA Journal, Vol. 13, No. 10, October 1975, pp. 1368-1374.
- 40 Deiwert, G. S., "Computation of Separated Transonic Turbulent Flows," AIAA Journal, Vol. 14, No. 6, June 1976, pp. 735-740.
- 41 Hung, C. M. and MacCormack, R. W., "Numerical Solutions of Supersonic and Hypersonic Laminar Compression Corner Flows," AIAA Journal Vol. 14, No. 4, April 1976, pp. 475-481.
- 39 Hung, C. M. and MacCormack, R. W., "Numerical Solutions of Supersonic and Hypersonic Turbulent Compression Corner Flows," AIAA Journal, Vol. 15, No. 3, March 1977, pp. 410-416.
- 43 Hung, C. M. and MacCormack, R. W., "Numerical Solution of Three-Dimensional Shock Wave and Turbulent Boundary-Layer Interaction," AIAA Journal, Vol. 16, No. 10, October 1978, pp. 1090-1096.
- 44 Settles, G. S., Fitzpatrick, T. J., and Bogdonoff, S. M., "Detailed Study of Attached and Separated Compression Corner Flowfields in High Reynolds Number Supersonic Flow," AIAA Journal, Vol. 17, No. 6, June 1979, pp. 579-585.

- 45 Horstman, C. C., Settles, G. S., Vas, I. E., Bogdonoff, S. M., and Hung, C. M., "Reynolds Number Effects on Shock-Wave Turbulent Boundary-Layer Interactions," AIAA Journal, Vol. 15, No. 8, August 1977, pp. 1152-1158.
- 46 Coakley, J. R., Viegas, J. R., and Horstman, C. C., "Evaluation of Turbulence Models for Three Primary Types of Shock Separated Boundary Layers," AIAA Paper No. 77-692, June 1977.
- 47 Viegas, J. R. and Coakley, T. J., "Numerical Investigation of Turbulence Models for Shock-Separated Boundary Layer Flows," AIAA Journal, Vol. 16, No. 4, April 1978, pp. 293-294.
- 48 Viegas, J. R. and Horstman, C. C., "Comparison of Multiequation Turbulence Models for Several Shock Boundary-Layer Interaction Flows," AIAA Journal, Vol. 17, No. 8, August 1979, pp. 811-820.
- 49 Viegas, J. R. and Horstman, C. C., "Comparison of Multiequation Turbulence Models for Several Shock Separated Boundary Layer Flows," AIAA Paper No. 78-1165, July 1978.
- 50 MacCormack, R. W., "Numerical Solution of the Interaction of a Shock Wave with a Laminar Boundary Layer," Lecture Notes in Physics, Vol. 8, Springer-Verlag, 1971, pp. 151-163.
- 51 MacCormack, R. W., "An Efficient Numerical Method for Solving the Time-Dependent Compressible Navier-Stokes Equations at High Reynolds Number," Computing in Applied Mechanics, AMD Vol. 18, ASME, 1976.
- 52 Rubesin, M. W., "A One-Equation Model of Turbulence for Use with the Compressible Navier-Stokes Equations," NASA TM X-73, 128, April 1976.
- 53 Jones, W. P. and Launder, B. E., "The Prediction of Laminarization with a Two-Equation Model of Turbulence," Int. Journal of Heat and Mass Transfer, Vol. 15, Pergamon Press, 1972, pp. 301-313.
- 54 Wilcox, D. C. and Rubesin, M. W., "Progress in Turbulence Modeling for Complex Flow Fields Including Effects of Compressibility," NASA TP 1517, 1980.
- 55 Knight, D. D., "Numerical Simulation of Realistic High-Speed Inlets Using the Navier-Stokes Equations," AIAA Journal, Vol. 15, No. 11, November 1977, pp. 1583-1589.
- 56 Knight, D. D., "Improved Calculation of High Speed Inlet Flows: Part I. Numerical Algorithm," AIAA Journal, Vol. 19, No. 1, January 1981, pp. 34-41.
- 57 Knight, D. D., "Improved Calculations of High Speed Inlet Flows: Part II. Results," AIAA Journal, Vol. 19, No. 2, February 1981, pp. 172-179.
- 58 Kumar, A., "Numerical Analysis of the Scramjet-Inlet Flow Field by Using Two-Dimensional Navier-Stokes Equations," NASA TP 1940, December 1981.
- 59 Kumar, A., "User's Guide for NASCRIN - A Vectorized Code for Calculating Two-Dimensional Supersonic Internal Flow Fields," NASA TM 85708, February 1984.

- 60 Kumar, A., "Numerical Simulation of Flow Through Scramjet Inlets Using a Three-Dimensional Navier-Stokes Code," AIAA Paper No. 85-1664, July 1985.
- 61 Drummond, J. P. and Weidner, E. H., "Numerical Study of a Scramjet Engine Flowfield," AIAA Journal, Vol. 20, No. 9, September 1982, pp. 1182-1187.
- 62 Coakley, J. R. and Hsieh, T., "A Comparison Between Implicit and Hybrid Methods for the Calculation of Steady and Unsteady Inlet Flows," AIAA Paper No. 85-1125, July 1985.
- 63 Hunter, L. G., Tripp, J. M., and Howlett, D. G., "A Mach 2.0 Plus Supersonic Inlet Study Using the Navier-Stokes Equations," AIAA Paper No. 85-1211, July 1985.
- 64 Paynter, G. C. and Chen, H. C., "Progress Toward the Analysis of Supersonic Inlet Flows," AIAA Paper No. 83-1371, June 1983.
- 65 Chaussee, D. S. and Pulliam, T. H., "Two-Dimensional Inlet Simulation Using a Diagonal Implicit Algorithm," AIAA Journal, Vol. 19, No. 2, February 1981, pp. 153-159.
- 66 Beam, R. and Warming, R. F., "An Implicit Finite-Difference Algorithm for Hyperbolic Systems in Conservation-Law Form," Journal of Computational Physics, Vol. 22, September 1976, pp. 87-110.
- 67 Baldwin, W. D. and Lomax, H., "Thin Layer Approximation and Algebraic Model for Separated Turbulent Flows," AIAA Paper No. 78-257, 1978.
- 68 Visbal, M. and Knight, D., "The Baldwin-Lomax Turbulence Model for Two-Dimensional Shock-Wave/Boundary-Layer Interactions," AIAA Journal, Vol. 22, No. 7, July 1984, pp. 921-928.
- 69 MacCormack, R. W., "The Effect of Viscosity in Hypervelocity Impact Cratering," AIAA Paper No. 69-354, April 1969.
- 70 Rudy, D. H., NASA-Langley Research Center, Langley, Virginia, private communications.
- 71 Rudy, D. H. and Strikwerda, J. C., "A Nonreflecting Outflow Boundary Condition for Subsonic Navier-Stokes Calculations," Journal of Computational Physics, Vol. 36, 1980, pp. 55-70.
- 72 Cline, M. C., "VNAP: A Computer Program for Computation of Two-Dimensional, Time-Dependent, Compressible, Viscous, Internal Flow," Report No. LA-7326, Los Alamos National Laboratory, Los Alamos, New Mexico, Nov. 1978.
- 73 Cline, M. C., "VNAP2: A Computer Program for Computation of Two-Dimensional, Time-Dependent, Compressible, Turbulent Flow," Report No. LA-8872, Los Alamos National Laboratory, Los Alamos, New Mexico, August 1981.
- 74 Viegas, J. R. and Rubesin, M. W., "Wall-Function Boundary Conditions in the Solution of the Navier-Stokes Equations for Complex Compressible Flows," AIAA Paper No. 83-1694, July 1983.

- 75 Viegas, J. R., Rubesin, M. W., and Horstman, C. C., "On the Use of Wall Functions as Boundary Conditions for Two-Dimensional Separated Compressible Flows," AIAA Paper No. 85-0180, January 1985.
- 76 Carroll, B. F., Dutton, J. C., and Addy, A. L., "NOZCS2: A Computer Program for the Design of Continuous Slope Supersonic Nozzles," Department of Mechanical and Industrial Engineering, University of Illinois at Urbana-Champaign, Report No. UILU ENG 86-4007, August 1986.
- 77 Bradshaw, P., "The Effect of Wind-Tunnel Screens on Nominally Two-Dimensional Boundary Layers," Journal of Fluid Mechanics, Vol. 2, Part 4, 1965, pp. 679-687.
- 78 Baines, W. D. and Peterson, E. G., "An Investigation of Flow Through Screens," ASME Transactions, Vol. 73, 1951, pp. 467-480.
- 79 Dutton, J. C. and Addy, A. L., "Theory, Computer Program, and Illustrative Examples for the Two-Dimensional Boundary Layer Flow of Ideal Gases," Technical Report T-CR-78-10, U. S. Army Missile Research and Development Command, Redstone Arsenal, Alabama, March 1978.
- 80 Johnson, D. A. and Rose, W. C., "Laser Velocimetry and Hot-Wire Anemometer Comparison in a Supersonic Boundary Layer," AIAA Journal, Vol. 13, No. 4, April 1975, pp. 512-515.
- 81 Ardonceau, P. L., "The Structure of Turbulence in a Supersonic Shock-Wave/Boundary-Layer Interaction," AIAA Journal, Vol. 22, No. 9, September 1984, pp. 1254-1262.
- 82 Petrie, H. L., "A Study of Compressible Turbulent Free Shear Layers Using Laser Doppler Velocimetry," Ph.D. Thesis, Department of Mechanical and Industrial Engineering, University of Illinois at Urbana-Champaign, Urbana, IL, 1984.
- 83 Samimy, M., "An Experimental Study of Compressible Turbulent Reattaching Free Shear Layers," Ph.D. Thesis, Department of Mechanical and Industrial Engineering, University of Illinois at Urbana-Champaign, Urbana, IL, 1984.
- 84 Kuntz, D. W., "An Experimental Investigation of the Shock Wave-Turbulent Boundary Layer Interaction," Ph.D. Thesis, Department of Mechanical and Industrial Engineering, University of Illinois at Urbana-Champaign, Urbana, IL, 1985.
- 85 Petrie, H. L., Samimy, M., and Addy, A. L., "An Evaluation of LDV Velocity and Fringe Bias Effects in Separated High Speed Turbulent Flows," Proceedings of the 11th International Congress on Instrumentation for Aerospace Simulation Facilities," ICIASF Record '85, IEEE Publication, New York, August 1985, pp. 297-308.
- 86 McLaughlin, D. K. and Tiedermann, W. G., Jr., "Biasing Correction for Individual Realization of Laser Anemometer Measurements in Turbulent Flow," The Physics of Fluids, Vol. 16, No. 12, 1973, pp. 2082-2088.
- 87 Davis, D. O., Gessner, F. B., and Kerlick, G. D., "Experimental and Numerical Investigation of Supersonic Flow Through a Square Duct," AIAA Paper No. 85-1622, July 1985.

TABLE I
UNCONFINED INTERACTION STUDIES

Ref.	M	Re/m	Re_{0u}	Re_{0u}	θ_u/h	δ_u/h	Geometry	Comments
Sekidani ¹⁸	1.47	9.84×10^6		4×10^4		0.053	Planar $15.2 \times 10.2 \text{ cm}^2$	Single Normal Shock Separated, Supersonic Tongue
Vidal, et al. ¹⁹	1.40	$Re_S =$ 9×10^6 to 36×10^6					Planar	Single Normal Shock Separated
Koon ²⁰	1.40	4.5×10^7	2.2×10^4	3×10^5			Planar Slotted Upper Wall	Single Normal Shock Separated, No Supersonic Tongue
East ²¹	1.30	10×10^6		4×10^5		0.105	Planar $91.5 \times 76.2 \text{ cm}^2$	Single Normal Shock No Supersonic Tongue
	1.40	10×10^6		4×10^5		0.105	Planar $91.5 \times 76.2 \text{ cm}^2$	Single Normal Shock Supersonic Tongue
	1.54	10×10^6		4×10^5		0.105	Planar $91.5 \times 76.2 \text{ cm}^2$	Single Normal Shock Supersonic Tongue
Dalery ²²	1.30	10×10^6					Planar $12 \times 10 \text{ cm}^2$	Single Normal Shock
	1.37	10×10^6				0.061 to	Planar $12 \times 10 \text{ cm}^2$	Single Normal Shock
	1.45	10×10^6				0.104	Planar $12 \times 10 \text{ cm}^2$	Single Normal Shock

TABLE 2
CONTAINED INTERACTION STUDIES

Ref.	M	Re/m	Re _{bu}	Re _{du}	θ_u/τ	δ_u/τ	Geometry	Comments
Lustwerk ²³	2.05						Planar	Single Normal Shock, Multiple Normal Shocks, Multiple Oblique Shocks
McLafferty, et al ²⁶	1.76 1.98 2.20 2.51 1.90						Axisymmetric " " Planar	Various Shock Structures
Fejer ²⁷	1.6 to 2.5						Planar 5.08x2.54 cm ²	Various Shock Structures
Wallrup and Bullig ³²	1.53 2.97 2.60 2.60 2.69 2.72 2.61 1.68	2.2x10 ⁷ to 2.8x10 ⁷ 2.4x10 ⁷ to 3.6x10 ⁷ 3.1x10 ⁷ to 5.5x10 ⁷ 2.9x10 ⁷ to 7.5x10 ⁷ 9.9x10 ⁷ to 12.8x10 ⁷ 17.5x10 ⁷ to 14.6x10 ⁷ 3.4x10 ⁷ to 6.3x10 ⁷ 2.8x10 ⁷ to 4.0x10 ⁷	1.07x10 ⁴ to 1.85x10 ⁴ 0.86x10 ⁴ to 2.15x10 ⁴ 1.07x10 ⁴ to 2.67x10 ⁴ 0.53x10 ⁴ to 3.12x10 ⁴ 2.42x10 ⁴ to 4.68x10 ⁴ 3.20x10 ⁴ to 5.53x10 ⁴ 2.07x10 ⁴ to 5.74x10 ⁴ 0.51x10 ⁴ to 1.04x10 ⁴		.014 to .018 .010 to .017 .010 to .014 .005 to .012 .007 to .010 .005 to .011 .008 to .012 .014 to .020		Axisymmetric D = 6.99 cm " " " " " Axisymmetric D = 15.49 cm Axisymmetric D = 2.54 cm	Normal Shock Multiple Oblique Shocks " " " " " " "
Merkli ²⁴	1.76 to 2.88	0.31x10 ⁷ to 3.1x10 ⁷					Planar 91x.95 cm ²	No Detailed Information on the Shock Structure

TABLE 2
(continued)

CONFINED INTERACTION STUDIES

Ref.	M	Re/m	Re _{0u}	Re _{0u}	θ_u/r	δ_u/r	Geometry	Comments
Ikui, et al. ²⁸	1.33 to						Planar 6x6 cm ²	Single Normal Shock
	1.37 to						"	Multiple Normal Shocks
	1.60						"	Multiple Oblique Shocks
	1.86 to 2.79						"	Multiple Oblique Shocks
Ikui, et al. ²⁹	1.44	3.22x10 ⁷					Planar 6x6 cm ²	Multiple Normal Shocks
	1.93	3.40x10 ⁷					"	Multiple Normal Shocks
	2.79	3.68x10 ⁷					"	Multiple Oblique Shocks
								Shock Motion Studied in All Three
Cuffel and Bach ³⁶	2.92	8.87x10 ⁶	9757	1.67x10 ⁵	.020	.348	Axisymmetric D = 10.8 cm	Single Normal Shock, Separated Surface was cooled
Mateer, et al. ³³	1.5	2.3x10 ⁷		5.83x10 ⁵		.202	Axisymmetric D = 24.77 cm	Single Normal Shock Separated
P. J. and J. J.	1.42	20x10 ⁷ to 80x10 ⁷				.216 to .279	Axisymmetric D = 24.77 cm	Single Normal Shock Unseparated
	.32	"				.443	"	"
		"				.326	"	"
		"				.258	"	"
						.178	"	"
						.099	"	Single Normal Shock Incipient Separation

TABLE 2
(continued)

CONFINED INTERACTION STUDIES

Ref.	M	Re/m	Re _{bu}	Re _{bu}	$\theta_{u/r}$	$\delta_{u/r}$	Geometry	Comments
Om, et al. ³⁴	1.48	4.92x10 ⁶	890	1.03x10 ⁴	.007	.081	Axisymmetric D = 5.19 cm	Single Normal Shock Separated
	1.37	"	979	1.15x10 ⁴	.008	.090	"	Single Normal Shock Incipient Separation
	1.28	"	1127	1.29x10 ⁴	.009	.101	"	Single Normal Shock Unseparated
	1.29	"	920	1.05x10 ⁴	.007	.082	"	"
Om and Childs ³⁵	1.49	4.90x10 ⁶	1955	2.52x10 ⁴	.015	.198	Axisymmetric D = 5.19 cm	Multiple Normal Shocks
	1.3	15.0x10 ⁶						
Chriss, et al. ¹⁵	1.3	15.0x10 ⁶					Planar	Single Normal Shock Unseparated
	1.6	"					30.5x30.5 cm ² "	Multiple Normal Shocks Separated
Current Study	2.45	30.x10 ⁶		9.0x10 ⁴		$\delta_u/h =$.15	Planar 7.62x3.91 cm ²	Multiple Oblique Shocks Separated
	2.45	"		16.2x10 ⁴		.26	7.62x4.14 cm ²	"
	2.45	"		21.9x10 ⁴		.35	7.62x4.23 cm ²	"
	1.60	"		2.7x10 ⁴		.06	7.62x3.21 cm ²	Multiple Normal Shocks Separated
	1.59	"		6.9x10 ⁴		.14	7.62x3.24 cm ²	"
	1.57	"		9.9x10 ⁴		.20	7.62x3.29 cm ²	"
	1.56	"		12.9x10 ⁴		.26	7.62x3.33 cm ²	"
	1.55	"		17.1x10 ⁴		.34	7.62x3.37 cm ²	"
	1.54	"		22.5x10 ⁴		.44	7.62x3.41 cm ²	"

TABLE 3

 $\lambda = 514.4$ nm (Green)

Beam spacing before 2.27x expansion = 50.0 mm

Beam spacing after 2.27x expansion = N. A.

Beam diameter before 2.27x expansion = 1.33 mm

Beam diameter after 2.27x expansion = N. A.

Lens focal length (mm)	120		250		350		600	
Expansion ratio	1.0	2.27	1.0	2.27	1.0	2.27	1.0	2.27
Measurement volume diameter (mm)	.06037	---	.12375	---	.17283	---	.29578	---
Measurement volume length (mm)	.28980	---	1.2375	---	2.4196	---	7.0988	---
Measurement volume height (mm)	.05911	---	.12314	---	.17239	---	.29553	---
Fringe spacing (μ m)	1.2613	---	2.5853	---	3.6107	---	6.1794	---
Number of fringes (Approx.)	48	---	48	---	48	---	48	---
Max. normal velocity (m/s) for 100 MHz max. Doppler frequency (No frequency shifting)	126	---	259	---	361	---	618	---
Max. normal velocity (m/s) for 60 MHz max. Doppler frequency (No frequency shifting)	76	---	155	---	217	---	371	---

TABLE 4

 $\lambda = 514.4 \text{ nm (Green)}$

Beam spacing before 2.27x expansion = 22.0 mm

Beam spacing after 2.27x expansion = 49.94

Beam diameter before 2.27x expansion = 1.33 mm

Beam diameter after 2.27x expansion = 3.02

Lens focal length (mm)	120		250		350		600	
Expansion ratio	1.0	2.27	1.0	2.27	1.0	2.27	1.0	2.27
Measurement volume diameter (mm)	.05935	.02660	.12325	.05452	.17248	.07614	.29558	.13030
Measurement volume length (mm)	.64749	.12781	2.8012	.54580	5.4878	1.0672	16.122	3.1310
Measurement volume height (mm)	.05911	.02604	.12314	.05425	.17239	.07594	.29553	.13019
Fringe spacing (μm)	2.8181	1.2628	5.8522	2.5884	8.1893	3.6150	14.034	6.1868
Number of fringes (Approx.)	21	21	21	21	21	21	21	21
Max. normal velocity (m/s) for 100 MHz max. Doppler frequency (No frequency shifting)	282	126	585	259	819	362	1331	619
Max. normal velocity (m/s) for 60 MHz max. Doppler frequency (No frequency shifting)	169	76	351	155	491	217	799	371

TABLE 5

 $\lambda = 514.4$ nm (Green)

Beam spacing before 2.27x expansion = 13.0 mm
 Beam spacing after 2.27x expansion = 29.51 mm
 Beam diameter before 2.27x expansion = 1.33 mm
 Beam diameter after 2.27x expansion = 3.02 mm

Lens focal length (mm)	120		250		350		600	
Expansion ratio	1.0	2.27	1.0	2.27	1.0	2.27	1.0	2.27
Measurement volume diameter (mm)	.05919	.02623	.12318	.05434	.17242	.07601	.29554	.13023
Measurement volume length (mm)	1.0928	.21335	4.7376	.92069	9.2841	1.8030	27.281	5.2956
Measurement volume height (mm)	.05911	.02604	.12314	.05425	.17239	.07594	.29553	.13019
Fringe spacing (μ m)	4.7562	2.1079	9.8976	4.3663	13.854	6.1076	23.748	10.464
Number of fringes (Approx.)	13	13	13	13	13	13	13	13
Max. normal velocity (m/s) for 100 MHz max. Doppler frequency (No frequency shifting)	476	211	990	437	1385	611	2375	1046
Max. normal velocity (m/s) for 60 MHz max. Doppler frequency (No frequency shifting)	285	126	594	262	831	366	1425	628

TABLE 6
MACH 2.45 EXPERIMENTAL CASES

δ_u (mm)	δ_u/h	M_u	P_0 (psia)	Re/m (m^{-1})	$Re\delta_u$
3.0	0.15	2.45	44.5 ± 1	$30. \times 10^6$	9.0×10^4
5.4	0.26	2.45	44.9 ± 1	$30. \times 10^6$	16.2×10^4
7.3	0.35	2.45	44.9 ± 1	$30. \times 10^6$	21.9×10^4

TABLE 7
MACH 1.6 EXPERIMENTAL CASES

δ_u (mm)	δ_u/h	M_u	P_0 (psia)	Re/m (m^{-1})	$Re\delta_u$
0.9	0.06	1.60	29.9 ± 1	$30. \times 10^6$	2.7×10^4
2.3	0.14	1.59	29.9 ± 1	$30. \times 10^6$	6.9×10^4
3.3	0.20	1.57	29.9 ± 1	$30. \times 10^6$	9.9×10^4
4.3*	0.26	1.56	29.9 ± 1	$30. \times 10^6$	12.9×10^4
5.7	0.34	1.55	29.9 ± 1	$30. \times 10^6$	17.1×10^4
7.5	0.44	1.54	29.9 ± 1	$30. \times 10^6$	22.5×10^4

*Case for the LDV experiments

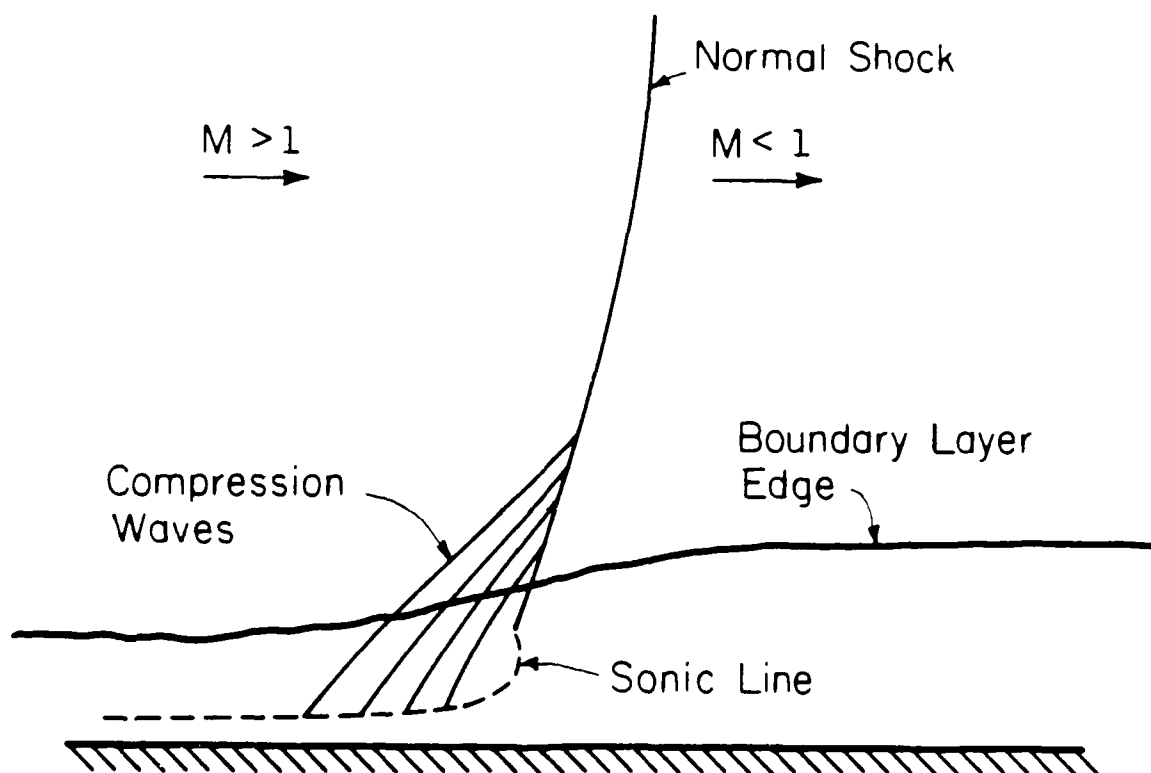


Figure 1. Unconfined, unseparated normal shock/turbulent boundary layer interaction

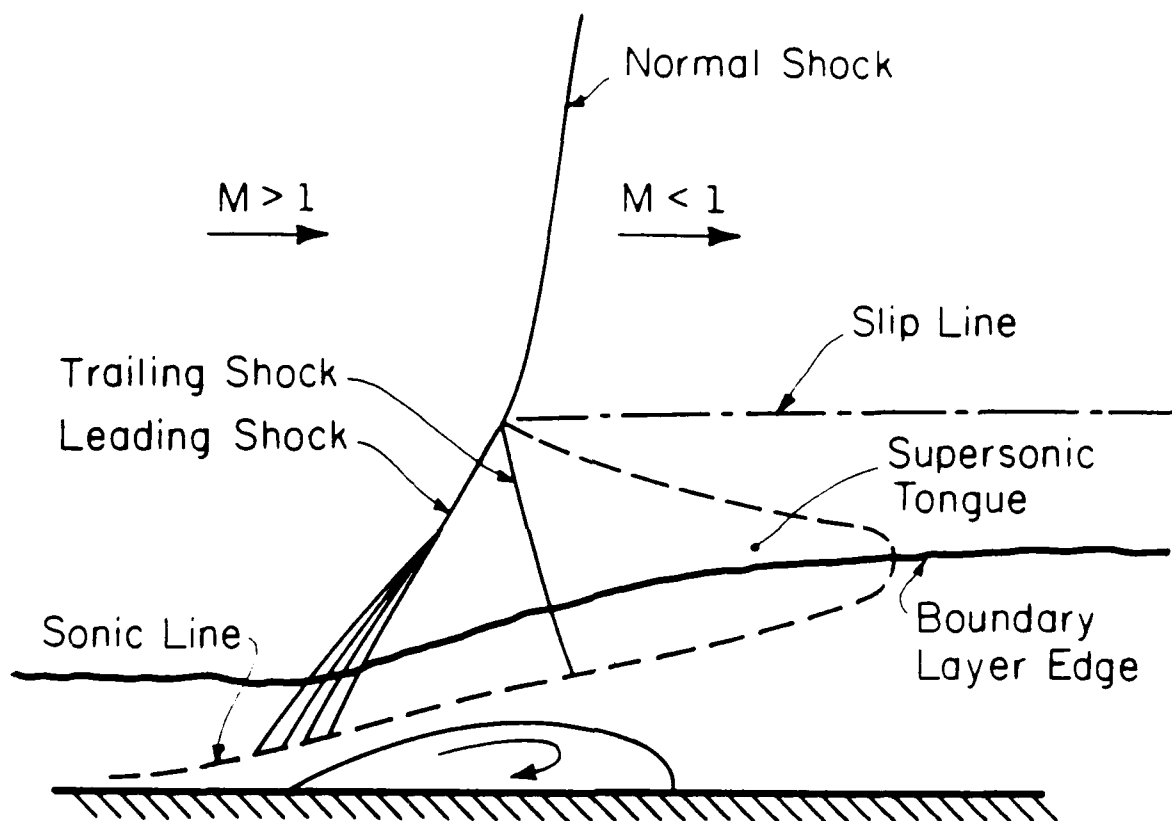


Figure 2. Unconfined, separated normal shock/turbulent boundary layer interaction

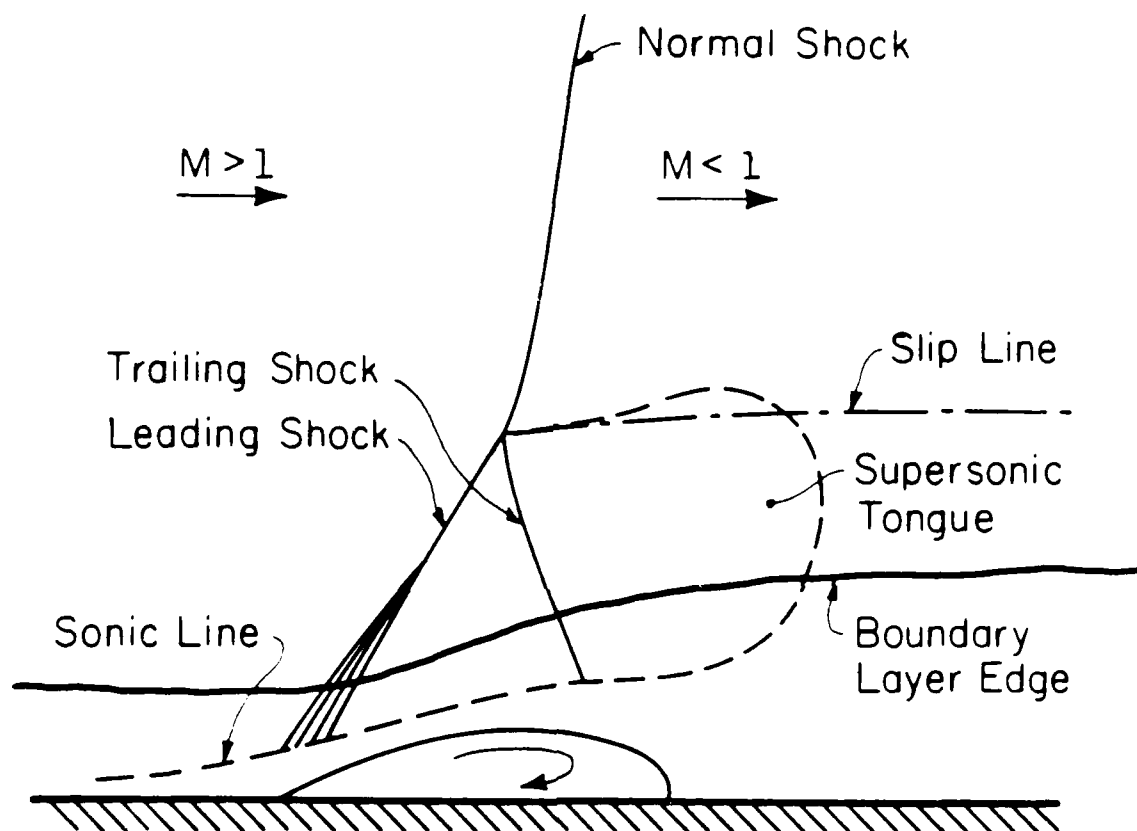


Figure 3. Confined, separated single normal shock/turbulent boundary layer interaction

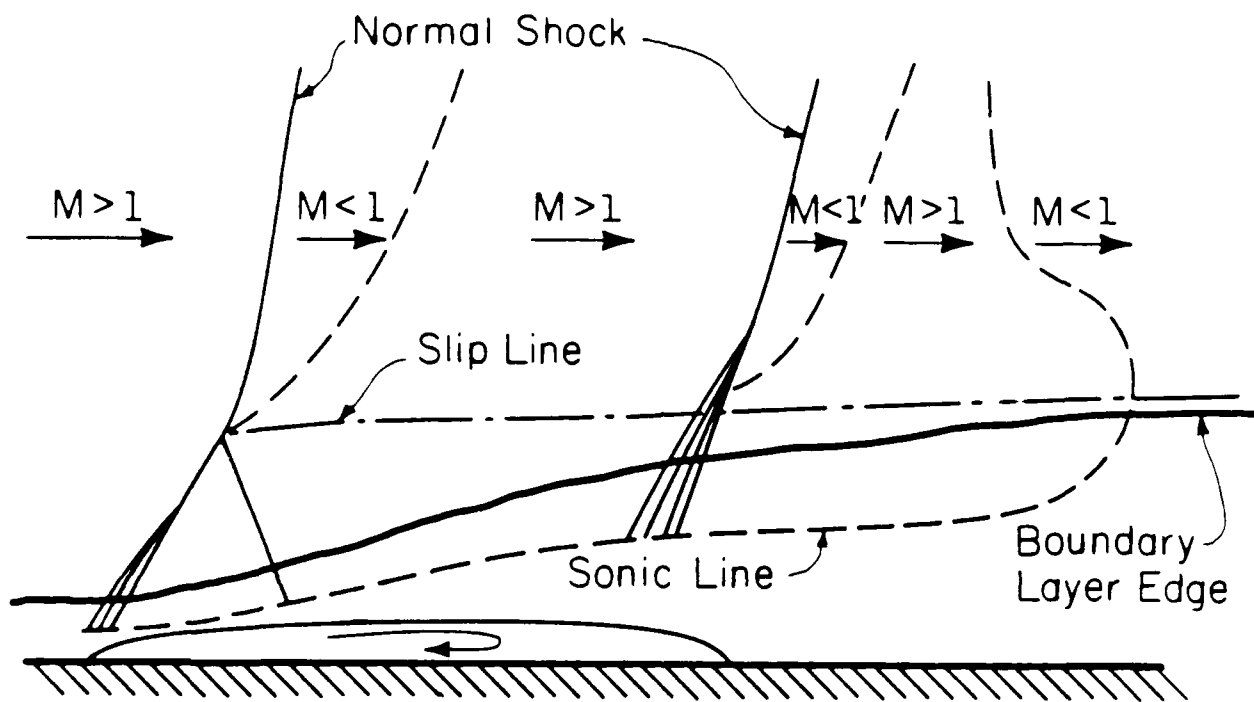


Figure 4. Confined, separated multiple normal shock/turbulent boundary layer interaction

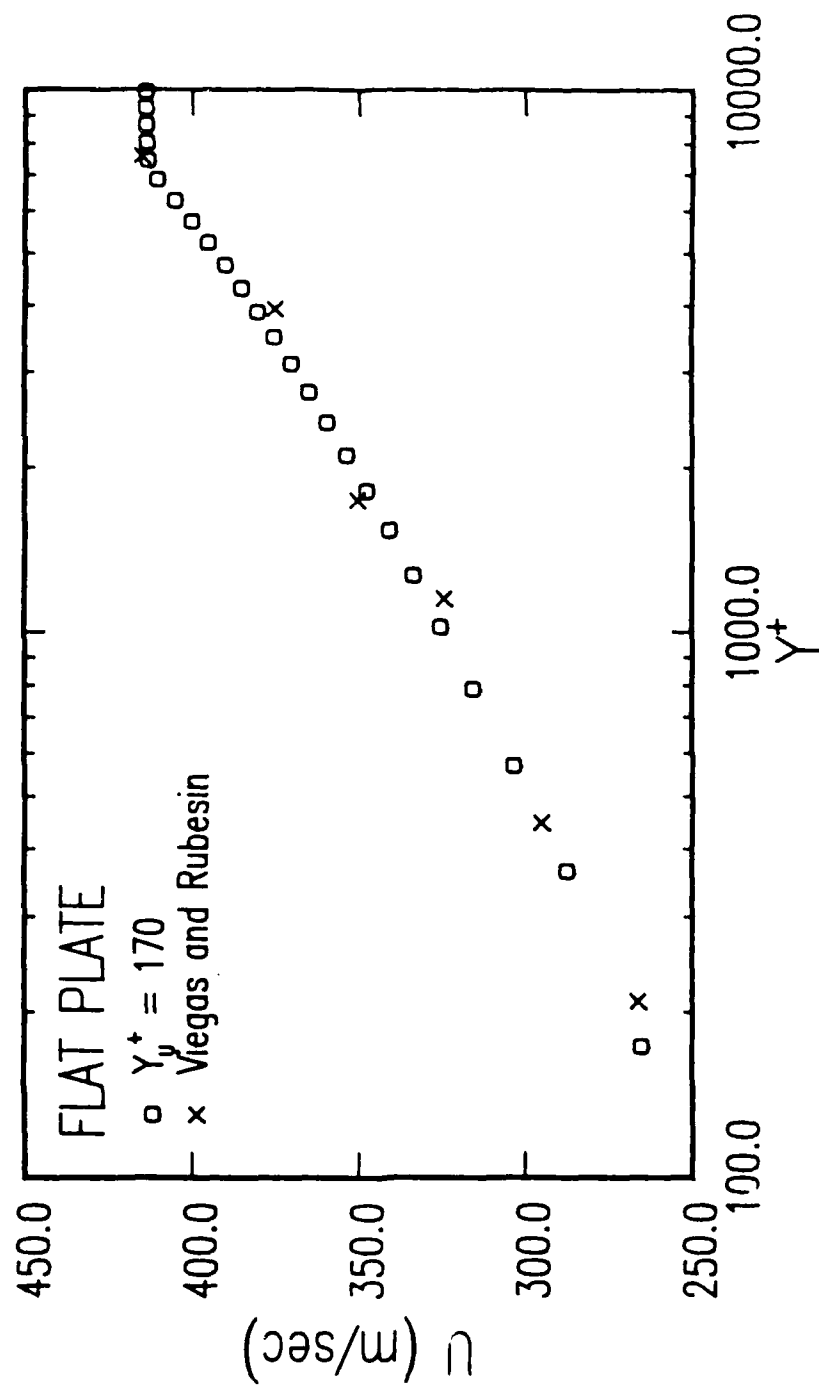


Figure 5. Mean u-velocity profile, equilibrium flat plate boundary layer, $M = 1.48$

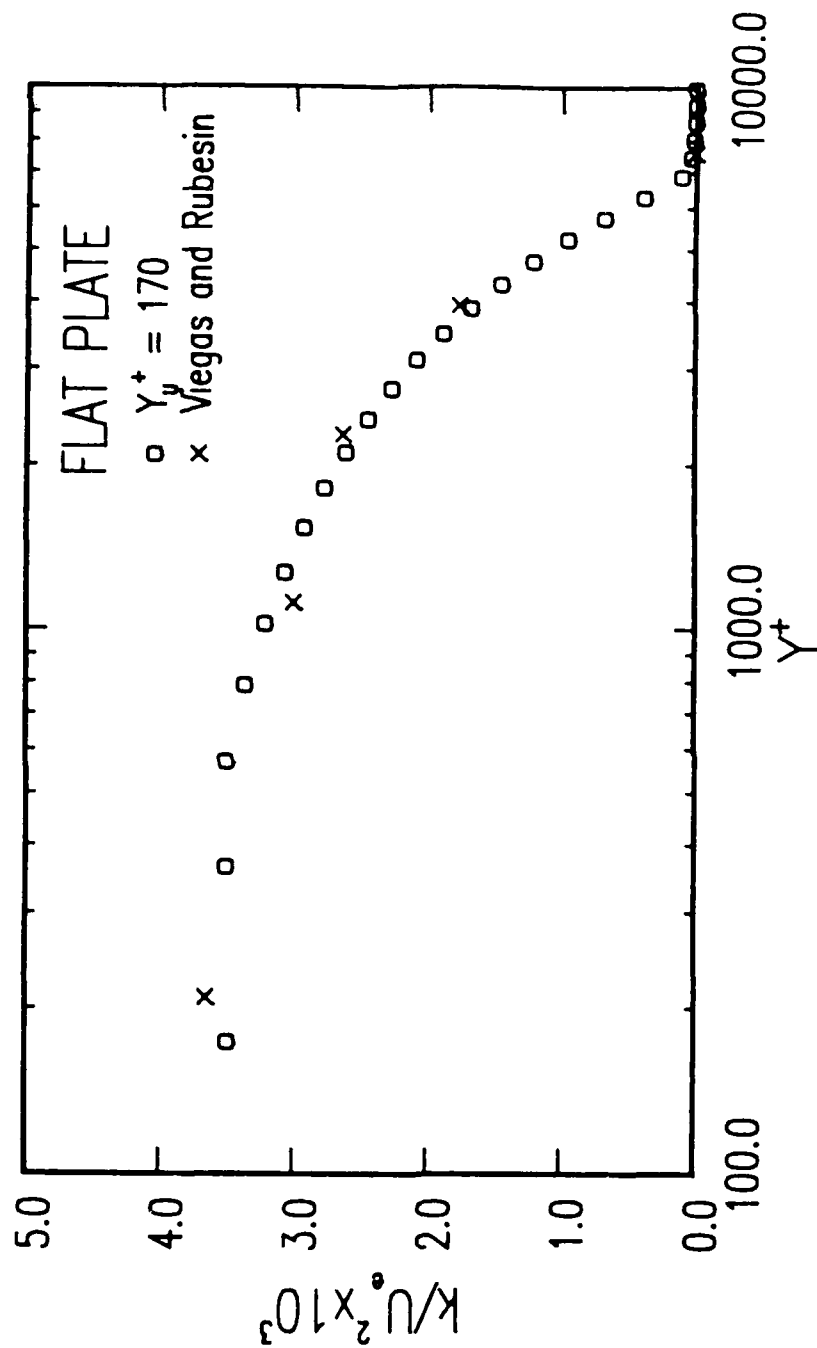


Figure 6. Turbulence kinetic energy profile, equilibrium flat plate boundary layer, $M = 1.48$

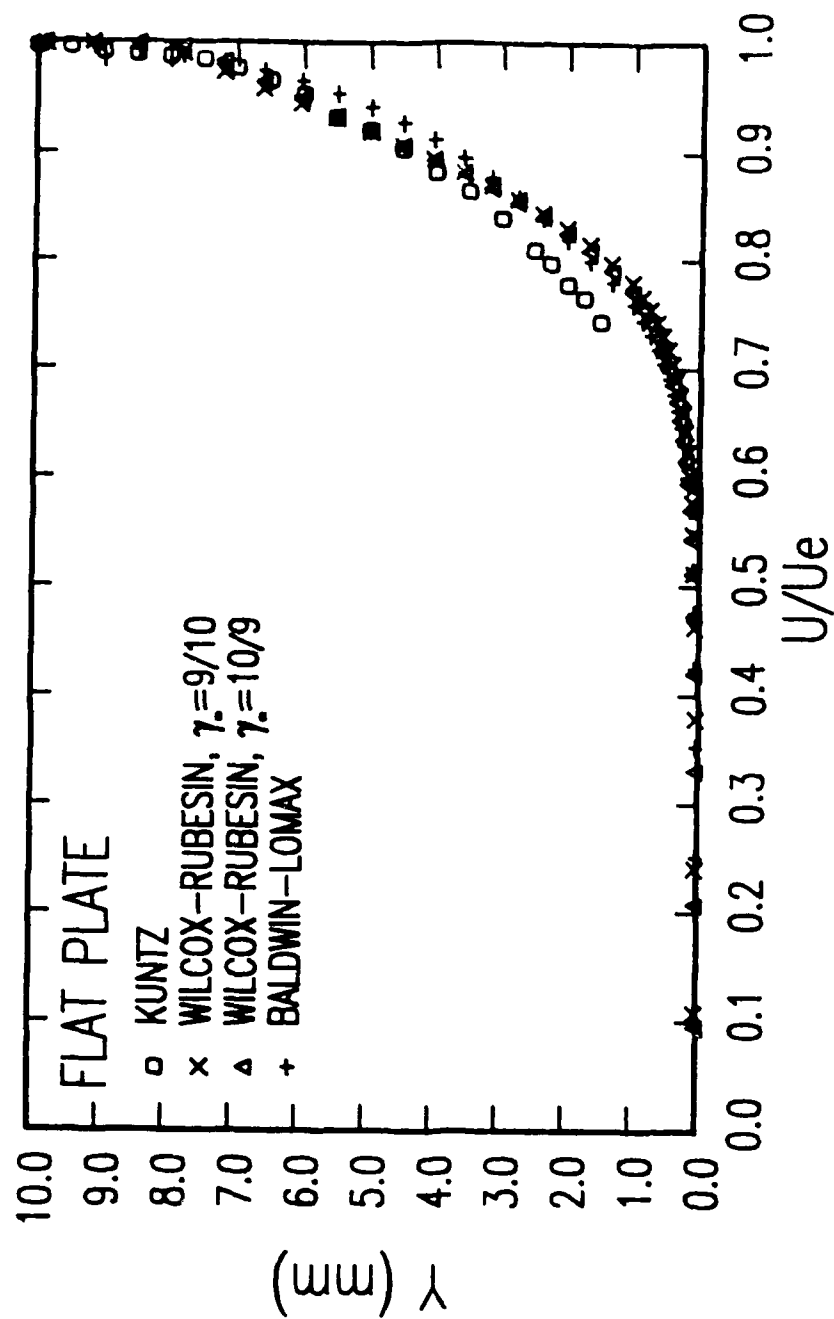


Figure 7. Mean u-velocity profile, equilibrium flat plate boundary layer, $M = 2.94$

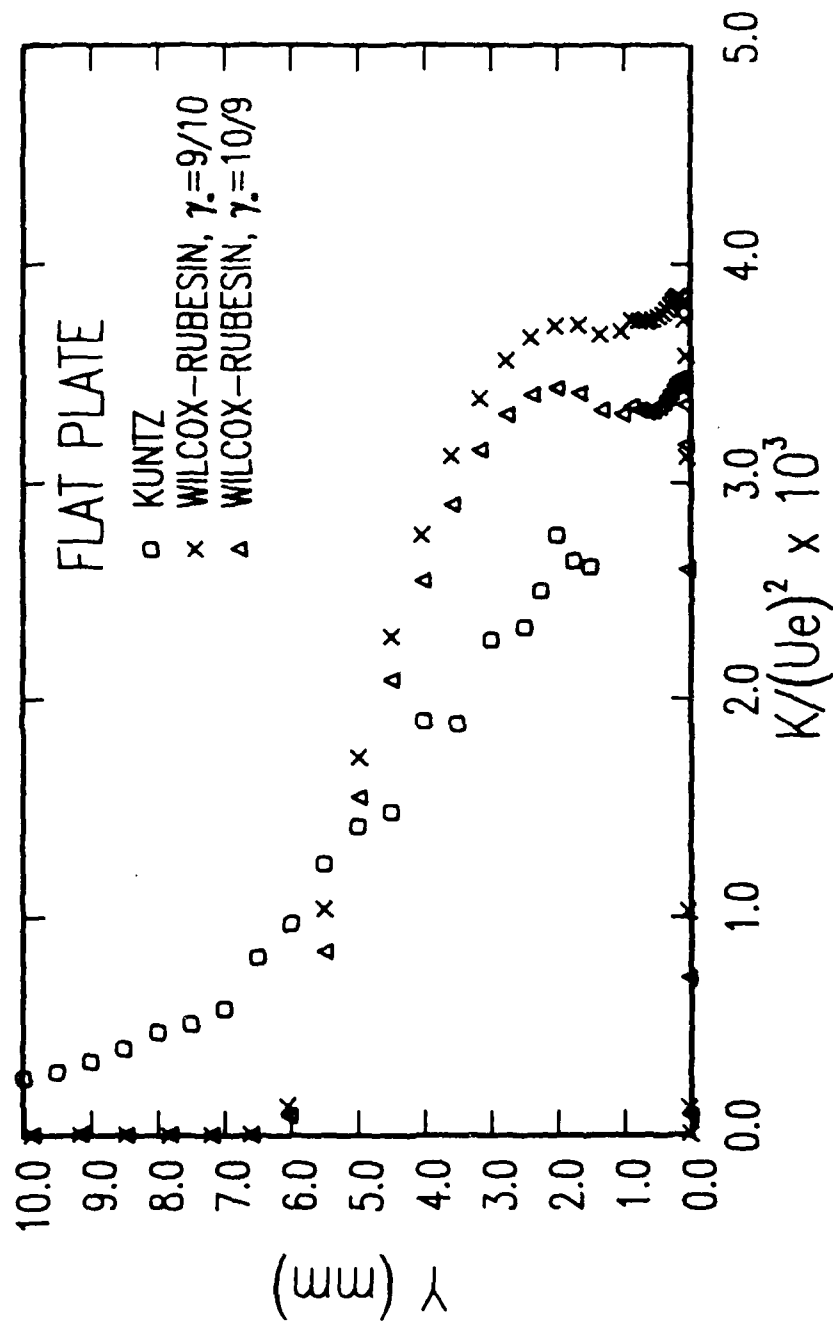


Figure 8. Turbulence kinetic energy profile, equilibrium flat plate boundary layer, $M = 2.94$

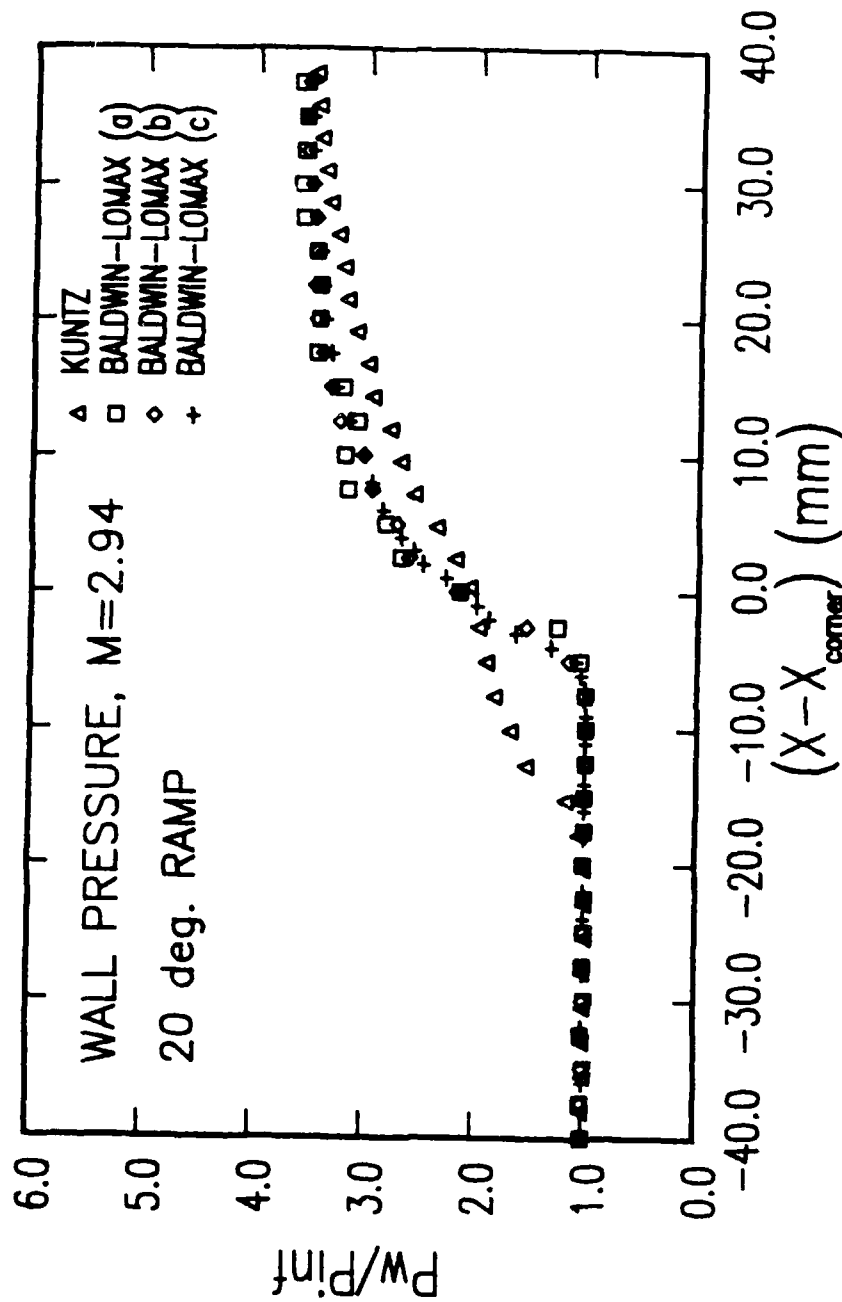


Figure 9. Wall static pressure distribution, separated oblique shock/turbulent boundary layer interaction, $M = 2.94$

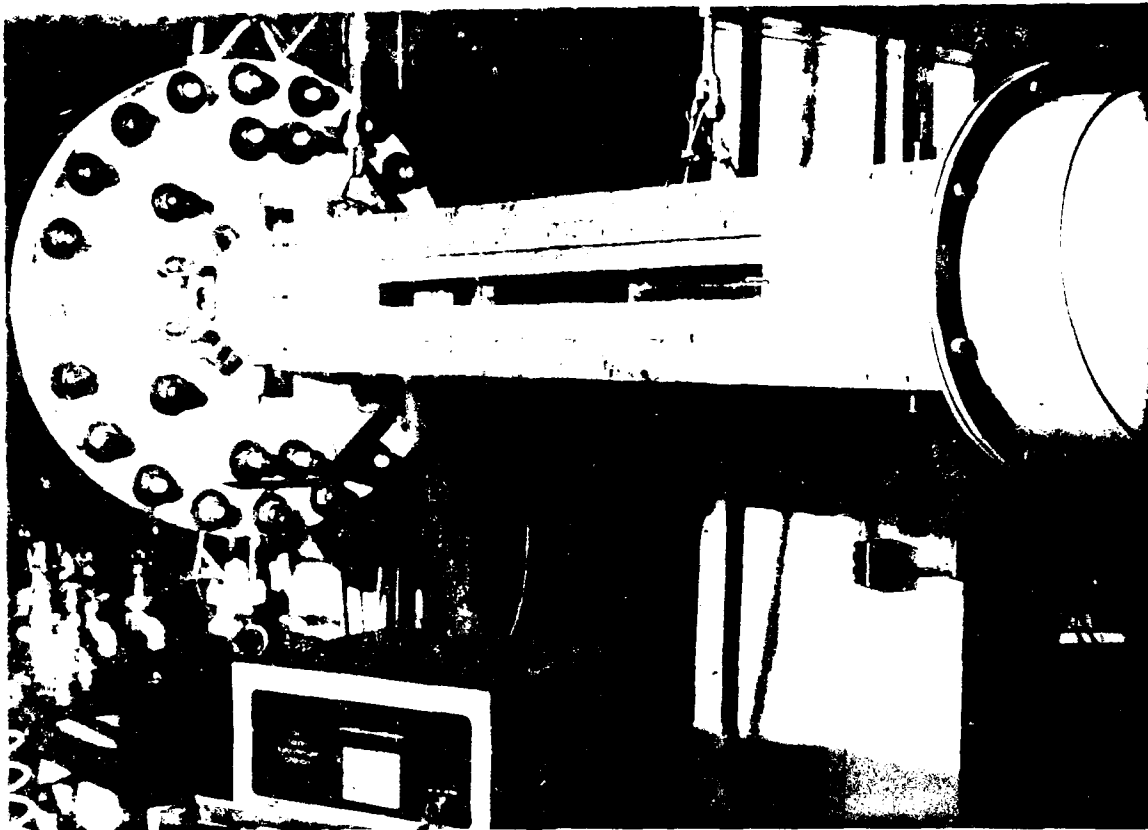


Figure 10. Wind tunnel with the Mach 1.6 nozzle blocks installed



Figure 11. Settling chamber



Figure 12. Mach 2.45 surface flow and Schlieren, $\delta u/h = 0.15$



Figure 13. Mach 2.45 surface flow and Schlieren, $\delta u/h = 0.26$



Figure 14. Mach 2.45 surface flow , $\delta u/h = 0.35$
(surface flow not possible due to flow unsteadiness)

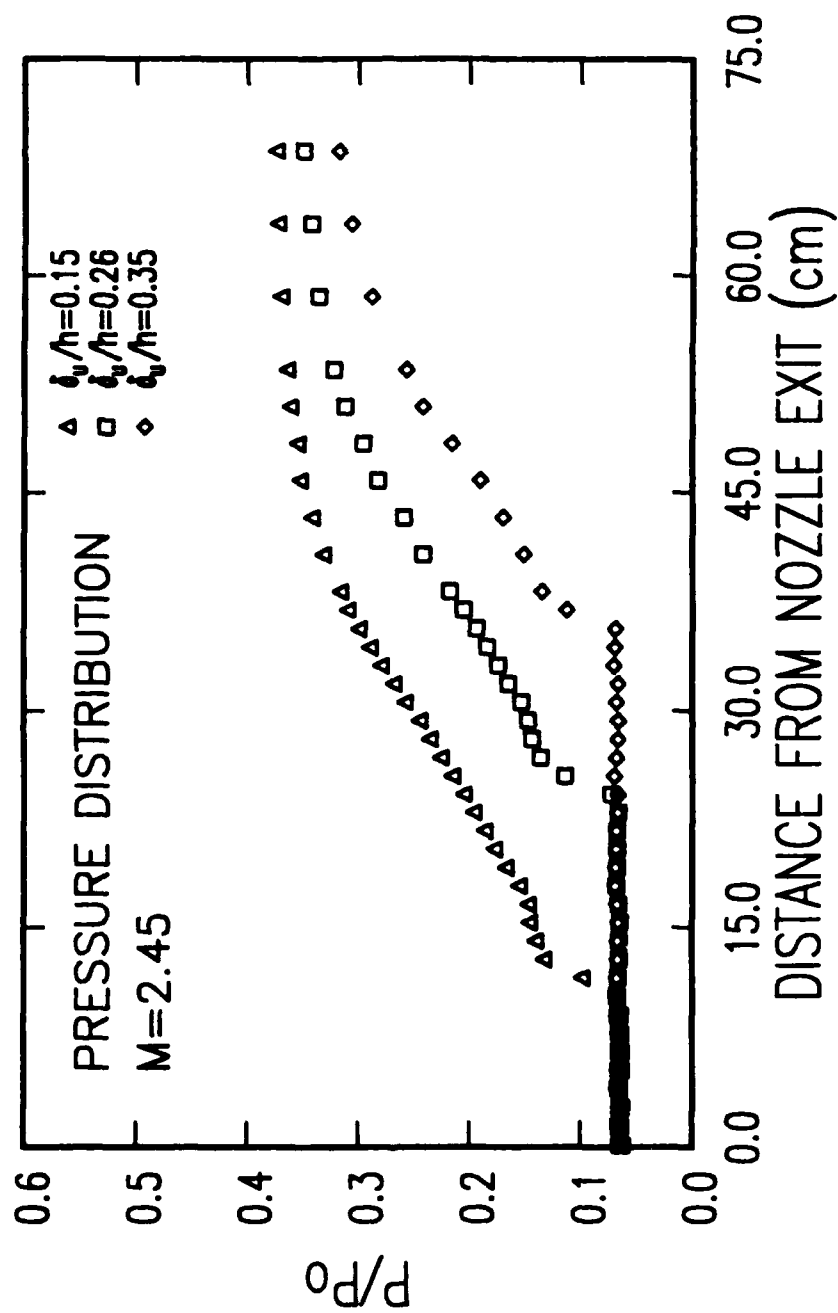


Figure 15. Wall static pressure distribution, unshifted

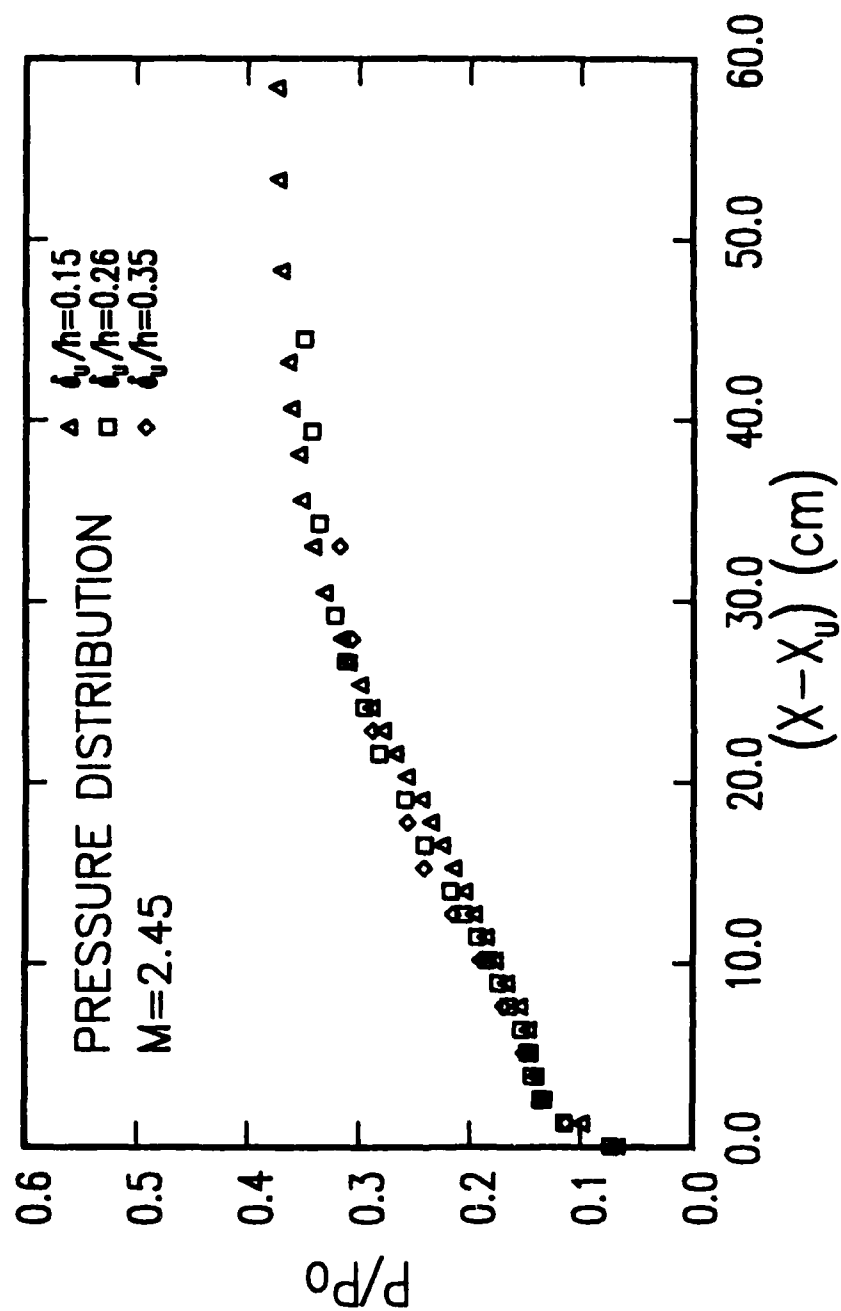


Figure 16. Wall static pressure distribution, shifted

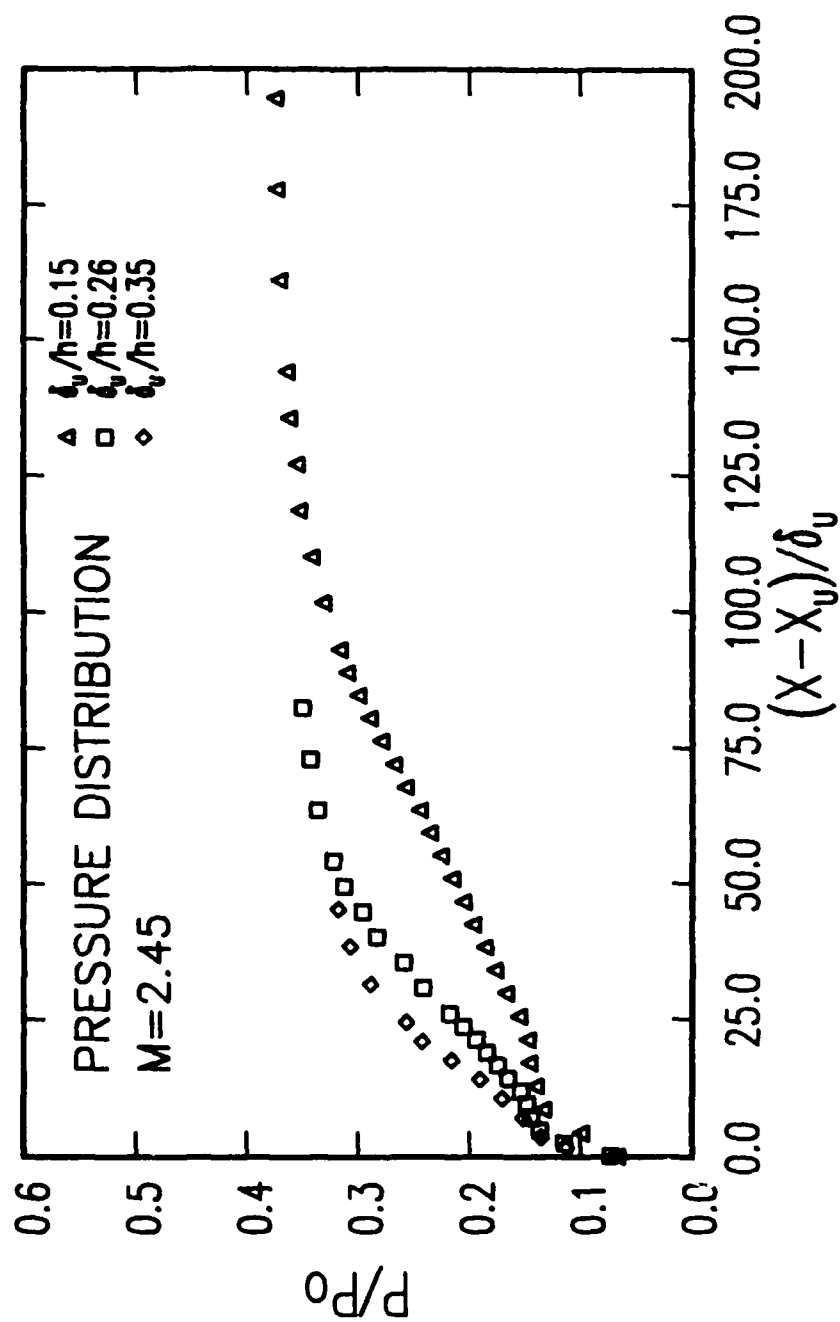


Figure 17. Wall static pressure distribution, shifted and non-dimensionalized

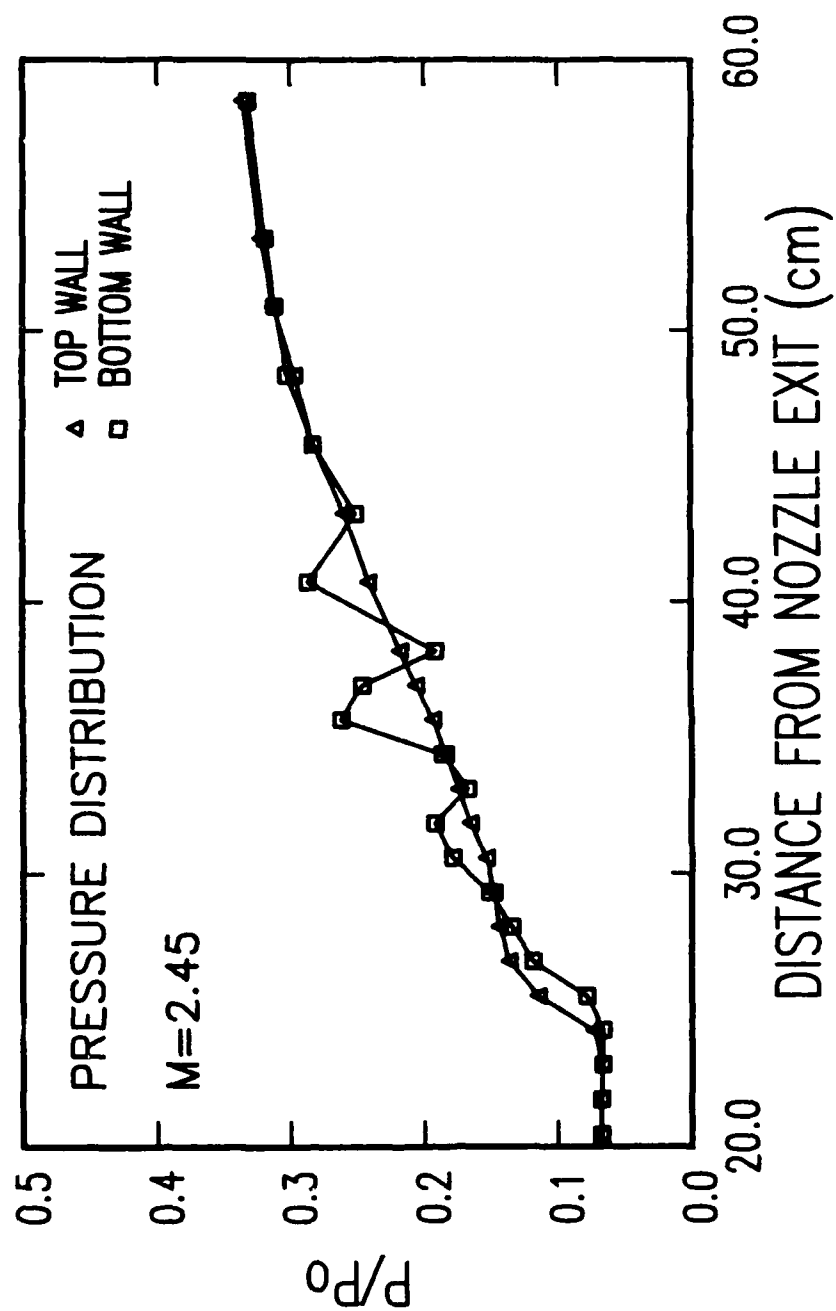


Figure 18. Top and bottom wall static pressure distribution

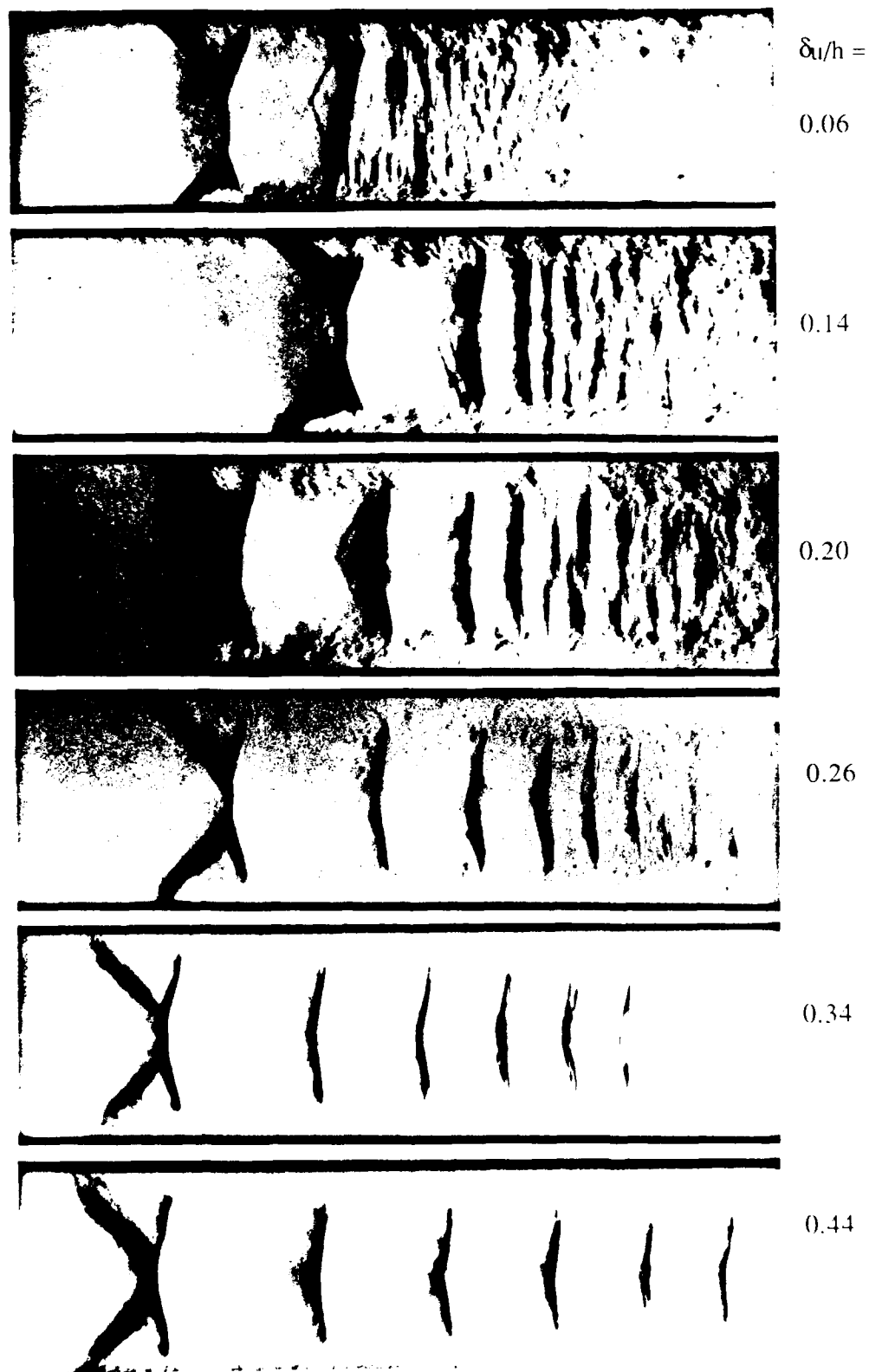


Figure 19. Schlieren, low sensitivity, $Mu = 1.6$

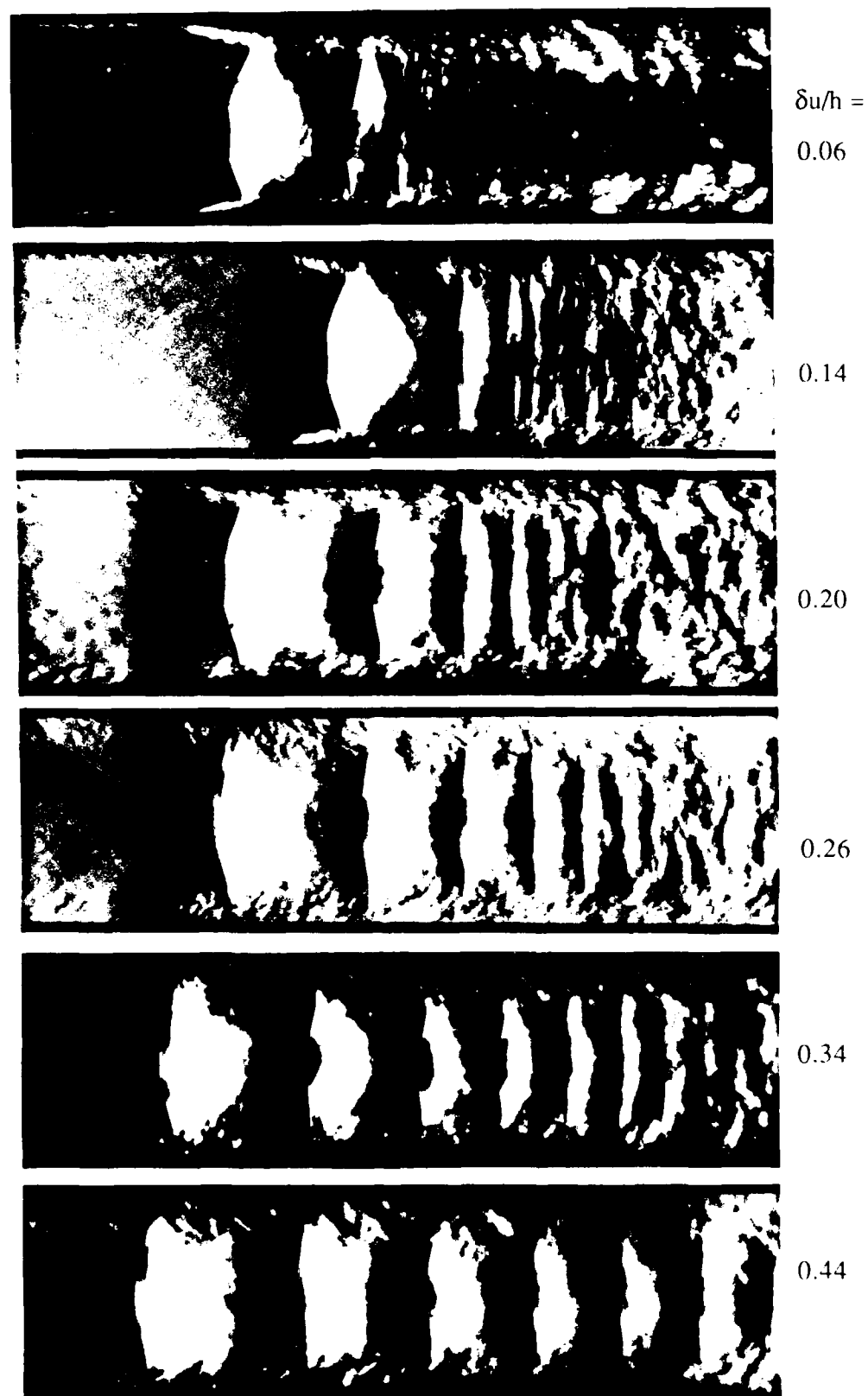
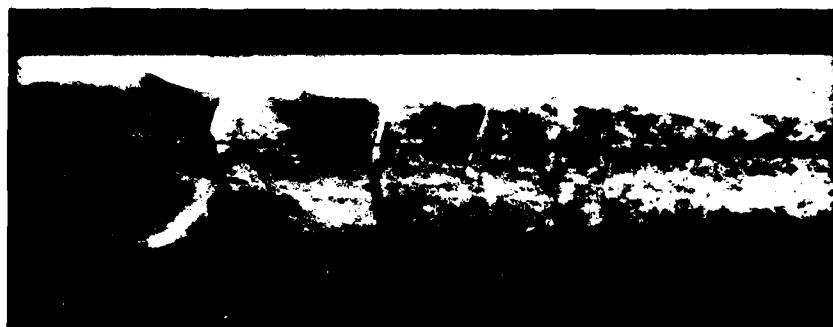


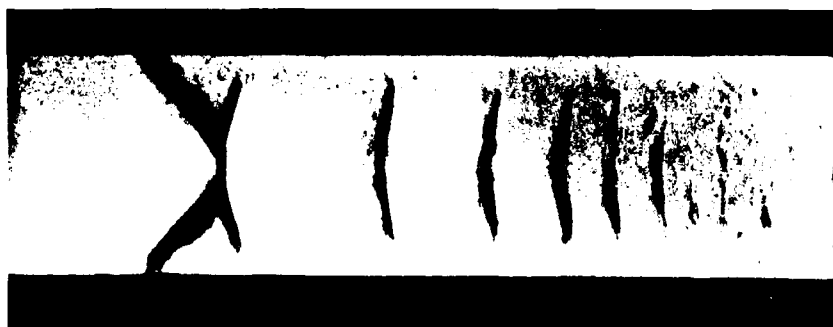
Figure 20. Schlieren, high sensitivity, $Mu = 1.6$



a) Horizontal knife edge



b) Vertical knife edge, high sensitivity



c) Vertical knife edge, low sensitivity

Figure 21. Schlieren, $Mu = 1.6$, $\delta u/h = 0.34$

top wall

side view

bottom wall



Figure 22. Mach 1.6 surface flow and Schlieren, $\delta u/h = 0.34$

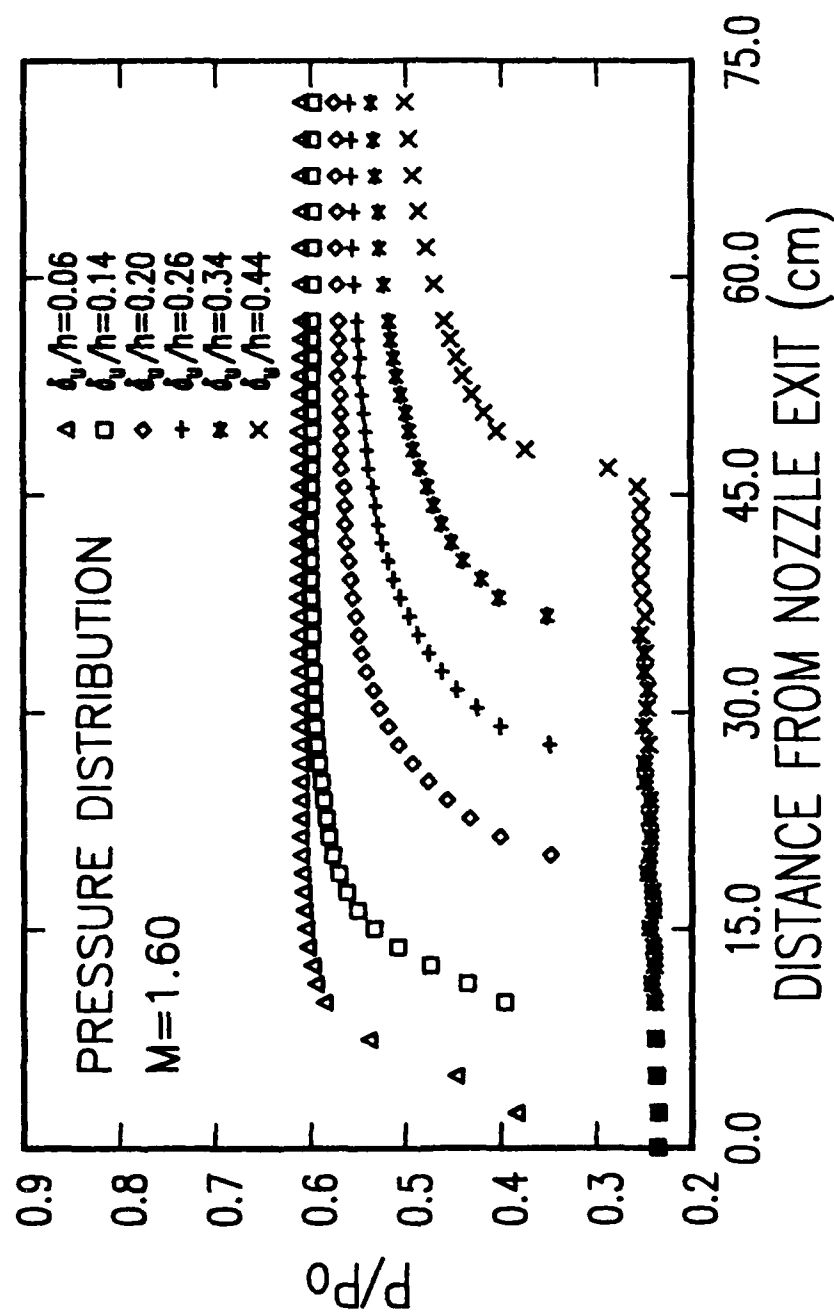


Figure 23. Wall static pressure distribution, unshifted

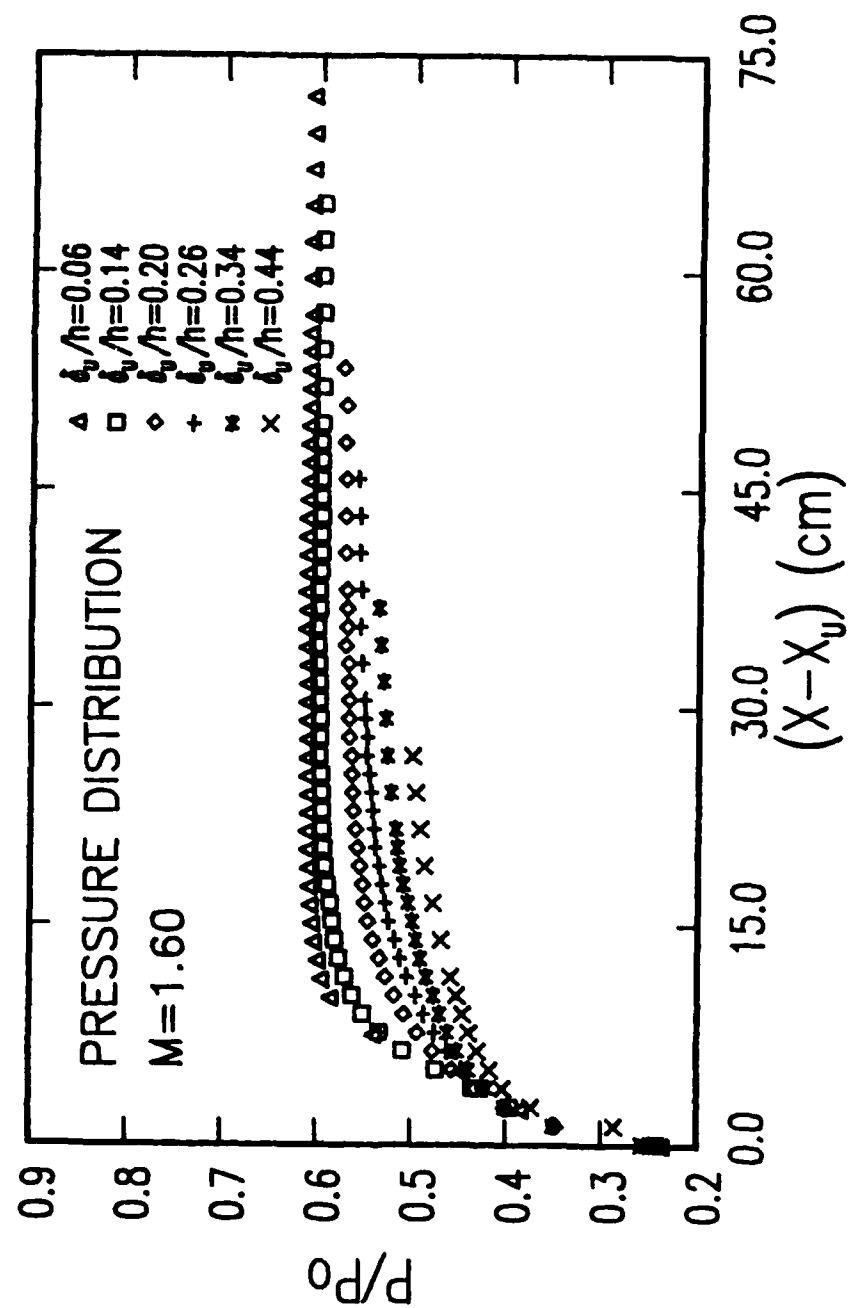


Figure 24. Wall static pressure distribution, shifted

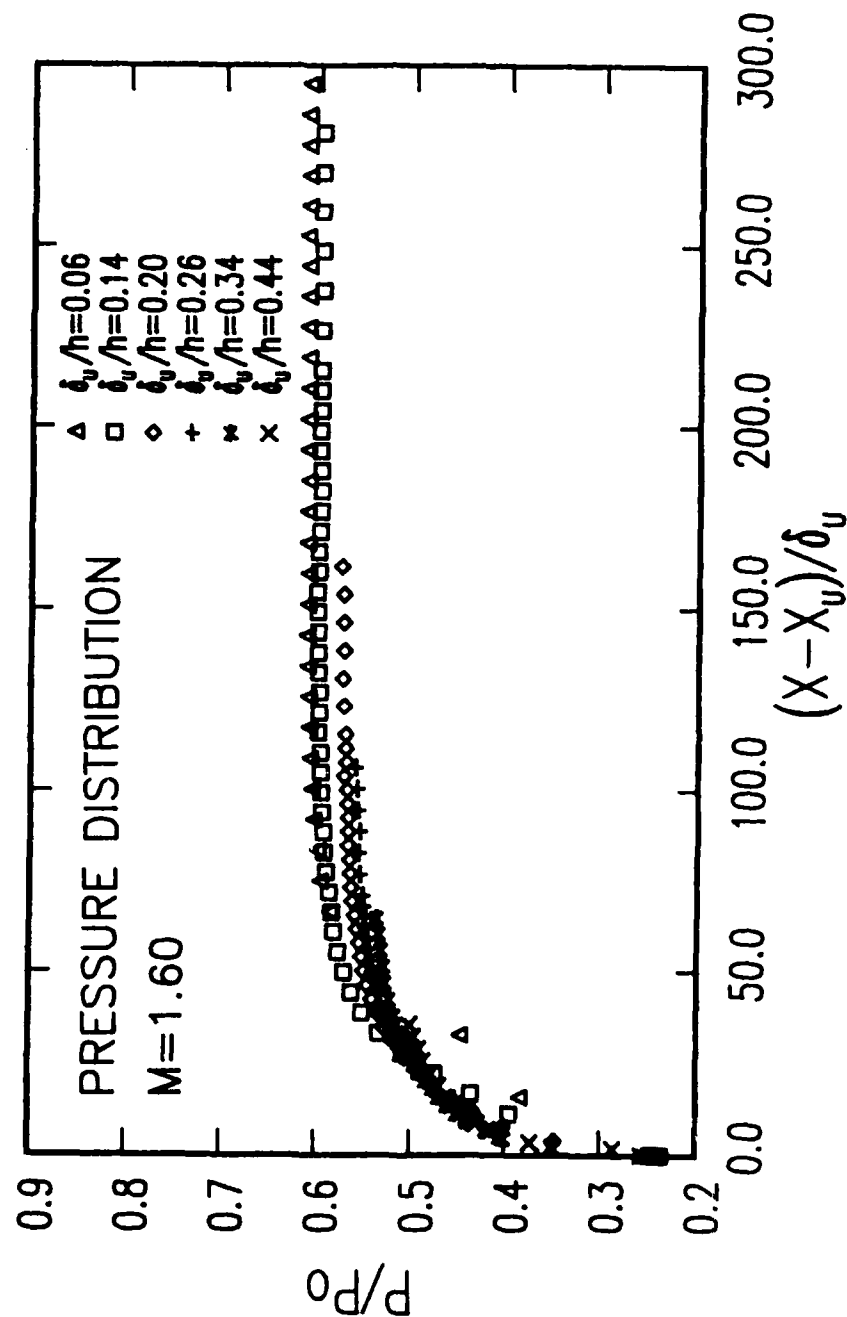


Figure 25. Wall static pressure distribution, shifted and non-dimensionalized

APPENDIX A

Collected here are the definitions of the Ψ_i and Ω_i which are required in the compatibility relations of the reference plane characteristic outflow boundary condition. The Ψ_i are treated as source terms and all derivatives contained within the Ψ_i are evaluated using finite difference expressions which maintain second order accuracy. The Ω_i are simply convenient groupings of terms.

$$\Psi_1 = \frac{1}{J} \left\{ y_\xi (u \rho_\eta + \rho u_\eta) - x_\xi (v \rho_\eta + \rho v_\eta) \right\} \quad (A1)$$

$$\begin{aligned} \Psi_2 = & -\frac{1}{J} \left\{ u_\eta (-y_\xi u + x_\xi v) - y_\xi p_\eta / \rho \right\} \\ & + \frac{1}{\rho J^2} \left\{ y_\eta \left[(\lambda + 2\mu) \frac{\partial u}{\partial x} + \lambda \frac{\partial v}{\partial y} \right]_\xi - y_\xi \left[(\lambda + 2\mu) \frac{\partial u}{\partial x} + \lambda \frac{\partial v}{\partial y} \right]_\eta \right. \\ & \left. - x_\eta \left[\mu \frac{\partial v}{\partial x} + \mu \frac{\partial u}{\partial y} \right]_\xi + x_\xi \left[\mu \frac{\partial v}{\partial x} + \mu \frac{\partial u}{\partial y} \right]_\eta \right\} \end{aligned} \quad (A2)$$

$$\begin{aligned} \Psi_3 = & -\frac{1}{J} \left\{ v_\eta (-y_\xi u + x_\xi v) + x_\xi p_\eta / \rho \right\} \\ & + \frac{1}{\rho J^2} \left\{ -x_\eta \left[(\lambda + 2\mu) \frac{\partial v}{\partial y} + \lambda \frac{\partial u}{\partial x} \right]_\xi + x_\xi \left[(\lambda + 2\mu) \frac{\partial v}{\partial y} + \lambda \frac{\partial u}{\partial x} \right]_\eta \right. \\ & \left. + y_\eta \left[\mu \frac{\partial v}{\partial x} + \mu \frac{\partial u}{\partial y} \right]_\xi - y_\xi \left[\mu \frac{\partial v}{\partial x} + \mu \frac{\partial u}{\partial y} \right]_\eta \right\} \end{aligned} \quad (A3)$$

$$\begin{aligned} \Psi_4 = & -\frac{1}{J} \left\{ (-u y_\xi + v x_\xi) p_\eta \right\} - \frac{a^2}{J} \left\{ (-u y_\xi + v x_\xi) \rho_\eta \right\} \\ & \frac{(\gamma-1)}{J^2} \left\{ (\lambda + 2\mu) \left(\frac{\partial u}{\partial x} \right)^2 + (\lambda + 2\mu) \left(\frac{\partial v}{\partial y} \right)^2 + \mu \left(\frac{\partial u}{\partial y} \right)^2 + \mu \left(\frac{\partial v}{\partial x} \right)^2 \right. \\ & \left. + 2\lambda \left(\frac{\partial u}{\partial x} \right) \left(\frac{\partial v}{\partial y} \right) + 2\mu \left(\frac{\partial u}{\partial y} \right) \left(\frac{\partial v}{\partial x} \right) + y_\eta \left[\rho \alpha \frac{\partial h}{\partial x} \right]_\xi - y_\xi \left[\rho \alpha \frac{\partial h}{\partial x} \right]_\eta \right\} \end{aligned}$$

$$- x_{\eta} \left[\rho \alpha \frac{\partial h}{\partial y} \right]_{\xi} + x_{\xi} \left[\rho \alpha \frac{\partial h}{\partial y} \right]_{\eta} \} \quad (\text{A4})$$

Where

$$\frac{\partial u}{\partial x} = y_{\eta} u_{\xi} - y_{\xi} u_{\eta} \quad (\text{A5})$$

$$\frac{\partial u}{\partial y} = -x_{\eta} u_{\xi} + x_{\xi} u_{\eta} \quad (\text{A6})$$

$$\frac{\partial v}{\partial x} = y_{\eta} v_{\xi} - y_{\xi} v_{\eta} \quad (\text{A7})$$

$$\frac{\partial v}{\partial y} = -x_{\eta} v_{\xi} + x_{\xi} v_{\eta} \quad (\text{A8})$$

$$\frac{\partial h}{\partial x} = y_{\eta} h_{\xi} - y_{\xi} h_{\eta} \quad (\text{A9})$$

$$\frac{\partial h}{\partial y} = -x_{\eta} h_{\xi} + x_{\xi} h_{\eta} \quad (\text{A10})$$

$$a^2 = \frac{\gamma p}{\rho} \quad (\text{A11})$$

$$\rho \alpha = \frac{\mu_t}{Pr_t} + \frac{\mu_l}{Pr_l} \quad (\text{A12})$$

$$h = C_p T \quad (\text{A13})$$

$$\mu = \mu_t + \mu_l \quad (\text{A14})$$

$$\lambda = -\frac{2}{3} \mu \quad (\text{A15})$$

The Ω_i are given by

$$\Omega_1 = a^2 \quad (\text{A16})$$

$$\Omega_2 = x_{\eta} \quad (\text{A17})$$

$$\Omega_3 = y_{\eta} \quad (\text{A18})$$

$$\Omega_4 = \Omega_6 = \frac{\rho \, a \, y_\eta}{\sqrt{x_\eta^2 + y_\eta^2}} \quad (\text{A19})$$

$$\Omega_5 = \Omega_7 = \frac{\rho \, a \, x_\eta}{\sqrt{x_\eta^2 + y_\eta^2}} \quad (\text{A20})$$

APPENDIX B. RESEARCH CONTRACT-RELATED PUBLICATIONS

Carroll, B. F., Dutton, J. C., and Addy, A. L., "NOZCS2: A Computer Program for the Design of Continuous Slope Supersonic Nozzles," Report No. UILU-ENG-86-4007 Department of Mechanical and Industrial Engineering, University of Illinois at Urbana-Champaign, August 1986.

Carroll, B. F., "A Numerical and Experimental Investigation of Multiple Shock Wave/Turbulent Boundary Layer Interactions in a Rectangular Duct," Ph. D. thesis proposal, Department of Mechanical and Industrial Engineering, University of Illinois at Urbana-Champaign, February 1987.

Carroll, B. F. and Dutton, J. C., "Characteristics of Multiple Shock Wave/Turbulent Boundary Layer Interactions in Rectangular Ducts," accepted for publication and presentation at the National Fluid Dynamics Congress, Cincinnati, Ohio, July 1988.

Carroll, B. F., "A Numerical and Experimental Investigation of Multiple Shock Wave/Turbulent Boundary Layer Interactions in a Rectangular Duct," Ph. D. thesis, Department of Mechanical and Industrial Engineering, University of Illinois at Urbana-Champaign, in progress.

APPENDIX C. PARTICIPATING PERSONNEL

FACULTY

J. Craig Dutton
Associate Professor

GRADUATE STUDENT

Bruce F. Carroll
ONR Graduate Fellow

SHOP SERVICES

Gregory L. Cler
Instrument Maker

William D. Morfey
Instrument Maker

Leroy W. Westendorf
Instrument Maker